

**Cretaceous mantle of the Congo craton:
Evidence from mineral and fluid inclusions in Kasai alluvial diamonds**

by

Charles Walter Kosman

BSc Honours, McGill University

A THESIS SUBMITTED IN PARTIAL FULFILLMENT OF THE REQUIREMENTS FOR
THE DEGREE OF
MASTER OF SCIENCE

in

The Faculty of Graduate and Postdoctoral Studies
(Geological Sciences)

THE UNIVERSITY OF BRITISH COLUMBIA

(Vancouver)

December 2015

Abstract

Alluvial diamonds from the Kasai River, Katanga Province, Democratic Republic of the Congo (DRC), were studied in order to constrain the composition, thermal state, and diamond forming fluids of the ancient lithospheric mantle of the Congo craton. The diamonds originate from Cretaceous kimberlites of the Lucapa graben in northeastern Angola. We report carbon isotope compositions ($\delta^{13}\text{C}_{\text{VPDB}}$), nitrogen concentrations ([N]), and nitrogen aggregation states of 138 diamonds, as well as compositions of mineral and fluid inclusions in the diamonds. Diamonds emplaced by kimberlites of the northeastern Lucapa graben and eroded into alluvials along the Kasai river contain 25–2900 ppm [N], show 0–88% N aggregation and $\delta^{13}\text{C}$ isotopic compositions spanning -27‰ to -2‰ with a mode near mantle-like values.

In situ cathodoluminescence (CL), secondary ion mass spectrometry (SIMS) and Fourier transform infrared spectroscopy (FTIR) reveal large heterogeneities in [N], N aggregation and $\delta^{13}\text{C}$, indicating diamonds grew episodically from fluids of distinct sources. Fluid inclusion compositions of fibrous diamonds analyzed by electron probe microanalysis are moderately to highly silicic, matching compositions of diamond-forming fluids from other DRC diamonds. Regional homogeneity of Congo fibrous diamond fluid inclusion compositions suggests spatially extensive homogenization of Cretaceous diamond forming fluids within the Congo lithospheric mantle. Electron probe microanalysis (EPMA) of trapped silicate inclusions revealed both peridotitic (Fo_{91-95} and En_{92-94} , 78% of the suite) and eclogitic parageneses (Cr-poor pyrope and omphacite with 11–27% jadeite, 17% of the suite) within diamonds (11% remainder unknown). Clinopyroxene-garnet thermobarometry suggest diamond formation at 1350–1375 °C, whereas [N] aggregation thermometry yields diamond residence temperatures between 1000 and 1275 °C, if the assumed residence time is 0.9–3.3 Ga. Integrated geothermobarometry indicates heat fluxes of 41–45 mW/m² during diamond formation and a shallow lithosphere-asthenosphere boundary (LAB) 175–189 km. The shallow LAB may result from a higher than average cratonic geotherms and the position of the Kasai block near the Congo cratonic margin. The hotter mantle may be attributable to contemporaneous rifting of the southern Atlantic, multiple post-Archean reactivations of the craton, and/or proximal Cretaceous plumes.

Preface

Samples used in this research were acquired from the Denver Museum of Nature and Science with the help of Curator James W. Hagadorn and James F. Hurlbut. I completed all polishing, EPMA, and FTIR of the samples. *In situ* carbon isotope and nitrogen concentration analyses were undertaken at the Canadian Centre for Isotopic Microanalysis at the University of Alberta, Edmonton, Canada.

Parts of this manuscript are intended to be submitted to a peer-reviewed geosciences journal in 2016 for publication.

Table of Contents

Abstract.....	ii
Preface.....	iii
Table of Contents	iv
List of Tables.....	vi
List of Figures.....	vii
1. Introduction.....	1
2. Regional Geology	4
3. Samples.....	6
4. Analytical Methods.....	8
4.1 Electron probe microanalysis (EPMA).....	8
4.2 Fourier transform infrared spectroscopy (FTIR)	8
4.3 Secondary ion mass spectrometry (SIMS)	9
5. Results.....	11
5.1 Physical characteristics	11
5.2 Compositions of mineral inclusions.....	11
5.3 Compositions of fluid inclusions	18
5.4 N analysis using different techniques: comparison between FTIR and SIMS	21
5.5 Nitrogen characteristics and nitrogen geothermometry	22
5.6 Composition of carbon isotopes and their relationship to [N] characteristics.....	24
5.7 Cathodoluminescence	26
6. Discussion.....	28
6.1 Sources of diamond carbon and their variation	28
6.2 Composition of diamond forming fluids	30
6.3 Thermal state of the Congo craton in the Cretaceous	31
6.4 Dual paragenesis origin of diamonds.....	35
7. Conclusions.....	39

References.....	40
Appendix A: Diamond Physical Characteristics.....	50
Appendix B: EPMA Data of Silicate Inclusions.....	57
Appendix C: Precision of EPMA analyses of polished mineral inclusions.....	62
Appendix D: Cathodoluminescence Images.....	63
Appendix E: $\delta^{13}\text{C}$, [N] and cathodoluminescence (CL) characteristics of Kasai River diamonds	74

List of Tables

Table 1. Physical characteristics of Kasai diamonds.....	10
Table 2. Summary of Kasai River alluvial diamond inclusion phases and parageneses.....	12
Table 3. Averaged composition of fluid inclusions in the fibrous cuboid Kasai River diamonds.....	18

List of figures

Figure 1. Geological and geographic positions of sampling locations for studied Kasai diamond	3
Figure 2. Representative photographs of studied Kasai River alluvial diamonds	6
Figure 3. Mg# of olivine inclusions in diamond from alluvial diamonds of the Kasai River, Katanga province, DRC	13
Figure 4. Chemistry of orthopyroxene inclusions from alluvial diamonds of the Kasai River, Katanga Province, DRC	14
Figure 5. Sodium vs aluminum cations for eclogitic (omphacitic) clinopyroxenes.	16
Figure 6. EPMA analyses of fibrous inclusions normalized to 100% Si+Al, Ca+Fe+Mg, and K+Na cation components.....	19
Figure 7. Temperature isotherms as a function of total nitrogen concentration [N] and degree to which nitrogen is aggregated in the B state (%[N] _B).	21
Figure 8. Carbon isotope composition ($\delta^{13}\text{C}$) vs [N] ppm for 221 points analyzed via SIMS for alluvial diamonds of the Kasai River.....	24
Figure 9. Representative cathodoluminescence (CL) images of six polished alluvial diamonds of the Kasai River, Katanga Province, DRC	25
Figure 10. Pressure-temperature diagram of Kasai diamond inclusions and previously published xenolith data	31
Figure 11. The modern day southern Atlantic Ocean with select hotspot tracks, alkaline magmatic provinces, and continental flood basalts (CFBs).....	37

1. Introduction

Old, cold, and thick roots of lithosphere with the potential to grow and store diamonds extend beneath Archean cratons. This subcontinental lithospheric mantle (SCLM) records the growth and modification of Earth's continents spanning from the Archean to present. SCLM minerals and fluids trapped within diamonds comprise a robust sample set by which to trace ancient mantle processes at 150 km and deeper. These minerals and fluids, shielded from a constantly changing mantle environment, provide the insight into the mantle composition and thermal state of the early continents.

Ancient, cratonic roots are neither heterogeneous nor static. Events including plume impingement, rifting, and accretion are capable of modifying the parageneses, structure, thermal state of SCLM, sometimes to the demise of the cratonic root and other times not (e.g. Helmstaedt and Gurney, 1995; Gibson et al., 1999; Griffin et al., 2003; Miller et al., 2012). Thus, characterization of SCLM within and between cratons in the context of their idiosyncratic geodynamic histories is an important contribution to our understanding of mantle dynamics.

The SCLM beneath some cratons, notably the Kaapvaal (e.g., Boyd and Gurney, 1986; Kopylova et al., 1997; Phillips et al., 2004), Slave (e.g., Davies et al., 1999; Tappert et al., 2005; De Stefano et al., 2009; Smart et al., 2012), Superior (e.g., Stachel et al., 2006; Miller et al., 2012) and Siberian (e.g., Griffin et al., 1993; Sobolev et al., 1999), have been characterized in substantial detail from the perspective of diamond inclusions; these studies revealed the mantle lithologies, the thermal state and the thickness of the lithosphere at the time of the kimberlite emplacement and have been fundamental in shaping models of SCLM formation. Despite the Congo craton's sheer size (Begg et al., 2009), few studies have investigated the underlying lithospheric mantle, with only one systematic study of Congo diamond inclusions thus far (Mveumba Ntanda et al., 1982). Of the lherzolitic, eclogitic, and sulfide minerals in this study, temperatures of 1090 °C and 1147 °C were calculated for two single lherzolitic clinopyroxenes at pressures of 54 kb and 59 kb, respectively.

Although a high-resolution shear-wave tomographic model of Central Africa is available (i.e., Begg et al. 2009), a geochemical picture of the Congo SCLM is lacking, and a temporal evolution of the thermal state of the Congo mantle is unknown. To fill this gap in our knowledge, we investigate inclusions in diamonds of the Kasai block of the Congo craton to constrain for the first time the Early Cretaceous geotherm, lithosphere asthenosphere-boundary, diamond host rocks, and diamond forming fluids of part of the Congo craton. These data complement analogous data for other cratons globally, helping us to understand the most general patterns in the evolution of the continental mantle.

Most Congo craton kimberlites are concentrated within the Lucapa graben, a northeast-southwest lineament extending from southwestern Angola to southeastern DRC (Figure 1A). Kimberlite ages are broadly contemporaneous with nearby plume activity and associated continental breakup, leading some to suggest

a causal relationship (e.g., Torsvik et al., 2010) as has been suggested for other cratons (e.g., Sao Francisco, Thompson et al., 1998; Kaapvaal, Bell et al., 2003). Thus, thermometry of diamonds and their inclusions provide insights into the mantle of the old continent during extension and rifting which cannot be obtained in any other way. For example, thermometry could resolve whether the Congo SCLM has been heated by plume activity like that of the Superior craton (Miller et al., 2012), or remained cold, like that of the Kaapvaal craton (Bell et al., 2003). Our findings contribute to a better understanding of the relationship between crustal tectonics and mantle dynamics, as well as diamond forming processes.

2. Regional Geology

The Congo craton is one of four cratons that comprise the African continent. The Congo craton is composed of several Archean blocks, adjacent Proterozoic mobile belts and areas covered by Proterozoic and Phanerozoic sediments (Figure 1). The exposed Kasai block in the southeastern part of the craton is a heterogeneous Paleoarchean to Mesoarchean (3.49–3.01 Ga) granulite complex, although whole rock Rb–Sr dating suggests that the granulite complex ranges in age from 3.49 and 3.33 Ga (De Waele et al., 2008). Zircons derived from heavy mineral concentrates northward of the Kasai river, the product of drainage from a myriad of host rocks spanning large intervals of geologic time, yield laser ablation inductively coupled plasma mass spectrometry (LA ICP-MS) U–Pb ages as old as 3.6 Ga (Batumike et al., 2009a). The Kasai block was metamorphosed in Mesoarchean to Neoarchean time (2.9–2.6 Ga) and is thought to have mostly accreted and docked to the Congo craton by 2.8 Ga (De Waele et al., 2008; Begg et al., 2009). The craton is bounded on the east by the 1.8 Ga Karagwe-Ankole Belt (KAB) and Kibara Belt (KIB), redefined from the continuous “Kibaran orogeny” (e.g., Tack et al., 2010; Fernandez-Alonso et al., 2012) resulting from convergent tectonism with the Tanzanian craton (Begg et al., 2009). Near 1.37 Ga, a failed intracratonic rift that may or may not have generated oceanic crust is recorded within the sedimentary and volcanic stratigraphy of the Kibaran belt (Tack et al., 2010). The Neoproterozoic Lufilian Arc obscures the southerly continuity of the KIB (Begg et al., 2009, Figure 1A). The southwestern extent of the craton is composed of the Archean orthogneissic Angolan block and Archean areas reworked in the Paleoproterozoic. Both the Kasai and Angolan blocks have been intruded by granitic bodies at ~2 Ga (De Waele et al., 2008, and references therein). However, the Kasai and Angolan blocks are separated by Phanerozoic basinal cover that prevents their rigorous correlation (De Waele, et al., 2008). The center of the craton is similarly extensively covered in Neoproterozoic basinal deposits (Begg et al., 2009). A root of low seismic velocity of the inferred lithospheric extent is as deep as 400 km beneath the center of the craton (Begg et al., 2009; O’Reilly et al., 2009).

The distribution of Angola’s kimberlites and other alkaline magmas is dictated by tectonic structures (Jelsma et al., 2004). Most Angolan kimberlites are concentrated within the Lucapa corridor or “graben”, a 50–90 km wide, northeast-southwest trending lineament of tectonic weakness episodically active since the Paleoproterozoic (Jelsma et al., 2004, Jelsma et al., 2009). The Lucapa corridor is along strike with a 400 km long set of discontinuous faults in southwest and central Angola (de Boorder et al., 1982) and eventually connects to a transfer fault of the southern Atlantic Ocean (Sykes, 1978). The Walvis Ridge of the southern Atlantic Ocean also aligns with the distribution of carbonatites and kimberlites on the continent. Jelsma et al. (2009) hypothesize that the distribution of western South Africa, Namibia, Lucapa graben kimberlites is controlled by asthenospheric melt migration along pre-existing fracture zones. Several African kimberlite clusters may be attributed to rifting (Jelsma et al., 2009), including the Kundelungu kimberlites (Batumike et al., 2008) emplaced along faults related to East Africa rift system. Roblez-Cruz et al. (2012b) similarly hypothesize that extensional tectonics associated with Jurassic-Cretaceous continental breakup allowed for emplacement of alkaline magmas, carbonatites and kimberlites along this extent. However, the alleged association of these kimberlites with lithospheric fracture zones does not imply a high heat flow of the

host cratons, as evident from thermobarometry of kimberlite-borne Kaapvaal materials (e.g., Stachel and Harris, 2008). Magmas classified as carbonatites appear to be more concentrated in southwestern Angola off cratonic margins, whereas kimberlites are more concentrated along the northeastern part of the trend (Reis, 1972; Demaiffe et al., 1991; Jelsma et al., 2009; Campeny et al., 2014; Figure 1). Alluvial diamond deposit distribution is dictated by the predominately northward flowing rivers, and thus alluvial deposits are typically to the north of kimberlite fields (Figure 1B).

Additionally, northeast Angolan kimberlite placement may be controlled by their setting near a steep change in lithospheric thickness. O'Neill et al. (2005) show that kimberlites and lamproites of Australia are localized near steep changes in lithospheric thickness, wherein a compromise between long-term diamond stability and asthenospheric melt generation is obtained. Faure et al. (2011) similarly show that North American diamondiferous kimberlites are distributed around cratonic roots, rather than within them, invoking a similar compromise between diamond stability and melt genesis. Kimberlites of northeast Angola lie near the southeastern margin of the inferred Congo craton root (e.g., Begg et al., 2009). Perhaps it is then the combination of the lineament of crustal weakness (Lucapa graben) and setting on a cratonic margin that is responsible for the crustal distribution of Angolan kimberlites, wherein thin roots allow for melt genesis and the crustal features channel the melts to their surface expressions.

Since the first discovery of kimberlite in Angola in 1952, more than 700 kimberlites have been discovered in the country (Reis, 1972; Robles-Cruz et al., 2012b). Plan view shapes of Angolan kimberlites are highly variable, spanning the spectrum of round to irregular (Demaiffe et al., 1991). Catoca, the first kimberlite mine in Angola and fourth largest in diamond reserves the world, is slightly ellipsoid and more than 900 m across (Nikitina et al., 2014). Six well-studied kimberlite pipes, Catoca (CA), Tchiuzo (TZ), Anomaly 116 (An116), Alto Cuilo-63 (AC63), Cucumbi-79 (CU79), and Alto Cuilo 4 (AC4) are characterized by the presence of both crater and diatreme facies with intense weathering up to 150 – 200 km depth (Roblez-Cruz et al. 2012b). Diatreme facies within the pipes include volcanoclastic kimberlite, volcanoclastic kimberlite breccia, and tuffisitic kimberlite, in order of increasing depth (Roblez-Cruz et al., 2012b). While Nikitina et al. (2014) note a predominance of eclogitic xenoliths at Catoca, Robles-Cruz et al. (2012b) report garnet lherzolites, wehrlites, and very rare eclogite xenoliths in the population. Kimberlites of northeast Angola have been dated to the Early Cretaceous (see references in Roblez-Cruz et al., 2012a); most recently, Roblez-Cruz et al. (2012a) report a U-Pb SHRIMP weighted mean age of zircons from Catoca of 117.9 ± 0.7 Ma (MSWD 1.3), correlated with the age of rifting of the southern Atlantic Ocean. In general, mantle derived alkaline magmas (including alkaline basalts, carbonatites, and kimberlites) of the southwestern extent of the Lucapa corridor are older than their more northeasterly counterparts; DRC kimberlites at Mbuji-Mayi are dated at 70 Ma (Schärer et al., 1997), whereas more southwesterly carbonatites are dated at 130 Ma (summarized in Alberti et al., 1999; Figure 1B). The paleolocation of the Cretaceous Congo Craton is thought to have been above the present day Tristan da Cunha mantle plume and associated large low-shear wave velocity province of the deep mantle, suggesting a temporal and genetic link between central African kimberlite magmatism and continental breakup (Wilson, 1992; Torsvik et al., 2010).

3. Samples

The studied diamonds (138 samples from the Paul Seel collection) were provided by the Denver Museum of Nature and Science (Appendix A). The stones were selected based on the presence of inclusions (Figure 2). The samples were collected in the 1960s from the Kasai River of the Katanga Province, DRC. The diamonds' primary sources are inferred to be the Early Cretaceous kimberlites of northeastern Angola on the basis of geographic proximity and regional sedimentary packages. The Congo basin is covered extensively by Neoproterozoic and Phanerozoic sediments (Figure 1A), suggesting the present regime of dominantly northward flowing rivers in NE Angola has been stable since the time of kimberlite emplacement in the Early Cretaceous. Such a regime has been generated by a complex history of subsidence of the Congo basin and uplift of highlands at least since Neoproterozoic time (Linol et al., 2015). Therefore, the diamonds of this study are inferred to have been liberated and transported from kimberlites of the Lucapa region with exception of the Mbuji-Mayi kimberlites, which lie 300 km northeast of the Lunda Norte province of northeastern Angola and at a lower altitude location within the Congo basin (Figure 1B).

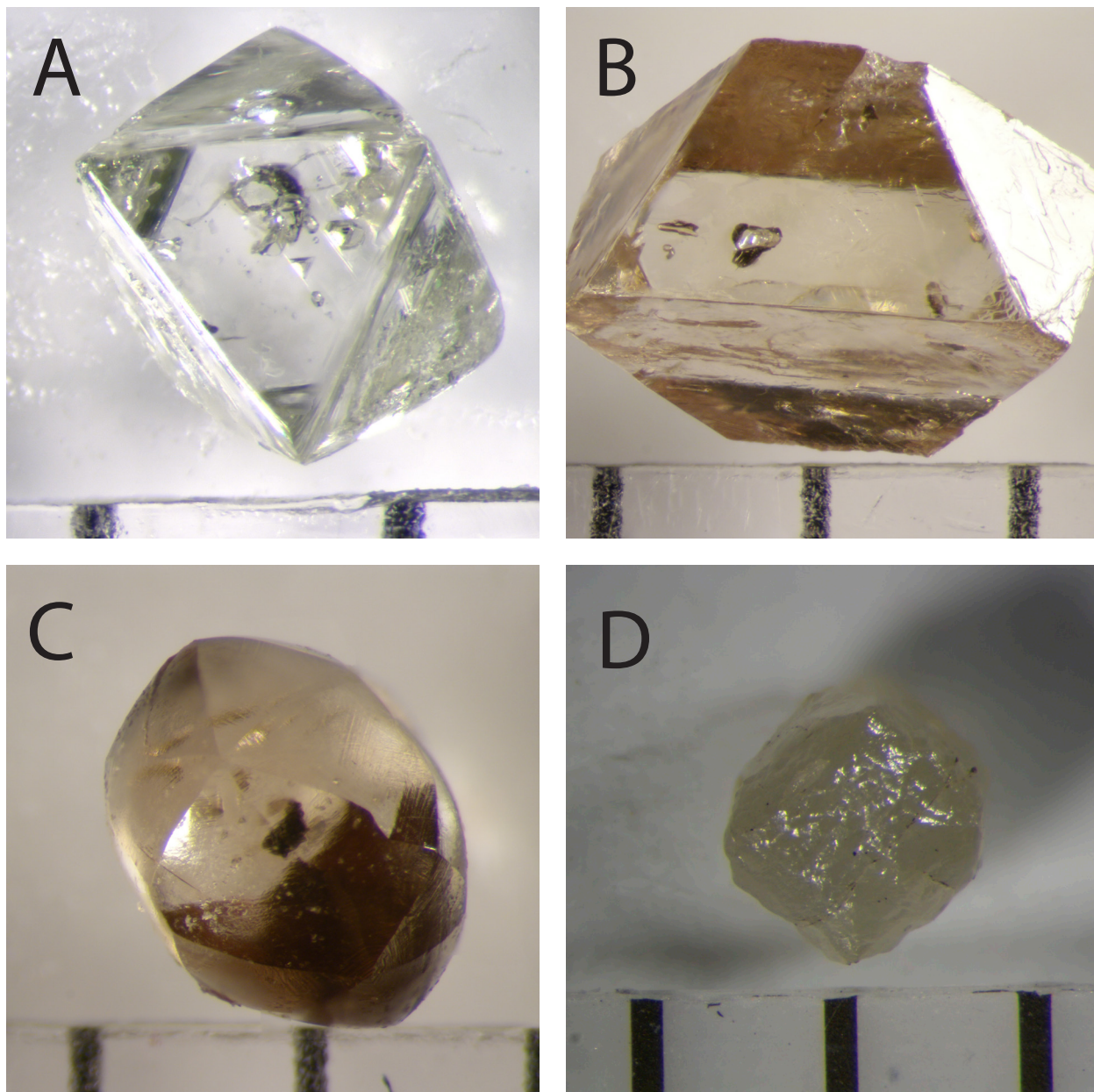


Figure 2. Representative photographs of studied Kasai River alluvial diamonds. Distance between black lines at the bottom of each photograph indicate 1 mm scale (A) Peridotitic diamond 11626 bearing olivine and orthopyroxene inclusions. (B) Peridotitic diamond 11691 bearing exclusively olivine mineral inclusions. (C) Eclogitic diamond 11712 bearing both garnet and clinopyroxene inclusions. (D) Fibrous coated diamond 10284.

4. Analytical Methods

4.1 Electron probe microanalysis (EPMA)

Twenty-nine octahedrally-grown diamonds with relatively large mineral inclusions were polished using a diamond-impregnated steel scaife to expose individual mineral inclusions. The inclusions were re-polished using diamond pastes to eliminate a possible addition of Fe from the scaife and mounted in an acrylic disk using epoxy or a combination of aluminum foil and conductive carbon putty. Quantitative chemical analyses were undertaken on a CAMECA SX-50 electron microprobe (University of British Columbia, Department of Earth, Ocean and Atmospheric Sciences; Appendix B). All elements were analyzed with a beam current of 20 nA, an acceleration voltage of 15 kV, a peak count time of 20s and two 10s backgrounds. Detection limits for most oxides are below 0.08 wt.%, with most closer to 0.04 wt.%. The exceptions are Cr, Mn, and Ni in select phases (0.11 wt.%; Appendix C). Fe³⁺ content was calculated stoichiometrically on the basis of the ideal oxygen unit total for each respective mineral.

Six of the 14 fibrous and coated diamonds were chosen on the basis of their fluid inclusion density to undergo EPMA analysis of trapped fluid inclusions. These diamonds were abraded to half their thickness using the diamond-impregnated steel scaife in order to sample fluids from the entirety of the diamonds' growth histories. Polished diamonds were cleaned and their exposed inclusion contents dissolved by submerging them in concentrated (68-70%) HNO₃ at 100°C for 24 hours, followed by concentrated HF (48-50%) at 100 °C for 24 hours.

Unexposed micro-inclusions (<1 µm) situated immediately beneath the polished surface were identified in electron backscatter on a CAMECA SX-50 electron microprobe (UBC, EOAS Dept.). The inclusions appear as bright sub-rounded spots without any visible surface relief in backscatter. Bright spots in backscatter at the locations of surface pits were interpreted as incompletely dissolved exposed micro-inclusions and were not studied. Inclusions were analyzed with a 1 µm wide beam at a current of 20 nA an acceleration voltage of 15 keV. Inclusions were selected from all parts of the diamonds to sample fluids from the entire growth history of the samples. Only analyses with totals above 4 wt.% were selected for further work. Totals on this order are expected because the inclusion volumes are very much smaller than the beam width (Kopylova et al., 2010). Even so, Weiss et al. (2008) demonstrate that EPMA analysis of fluid micro-inclusions precise to better than ± 15%, relative, for major element analysis.

4.2 Fourier transform infrared spectroscopy (FTIR)

Infrared spectra were collected at the CGL-GRS Swiss Canadian Gemlab (Vancouver, Canada) on a Nicolet 6700 Fourier transform infrared spectrometer. Each sample's absorbance spectra was measured at maximum light transmission. Background spectra were collected for 120 s prior to the analysis of each sample and were subtracted from each measured absorbance spectra. Count times for spectra were 40 seconds at a spectral resolution of 0.5 cm⁻¹. One to three analyses were performed per sample.

Nitrogen content and aggregation state of the diamonds were calculated by deconvoluting peaks corresponding to A and B centers using both a spreadsheet provided by John Chapman (Rio Tinto Diamonds, Ltd., 2014) and a spreadsheet developed by David Fischer (Diamond Trading Company Research Center, Maidenhead, UK, 1997; “DTC, 1997”). Both spreadsheets use a least squares approach to fit baseline corrected, thickness-normalized spectra to simulated A, B, C and D nitrogen peak spectra in accordance with the methodology of Medelssohn and Milledge (1995). Baseline corrections were performed visually with coordinates at 404 cm^{-1} , 1523 cm^{-1} , and 4000 cm^{-1} wavenumbers. A thickness correction factor of 12.3 cm^{-1} absorption units at 1992 cm^{-1} (Mendelssohn and Milledge, 1995) was applied in order to normalize spectra to a 1 cm sample thickness for the DTC (1997) spreadsheet. The Rio Tinto (2014) spreadsheet normalizes sample thickness based on peak height at 2160 cm^{-1} wavenumber. It also calculates IaA and IaB nitrogen content from spectra whose absorption coefficients are 16.5 ppm IaA cm^{-1} and 75 ppm IaB cm^{-1} at 1280 cm^{-1} wavenumber, whereas DTC (1997) uses absorption coefficients of 16.5 IaA cm^{-1} and 79.4 IaB cm^{-1} at 1282 cm^{-1} wavenumber in accordance with Boyd et al. (1994, 1995). For spectra that produce low-error fits in both programs, $[\text{N}]_{\text{B}}$ agree within 2%.

Both spreadsheets function similarly; however, Rio Tinto (2014) contains master A, B, and C spectra over the range 430 – 1530 cm^{-1} wavenumbers, in comparison to narrower range 1000 – 1400 cm^{-1} wavenumbers in DTC (1997). Although maximum absorbance peaks attributed to A, B and C nitrogen centers in diamond fall within this latter range, evaluating the quality of fit of over the entire A, B, and C peak widths allows for a more robust calculation of $[\text{N}]$. The wider range of wavenumbers in Rio Tinto (2014) allows for a better evaluation of the extent to which the choice of baseline has detracted from fit quality. Visual evaluation of fit indicates that DTC (1997) fits overestimates $[\text{N}]_{\text{B}}$ by up to 80 ppm.

4.3 Secondary Ion Mass Spectrometry (SIMS)

Mount preparation and secondary ion mass spectrometry (SIMS) were carried out within the Canadian Centre for Isotopic Microanalysis (CCIM) at the University of Alberta. Sectioned and polished diamonds (CCIM sample numbers S3204–S3244, excluding 3213) were cast into a single 25 mm diameter assembly (mount number M1319), along with a piece of CCIM reference material (RM) S0270. The mount was coated with 10 nm of Au prior to scanning electron microscopy (SEM) using a Zeiss EVO MA15 instrument, operating at 15 kV and 3 nA beam current. Cathodoluminescence SEM images were obtained using a parabolic mirror coupled to a high-sensitivity, broadband photomultiplier detector (Appendix D). The mount was subsequently coated with an additional 20 nm Au film prior to SIMS analysis.

Isotopes of carbon ($^{13}\text{C}/^{12}\text{C}$) were determined in session IP15025 using the IMS-1280 multi-collector ion microprobe at CCIM (Appendix E). Analytical methods follow the methods and reference materials detailed by Stern et al. (2014) and summarized by Palot et al. (2014). Primary beam conditions included the use of 20 keV $^{133}\text{Cs}^+$ ions focused to a diameter of $\sim 15\text{ }\mu\text{m}$ and beam currents of $\sim 2.3\text{ nA}$. The primary beam was rastered across a 20 x 20 μm area for 30 s prior to analysis, to clean the surface of Au and contaminants, and implant Cs. The normal incidence electron gun was not utilized, as most diamonds are

conducting under ion bombardment, and the use of the electron gun accentuates formation of unwanted carbon-hydride isobars. Negative secondary ions were extracted through 10 kV to the grounded secondary column (Transfer section). Automated tuning of the secondary ions in the Transfer section preceded each analysis. Secondary ion collection conditions for C-isotopes included an entrance slit width of 100 μm , field aperture of 5 x 5 mm, a field aperture-to-sample magnification of 100 x, and a fully-open energy slit. Both $^{12}\text{C}^-$ and $^{13}\text{C}^-$ were analyzed simultaneously in Faraday cups (L'2 using 1010 Ω amplifier, and FC2 with 1011 Ω) at mass resolutions of 1975 and 2900, respectively. Faraday cup baselines were determined once at the start of the session. Mean count rates for $^{12}\text{C}^-$ and $^{13}\text{C}^-$ were typically 1.2×10^9 and 1.3×10^7 counts/s, respectively, determined over a 75 s counting interval, with total analysis time of 210 s. The analytical sequence interspersed measurements of unknowns with the natural diamond S0270, having $\delta^{13}\text{C}_{\text{VPDB}} = -8.88 \pm 0.10 \text{ ‰}$ in a 4:1 ratio. Instrumental mass fractionation (IMF) for $^{13}\text{C}^-/^{12}\text{C}^-$ was -23.1 ‰, determined from utilizing all the replicate analyses (N = 60) of S0270 diamond. The standard deviation of the $^{13}\text{C}^-/^{12}\text{C}^-$ values was 0.05 ‰ after correction for systematic within-session IMF drift of +0.5‰ over 18 hours. Uncertainties of individual $\delta^{13}\text{C}_{\text{VPDB}}$ analyses propagate within-spot ($\sim \pm 0.05 \text{ ‰}$, 1σ), between-spot ($\pm 0.15 \text{ ‰}$, 1σ), and between-session errors ($\pm 0.01 \text{ ‰}$, 1σ), and average $\pm 0.32 \text{ ‰}$ (2σ). A larger-than-normal (typically $\pm 0.05 \text{ ‰}$, 1σ) between-spot blanket error was applied to account for possible biases resulting from the analysis of diamonds over a wide radius (i.e., $\pm 8 \text{ mm}$, compared to $\pm 5 \text{ mm}$ normally) away from the mount center.

Nitrogen abundances were determined following C-isotopes from the identical spot locations (Appendix E). The primary beam was rastered for 60 s prior to analysis. Secondary ion collection conditions included an entrance slit width of 40 μm , field aperture of 3 x 3 mm, and energy slit width of 40 eV transmitting low-energy ions. The molecular ions [$^{12}\text{C}^{14}\text{N}^-$]/[$^{12}\text{C}^{12}\text{C}^-$] were analyzed simultaneously using a Faraday cup–Faraday cup (L'2–FC2) combination where $^{12}\text{C}^{14}\text{N}^- > 1 \times 10^5$ counts/s, and Faraday cup–electron multiplier combination (L'2–EM) where $< 1 \times 10^5$ counts/s. Mass resolution was 7000 and 2100 for $^{12}\text{C}^{14}\text{N}^-$ and $^{12}\text{C}^{12}\text{C}^-$, respectively. Electron multiplier counts were corrected for background and deadtime (40 ns). Total analysis time was 240 s, including pre-analysis raster, secondary ion centering, and peak counting time of 50 s. The sensitivity factor for N in diamond was determined by analysis of RM S0280 having [N] = 1670 at. ppm ($\pm 5 \text{ ‰}$ absolute, 95% conf.) located on a separate mount (Stern et al., 2014).

A total of 221 analyses of both C-isotopes and [N] were carried out, typically 5 spots per diamond.

5. Results

5.1 Physical characteristics

The morphology of the diamonds, together with the degree of resorption and colour, were observed with a binocular microscope and documented (Table 1, Appendix A). It should be noted that these characteristics may not necessarily be representative of the alluvial diamonds of northeast Angola in general, but rather just the diamonds that were studied.

Most octahedrally-grown diamonds are of octahedral morphology ($n = 49$), followed by resorbed dodecahedra ($n = 35$), polycrystalline aggregates ($n = 13$), cuboid morphologies ($n = 12$), macles ($n = 10$), and unknown ($n = 5$). Diamond resorption degree was ranked from 1 (unresorbed) to 6 (no remaining octahedral faces) according to the scale of McCallum et al. (1994). Most diamonds are either lightly resorbed (class 5, $n = 37$) or completely resorbed (class 1, $n = 33$). With respect to the classification by morphology, diamonds in resorption categories 1 and 2 were classified as dodecahedra, whereas categories 3 through 6 were classified as octahedra. The samples are colourless ($n = 49$), brown ($n = 37$), yellow ($n = 17$), pink ($n = 9$), green ($n = 9$), and grey ($n = 3$). The remaining 14 diamonds were classified as fibrous or fibrous coated diamonds based on their low degree of transparency, cube or twinned cube morphologies, and uneven surface appearance characteristic of fibrous growth.

The observed morphology result from multiple growth and resorption events. These were mapped with cathodoluminescence (CL) photographs (Appendix D). They reveal that all diamonds contain multiple layers with distinct CL characteristics. The interpreted growth zone boundaries range from rounded to angular. The constituent layers of rounded growth zones commonly appear truncated by more exterior growth zones, interpreted as diamond resorption between growth events. This interpretation is supported by the observation that rounding and truncation of growth is most pronounced towards the vertices of octahedra. In many instances the morphology of the more interior growth zones is the same as that of the overall sample. Four of the 40 diamonds imaged in CL display more complex structures that suggest more than one core is present. CL brightness varies widely across samples, with the entire observed spectrum of brightness occurring within single samples.

5.2 Compositions of mineral inclusions

EPMA analysis of 106 mineral inclusions in 29 diamonds revealed four main phases: olivine (mean Fo_{93}) orthopyroxene (mean En_{93}), low-Cr garnet, and omphacitic clinopyroxene (11.8–36 mole % jadeite, Table 2, Appendix B). One pentlandite (36 wt.% Ni) and 2 pyrrhotite grains were also analyzed. Most of the diamonds ($n=21$, 72%) host only one mineral phase, with olivine-only diamonds comprising approximately half the sample set ($n=15$). Four diamonds host only omphacite, one diamond hosts orthopyroxene only, and one diamond low-Cr garnet only. Two phases assemblages constitute the remainder of the sample set ($n=8$). Olivine + orthopyroxene assemblages constitute the most abundant two phase assemblage type and second most abundant assemblage overall with a total of seven samples. A single diamond hosts both low-

Table 1. Resorption, colours, and habit of 124 non-fibrous Kasai River diamonds (resorption classification follows the scheme of McCallum et al., 1994).

Physical characteristic	#
Resorption	
1	33
2	4
3	11
4	16
5	37
6	18
Unknown	5
Colour	
Colourless	49
Brown	37
Yellow	17
Pink	9
Green	9
Grey	3
Habit	
Octahedron	49
Dodecahedron	35
Polycrystalline aggregate	13
Cube or cubo-octahedron	12
Macle	10
Unknown	5
Fibrous or fibrous coated	14*

*Fibrous and fibrous diamonds are not categorized in colour or resorption.

Table 2. Summary of Kasai River alluvial diamond inclusion phases and parageneses.

Inclusions Species	# diamonds	# inclusions	Bulk composition
Olivine	15	41	Peridotitic
Orthopyroxene	1	1	Peridotitic
Olivine + Orthopyroxene*	7	23 + 14*	Peridotitic
Clinopyroxene	4	13	Eclogitic
Garnet	1	6	Eclogitic
Garnet + Clinopyroxene*	1	7 + 1*	Eclogitic
Total	29	106	

*Addition symbols indicate the number of each phase within diamonds bearing two phases.

Cr garnet and omphacite. None of the analyzed inclusion grains are zoned.

Olivine is the most abundant mineral inclusion of the alluvial sample set. A total of 64 olivine inclusions from 22 diamonds were identified through energy-dispersive X-ray spectroscopy (EDS), though only 51 of 20 diamonds were large enough to yield wavelength-dispersive X-ray spectroscopy (WDS) analyses with sufficiently high totals. Mg# ($100 * \text{molar Mg}/(\text{Mg}+\text{Fe})$) of the olivine inclusions ranges from 90.6 to 94.6 with a mean of 93.1. This mean Mg# lies closer to the identified mean Mg# of the harzburgitic (93.2) than the lherzolitic (92.0) olivine diamond inclusions of the worldwide dataset compiled in Stachel and Harris (2008) (Figure 3). One diamond (11961) shows large heterogeneity in olivine Mg#, with a single inclusion towards the rim of the diamond measured at 90.6 in contrast to six other olivine whose Mg# averaging 93.1 (Appendix B). All other olivine bearing diamonds show less than 0.5 difference in Mg#, often less than 0.3, between olivine inclusions.

Orthopyroxene is the second most abundant inclusion phase, with 15 inclusions analyzed from eight diamonds. Al_2O_3 and Cr_2O_3 are strongly correlated with one another ($r = 0.90$, Figure 4A). Al_2O_3 content of 13 of the inclusions is less than 1.5 wt.% suggesting their equilibration with garnet, while two inclusions from a single diamond exceed 1.5 wt.% Al_2O_3 suggesting their equilibration with spinel (Boyd et al., 1997). The diamond that hosts both of the orthopyroxene inclusions of Al_2O_3 exceeding 1.5 wt.% also hosts an orthopyroxene inclusion of less than 1.5 wt.% (0.97 wt.%). Mg# of the orthopyroxene inclusions ranges from 91.6 to 94.0 with a mean of 93.7 (Figure 4B), slightly higher than the average Mg# of the olivine. Orthopyroxene analyses broadly occupy the same Mg#-CaO space defined by other worldwide orthopyroxene diamond inclusions from cratons worldwide (Figure 4B) and cluster near the overlap of harzburgite and lherzolitic parageneses (Stachel and Harris, 2008). One Ca-rich orthopyroxene (CaO = 0.93 wt.%) lies outside the defined fields.

Clinopyroxene is the third most abundant inclusion phase with 14 inclusions from five diamonds. Mg# of the clinopyroxene ranges from 63.9 to 77.1, with an average of 71.6. Calculation of a jadeite end member as the average of Al^{VI} and Na cations yields a significant component thereof for all clinopyroxene grains (min=10.7, max=27.3, mean=18.9 mole percent). The low Mg#, significant jadeite component, low Cr (maximum 0.21 wt.% Cr_2O_3) and elevated Al (minimum 5.06 wt.% Al_2O_3) of clinopyroxenes assign them to an eclogitic paragenesis. Na is present in concentrations ranging from 0.21 to 0.47 and Al from 0.22 to 0.63 (both on a 4 cation unit basis). Clinopyroxene with lower concentrations of Na and Al host them in nearly 1:1 cation ratios, whereas grains with higher contents of both tend to host excess Al cations over Na cations (Figure 5). This excess Al is attributed to Tschermak clinopyroxene endmembers and is calculated as such within the scheme of Cawthorn and Collerson (1974). Potassium oxide is present in concentrations up to 0.58 wt.%, mean = 0.27 wt.%. Magnesium oxide displays the most heterogeneity between diamonds, with a range of 10.5% due to two highly magnesian clinopyroxenes belonging to a single diamond (sample 11664). Those two clinopyroxenes are the only ones present within that diamond. Although they overlap with websteritic compositions in terms of their Na and Al cation concentrations,

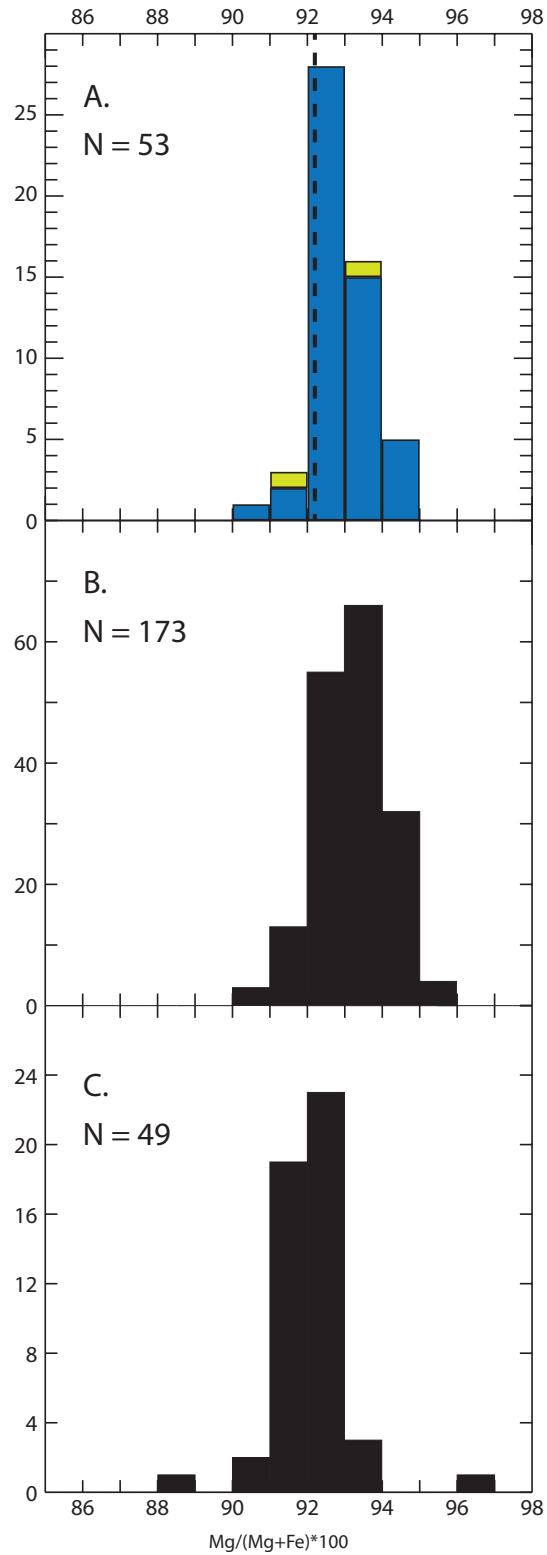


Figure 3. (A) Mg# of olivine inclusions in diamond from alluvial diamonds of the Kasai River, Katanga Province, DRC (blue), and from within diamonds of the Mbuji-Mayi kimberlites (green) of Mveumba Ntanda et al. (1982). Dashed line marks mean Mg# of olivines from peridotitic xenoliths from the Somacuanza kimberlite, central Angola, from Boyd and Danchin (1980). (B) and (C) Mg# of worldwide harzburgitic and lherzolitic olivine diamond inclusions, respectively (after Stachel and Harris, 2008).

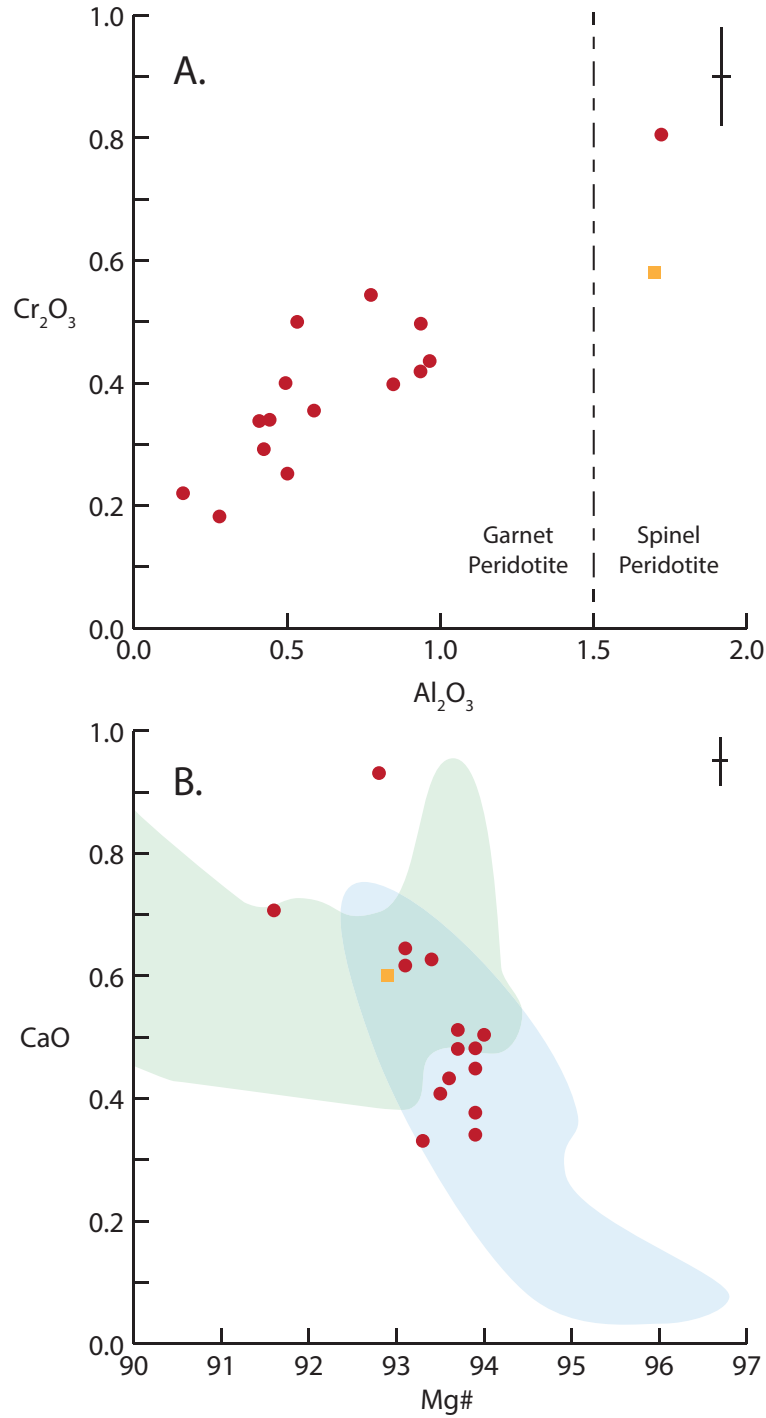


Figure 4. (A) Cr₂O₃ vs. Al₂O₃ of orthopyroxene inclusions from alluvial diamonds of the Kasai River, Katanga Province, DRC (red circles). Orange square indicates the mean analysis of orthopyroxenes from peridotite xenoliths of the Somacuanza kimberlite, Central Angola (Boyd and Danchin, 1980). Dashed line indicates proposed cutoff of Boyd et al. (1997) between orthopyroxenes originating from spinel facies peridotites (higher Al₂O₃ content) from garnet facies peridotites (lower Al₂O₃ content). (B) Mg# vs. CaO of orthopyroxenes from alluvial diamonds of the Kasai River, Katanga Province, DRC. Symbology as in A. Green and blue areas outline compositional fields of lherzolitic and >95% of harzburgitic orthopyroxenes, respectively, within worldwide dataset of Stachel and Harris (2008). Averaged analytical error bars (upper right) calculated using electron microprobe XMasPlus software.

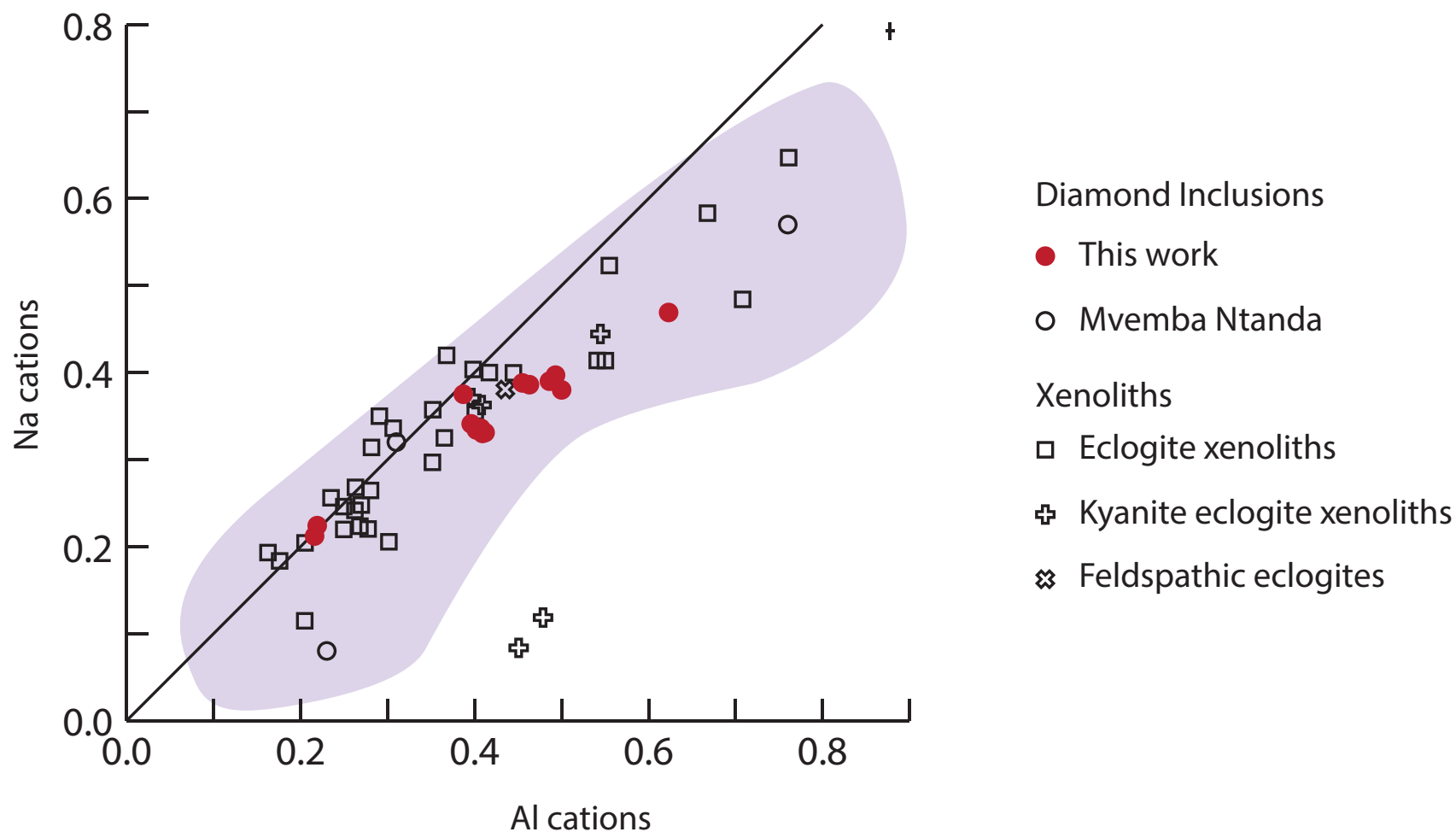


Figure 5. Sodium vs aluminum cations for eclogitic (omphacitic) clinopyroxenes. Closed red circles indicate clinopyroxene inclusions from alluvial diamonds of the Kasai River, Katanga Province, DRC. Solid line indicates a 1:1 ratio. Open circles indicate omphacitic clinopyroxene compositions from diamond inclusions of Mbuji Mayi (Mvemba Ntanda, 1982). Eclogitic xenolith data from Camutue after Boyd and Danchin (1980), Mbuji-Mayi after El Fadili and Demaiffe (1999), Catoca after Roblez-Cruz (2012), and Catoca and Cat-115 after Nikitina et al. (2014). Kyanite bearing eclogitic xenolith data from Chicundo after Boyd and Danchin (1980) and Mbuji-Mayi after El Fadili and Demaiffe (1999). Feldspathic eclogitic xenolith data are from Vale do Queve after Boyd and Danchin (1980). The purple area outlines compositional field of eclogitic diamond inclusion clinopyroxenes within the worldwide dataset of Stachel and Harris (2008). Analytical error bars (upper right) were calculated using electron microprobe XMasPlus software.

their Mg #s (77.0, 77.1) lie closer to the worldwide mean of eclogitic clinopyroxenes (76.8) than that of websteritic clinopyroxenes (83.6; Stachel and Harris, 2008). Aluminum oxide is the next most heterogeneous element with a range of 9.6 wt.%, due to Al_2O_3 content near 5 wt.% in the same highly magnesian clinopyroxenes contrasted with 14.6% in another (sample 11712). For diamonds that contain more than one clinopyroxene inclusion, maximum heterogeneity occurs between the five analyzed clinopyroxenes of sample 11635, with a range of 1.11 wt.% for MgO and 1.07 wt.% for Al_2O_3 . Oxide wt.% range is less than 1% for all other analyzed elements within sample 11635 and for all oxides of all other clinopyroxene within multi-clinopyroxene diamonds.

Garnet is the least abundant inclusion type with 13 inclusions from two diamonds. Only seven were large enough to yield sufficiently high WDS oxide totals. Pyrope garnet Mg# is restricted to 49.7-53.1. Chromium oxide content in garnet inclusions does not exceed 0.75 wt.%. Calcium oxide content ranges from 8.94 to 10.39 wt.%. Titanium oxide is below detection limit in most instances, though averages of 0.71 wt.% a single inclusion. These criteria classify all observed garnets as G3 eclogitic in the scheme of Grutter et al. (2004). Na_2O ranges from 0.23 – 0.48 wt.%, averaging 0.33 wt.% across all analyzed garnet inclusions. Garnet across the suite is most heterogeneous with respect to FeO content (range 2.43 wt.%) and CaO (range 1.46 wt.%), and Al_2O_3 content (range 0.93 wt.%), prior to renormalization. However, garnets belonging to the same diamond are less heterogeneous, with a maximum range of 0.37 wt.% FeO for two analyzed garnets of sample 11712 and a maximum range of 0.80 wt.% Al_2O_3 for five analyzed garnets of sample 11601.

Studied Kasai alluvial diamonds with inclusions are divided into two parageneses. The 23 diamonds bearing inclusions of olivine, orthopyroxene, or both are assigned to peridotitic parageneses. Six diamonds bear clinopyroxene, garnet, or both. Low Mg# and Cr-poor compositions of garnet unambiguously assign them to eclogitic parageneses (Table 2).

5.3 Compositions of fluid inclusions

A total of 48 micro-inclusions across six fibrous diamonds were analyzed via EPMA. The average fluid inclusion composition of each diamond is listed in Table 3. Samples 10274, 11671, MB2-1, and MB2-3 are entirely fibrous and dense with fluid inclusions throughout; sample MB2-6 is fluid inclusion dense except for one clear growth band near its edge; and samples MB2-4 and MB2-5 host fluid inclusions only in thin fibrous coats mantling octahedral growth zones. Renormalization of individual analyses to K+Na, Ca+Fe+Mg, and Si+Al cations indicates that most analyzed inclusions are Si+Al rich (Figure 6). Micro-inclusion compositions resemble some of the most Si+Al rich average fluid compositions identified in previously studied DRC (Navon et al., 1988; Kopylova et al., 2010), Botswanan (Schrauder and Navon, 1994), Guinean (Weiss et al., 2009), Yakutian (Klein-BenDavid et al., 2009), Brazilian (Shiryaev et al., 2005), and some Fox kimberlite, Slave craton (Weiss et al., 2015) diamonds.

Table 3. Averaged composition of fluid inclusions in the fibrous cuboid Kasai River diamonds.

Sample Number	11671	MB2-1	10274	MB2-3	MB2-4	MB2-6
Average of	11	7	6	15	5	4
SiO ₂ , wt. %	45.80	49.38	57.77	60.78	57.13	34.29
TiO ₂ , wt. %	1.45	1.92	2.63	2.78	2.58	1.86
Al ₂ O ₃ , wt. %	4.55	8.96	7.42	6.59	6.85	5.54
FeO, wt. %	8.56	2.42	6.02	4.15	4.02	4.29
MgO, wt. %	6.74	1.77	2.13	0.97	1.61	5.69
CaO, wt. %	5.77	8.42	4.04	2.36	3.56	16.86
SrO, wt. %	1.14	1.19	0.35	0.51	1.02	1.16
BaO, wt. %	1.16	2.31	0.88	2.18	0.93	2.89
Na ₂ O, wt. %	4.78	1.93	1.53	0.77	0.92	2.93
K ₂ O, wt. %	11.77	14.45	14.08	15.79	17.14	16.46
P ₂ O ₅ , wt. %	4.47	4.08	1.84	1.55	2.44	6.21
Cl, wt. %	3.09	2.86	0.95	1.21	1.21	1.41
SO ₂ , wt. %	0.73	0.30	0.36	0.35	0.59	0.42
Total	100.00	100.00	100.00	100.00	100.00	100.00
Total initial, wt %	5.26	5.42	5.59	5.33	5.22	5.33
Si, mol %	18.06	19.40	21.87	23.10	21.86	14.28
Ti, mol %	0.43	0.57	0.75	0.79	0.74	0.58
Al, mol %	2.11	4.15	3.31	2.95	3.09	2.72
Fe, mol %	2.86	0.81	1.93	1.33	1.30	1.51
Mg, mol %	3.96	1.04	1.20	0.55	0.92	3.53
Ca, mol %	2.44	3.54	1.64	0.96	1.46	7.52
Sr, mol %	0.26	0.27	0.08	0.11	0.23	0.28
Ba, mol %	0.18	0.36	0.13	0.33	0.14	0.47
Na, mol %	3.66	1.47	1.13	0.57	0.68	2.37
K, mol %	5.92	7.25	6.80	7.66	8.37	8.74
P, mol %	0.75	0.68	0.29	0.25	0.40	1.09
Cl, mol %	2.06	1.90	0.61	0.78	0.78	0.99
S, mol %	0.27	0.11	0.13	0.12	0.21	0.16
O, mol %	57.04	58.46	60.14	60.49	59.82	55.74
Total	100.00	100.00	100.00	100.00	100.00	100.00

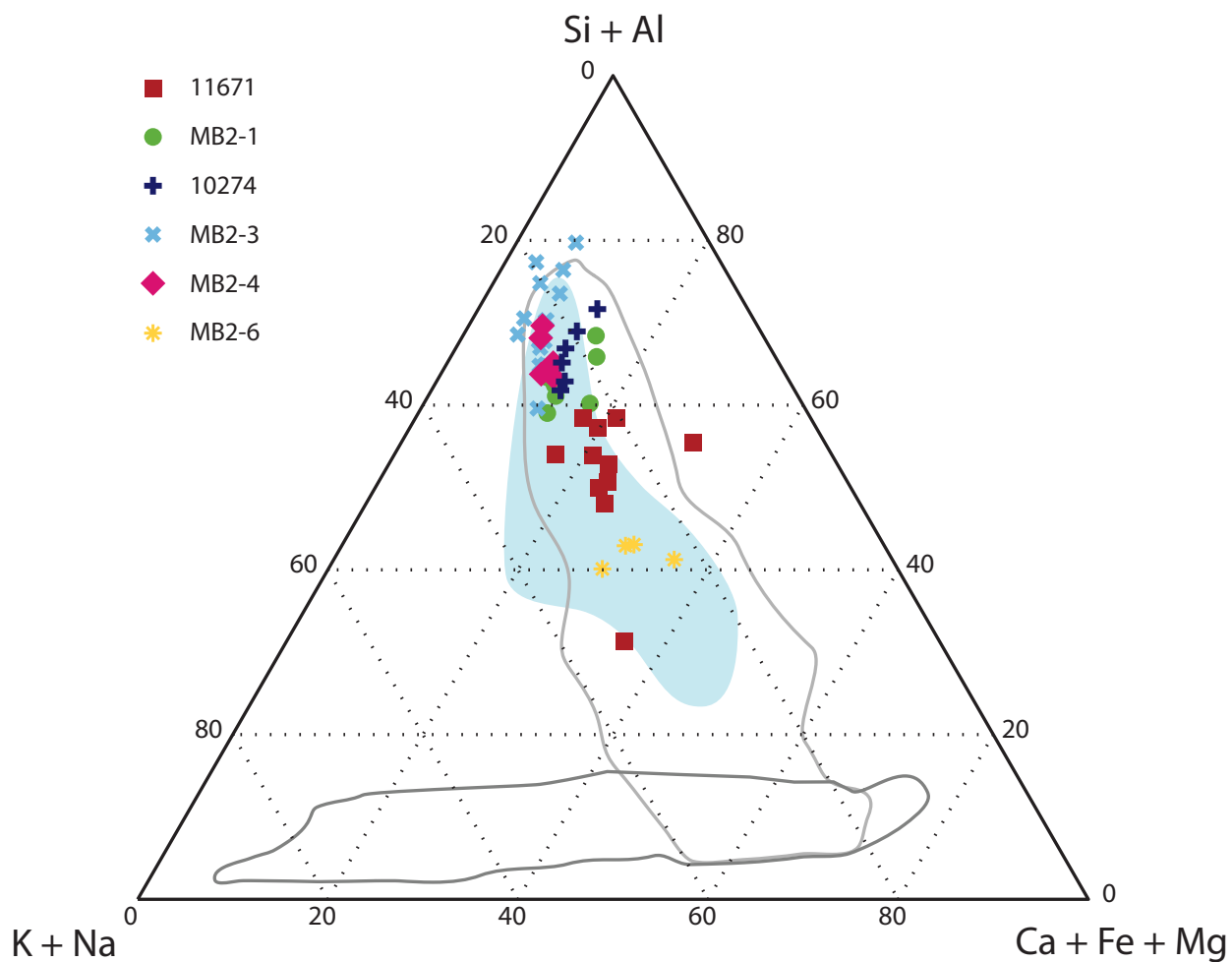


Figure 6. EPMA analyses of inclusions in fibrous diamonds normalized to 100% Si+Al, Ca+Fe+Mg, and K+Na cation components. Global observed compositional fields are from Smith et al. (2012) and references therein. Light blue field outlines observed compositions of Zaire cubic diamonds fluid inclusion compositions after Navon et al. (1988) and Kopylova et al. (2010).

Each diamond is relatively restricted in the composition of its micro-inclusions, with most micro-inclusion analyses deviating by no more than $\pm 10\%$ from their host diamonds' mean normalized Si+Al content. Less deviation from mean diamond composition is present for K+Na and Ca+Fe+Mg content. The clear exceptions to this trend are two analyses from diamond 11671, one with anomalously low Si+Al content and another with anomalously low K+Na. These analyses may represent accidental entrapment of solid or mixed solid and fluid material, rather than pure daughter minerals, or bias introduced by anomalously large daughter minerals (Izreali et al., 2004; Kopylova et al., 2010). No systematic chemical trends with CL identified growth zones are observed for any of the six diamonds.

5.4 N analysis using different techniques: comparison between FTIR and SIMS

Thirty-one octahedral diamonds were measured for [N] both through deconvolution of FTIR spectra (Rio Tinto, 2014) and through SIMS spot analyses within growth zones identified with CL. The analyses provide an opportunity to compare the two methods of [N] analysis. Twenty-eight diamonds show agreement between the determined SIMS [N] range and bulk [N] determined through spectra deconvolution, while for 2 diamonds (11655 and 11738) the [N] analyses do not match. In both instances, the bulk calculated [N] exceeds the maximum [N] determined from SIMS spot analyses. Both diamonds have very low [N] determined by both methods. Sample 11655 ranges from 1.0 to 10.3 ppm nitrogen in its spot analyses and bulk [N] was calculated as 40 ppm. Sample 11738 similarly ranges from 0.8 ppm nitrogen to 46.4 ppm, whereas bulk [N] is calculated as 55 ppm.

The distributions of SIMS spot analyses within samples 11655 and 11738 sufficiently cover their respective growth zones identified in CL. Thus, having missed a growth zone of higher [N] exceeding the bulk calculated [N] seems unlikely. Rather, spectra deconvolution overestimates [N] content for diamonds of low [N]. Spectra deconvolution methods examine any residual difference between baseline corrected, normalized spectra and 0 at the wavenumbers corresponding to $[N]_A$ and $[N]_B$ as peaks and output [N]. Therefore, higher bulk [N] calculated by FTIR in diamonds of low [N] are perhaps indicative of non-linear baseline contributions.

The FTIR spectra of sample (11699) went off scale as a result of large sample thickness and high actual [N] so its peaks could not be deconvoluted. I estimate bulk [N] in excess of 1000 ppm. SIMS data indicates the diamond ranges from 10.8 ppm to 1314.9 ppm [N], with the majority of growth zones (and therefore diamond volume) in excess of 760 ppm [N]. Therefore, this sample's FTIR [N] and SIMS [N] are in agreement.

The overall match between spectra deconvolution and direct measurement of [N] is sufficiently robust, considering that the former relies on a visual estimation of baseline and spectra fit, that bulk calculated [N] will provide a reasonably accurate value for use in nitrogen geothermometry.

5.5 Nitrogen characteristics and nitrogen geothermometry

Infrared spectra were obtained for 33 octahedrally grown diamonds. Nitrogen occurs in the diamond lattice as single or aggregated atoms. Nitrogen is first incorporated into the diamond structure as C-centers (isolated nitrogen atoms). These C-centers convert relatively quickly to A-centers (paired nitrogen atoms), followed by B-centers (four nitrogen atoms surrounding a vacancy), the latter two of which absorb in the infrared region (Taylor et al., 1990, 1996). The infrared absorbance peaks corresponding to A- and B-centers were deconvoluted using the Rio Tinto (2014) spreadsheet. Calculated [N] varies from 25 ppm to 600 ppm, with an average of 230 ppm. [N] appears bimodal, with a large mode near 100 – 149 N ppm and a lesser mode near 350 – 399 ppm. The degree to which total nitrogen is aggregated into B-centers (denoted hereafter as % $[N]_B$) ranges from 0 to 88%. % $[N]_B$ also appears bimodal, with a mode near 40 – 50% $[N]_B$ and a second mode larger mode at 60 – 70%. No linear correlation is present between calculated [N] and % $[N]_B$ ($r = 0.08$). Diamond of eclogitic parageneses, on average, contain both more nitrogen and greater proportion of [N]B than diamonds of peridotitic or unknown parageneses (Figure 7). All but one analysis, a rim analysis yielding 2962 [N] ppm, contain less than 1350 [N] ppm. Most fibrous diamond [N] ppm content ranges from 957 to 2160 ppm, with two exceptions on the high end of the range (2402 and 2976, belonging to the core of the same diamond) and two exceptions on the low end of the range (9.4 ppm and 518 ppm, belonging to cores of two different diamonds).

This sequential transformation of nitrogen aggregation state is a function of nitrogen content, mantle storage time, and mantle storage temperature (Taylor et al., 1990). The kinetics of transformation are strongly dependent on mantle storage temperature but weakly dependent on mantle storage time, making for a geothermometer surprisingly consistent with conventional coexisting mineral inclusion geothermobarometer but a poor chronometer; if the diamonds are known to be at least a certain age, calculated temperatures vary little with different assumed mantle residence time inputs (Navon, 1999; Stachel and Harris, 2008).

In order to use the degree of N aggregation to infer mantle temperatures, one should constrain the diamonds' residence time in the mantle based on the geological history of the craton. Tectonic reconstructions of Africa based on field geology and geophysical observations suggest that the SCLM of the Kasai block of the Congo craton had already developed and accreted to the Congo craton prior to 2.7 Ga (Begg et al., 2009). Granulite complexes of the Kasai block are dated at 3.01 Ga (Begg et al., 2009). Whole rock Rb-Sr push the granulite complex ages back to between 3.49 and 3.33 Ga (De Waele et al., 2008). U-Pb dating of crustal zircons from the central Congo craton indicates crust as old as 3.6 Ga (Batumike et al., 2009b). Since the Kasai crust formed 3.01–3.6 Ga, and the underlying mantle is expected to form concurrently with the crust (Pearson and Wittig, 2008), the Kasai SCLM should also have similar ages. However, worldwide ages of peridotitic diamonds as determined by Re-Os chronology go only as far back as 3.3 Ga (Shirey and Richardson, 2011). In the absence of definitive Re-Os diamond ages older than 3.3 Ga, the maximum residence time of peridotitic Kasai diamonds are taken to be 3.2 Ga, given that minimum eruption ages of NW Angolan kimberlites are Early Cretaceous (Roblez-Cruz et al., 2012a, and references therein).

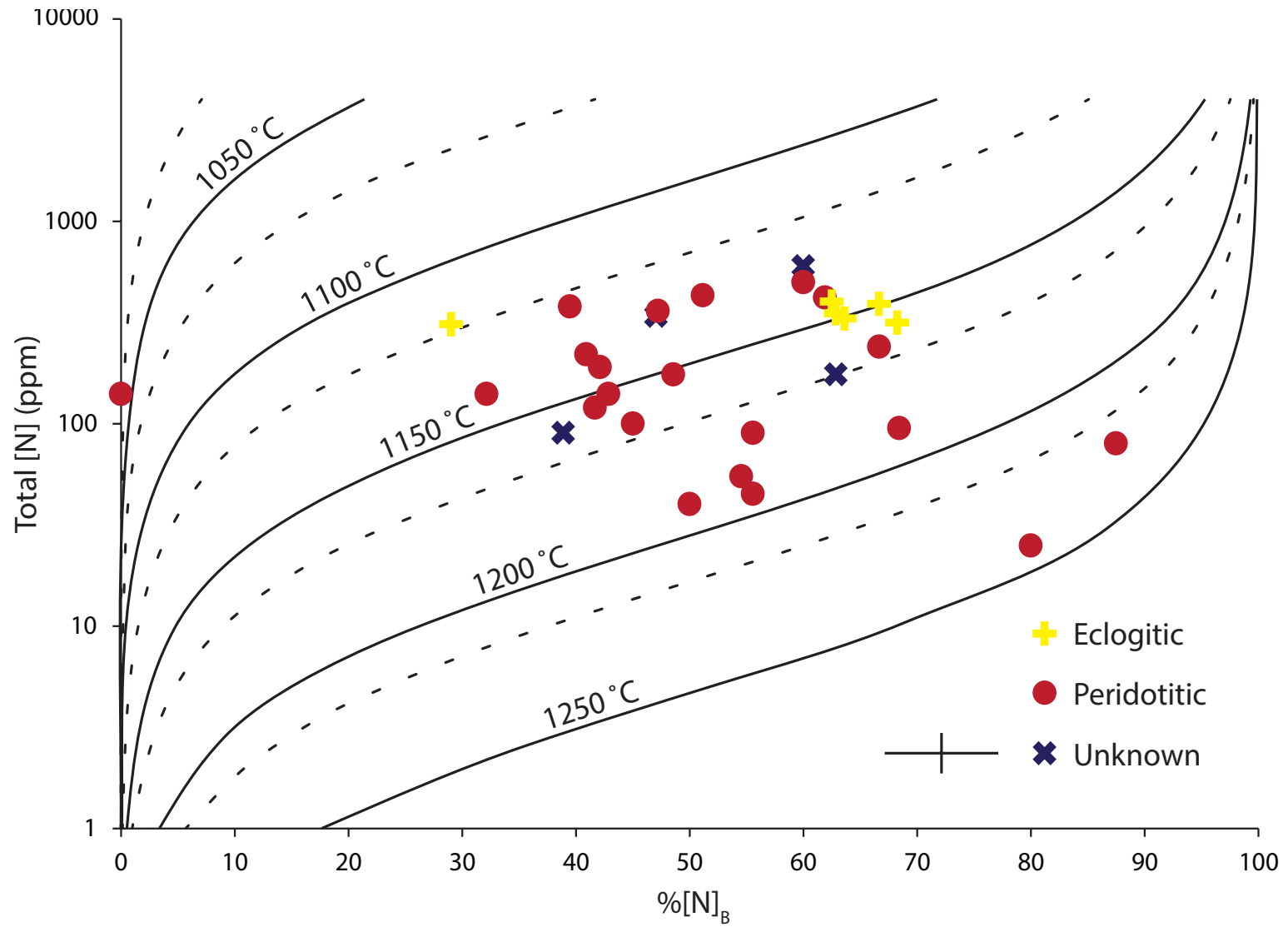


Figure 7. Temperature isotherms as a function of total nitrogen concentration [N] and degree to which nitrogen is aggregated as B-centers (%[N]_B). Isotherms calculated based on the equations of Taylor et al. (1990) and Leahy and Taylor (1997). Solid isotherms calculated assuming a mantle residence time of 3.2 Ga, dotted lines assume a mantle residence time of 900 Ma. See text for discussion of [N] and [N]_B calculation methodologies and justification of mantle residence time. Analytical error bars (lower left) represent $\pm 10\%$ error after Stachel et al. (2002).

Mantle residence time for eclogitic diamonds may be different, since cratonic eclogites are thought to be the product of high pressure metamorphism of a basaltic parent, i.e., subducted MORB (Jacob, 2004). In particular, Nikitina et al. (2014) advocate a subduction origin for Kasai eclogite xenoliths. Diamonds with eclogitic inclusions therefore should have mantle residence times only as old as the difference in age between the most recent subduction events responsible for introducing eclogitic paragenesis to the SCLM and kimberlite eruption ages. In the southern Congo Craton/Kasai block, the last accretionary event was the convergence of the Congo-Tanzania-Bangweulu cratons with the Kalahari cratons at 1.0 Ga (Begg et al., 2009). Older ages of Congo eclogites are constrained by the Kibaran orogeny to the east (1.8 Ga; De Waele et al., 2008; Begg et al., 2009) and discordant 2.97 – 1.24 Ga ages of zircon in eclogitic xenoliths of the Catoca kimberlite (Nikitina et al., 2014). However, global Re-Os dating of eclogitic sulfide inclusions in diamonds indicate an absence of eclogitic diamonds younger than 900 Ma (Shirey and Richardson, 2011). Therefore, minimum mantle residence time is inferred to be 900 Ma.

Figure 8 displays mantle storage temperature isotherms as a function of nitrogen content and $\%[N]_B$ center for ages of 3.2 Ga and 900 Ma. Comparison of the two assumed mantle residence times indicate temperature discrepancies of less than 50 °C in for any given diamond. Therefore, diamond resided at time-averaged temperatures between 1000 to 1278 °C if the residence time was 0.9–3.2 Ga.

5.6 Composition of carbon isotopes and their relationship to [N] characteristics

Carbon isotopic compositions ($\delta^{13}C_{VPDB}$) of 40 diamonds was determined with SIMS spot analyses (Figure 8, Appendix E). Analyses range from -27.3‰ to -1.9‰, with a mean of -5.7‰. Carbon isotopic compositions follow previously established correlations to diamond paragenesis (Cartigny, 2005). Eclogitic diamonds span a wide range of isotopic compositions (-17.8‰ to -3.4‰, mean -8.29‰), whereas peridotites are restricted to heavier values (-12.5‰ to -1.9‰, mean -3.9‰). Non-fibrous diamonds of unknown paragenesis may comprise some of both, given the range from -27.3‰ to -3.1‰ (mean -12.35‰). Fibrous diamonds are restricted to -9.3‰ to -4.1‰.

Octahedral diamonds with peridotitic inclusions and diamonds of fibrous growth habits (parageneses unknown) display relatively restricted $\delta^{13}C$ and [N] ranges (Figure 8). All but three spot analyses of peridotitic octahedral diamonds are between -6‰ to 0‰ $\delta^{13}C$. The exceptions are diamond core analysis at -12.48‰, and two analyses from the same core of a different sample at -8.53‰ and -8.03‰. Fibrous diamond spot analyses have lower $\delta^{13}C$ but with a similar overall range from -9.3 ‰ to -4.1‰.

Octahedrally grown eclogitic diamonds are less restricted in their $\delta^{13}C$ isotopic composition. Three of five eclogitic diamonds (17 spot analyses) are isotopically indistinguishable from the peridotitic diamonds (range -5.37‰ to -3.24‰). The remaining two eclogitic diamonds (5 spot analyses each) are isotopically light, with one diamond ranging from -17.8‰ to -14.3‰ and the other from -13.7‰ to -13.0‰. [N] of spot analyses of five eclogitic diamonds is lower than the maximum of peridotitic diamonds, ranging from

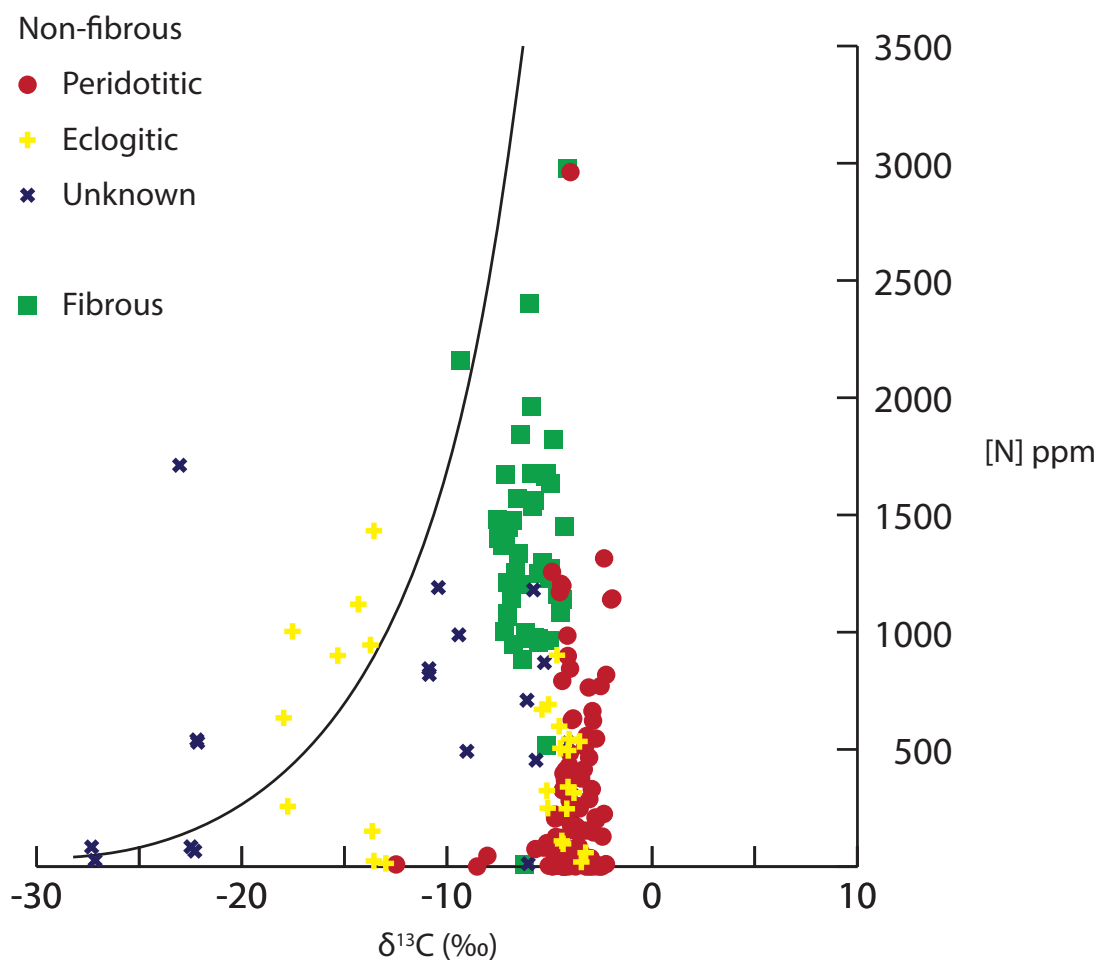


Figure 8. Carbon isotope composition ($\delta^{13}\text{C}$) vs [N] ppm for 221 points analyzed via SIMS for alluvial diamonds of the Kasai River, Katanga Province, DRC. Red circles indicate analyses from octahedral diamonds, yellow crosses from eclogitic diamonds, blue crosses from diamonds of unknown paragenesis, and green squares from fibrous cuboid diamonds. Solid line is the “limit sector” curve of Cartigny et al. (2001), an empirically formulated maximum [N] content for a given $\delta^{13}\text{C}$ value of diamond.

14 ppm to 1432 ppm.

Diamonds of unknown paragenesis display both the most overall and intrastone variation in their $\delta^{13}\text{C}$ composition. One of the four diamonds overlaps with the peridotitic and two eclogitic diamonds (range -4.1‰ to -3.1‰). A second diamond is isotopically light (-10.9‰ to -9.0‰) and a third sample uniformly lighter than all others (-23‰ to -22.1‰). Another diamond of unknown paragenesis is both the most isotopically light sample (two spot analyses in the core of the diamond measure -27.2‰ and -27.3‰) and by far displays the most intrastone variation (-27.3‰ to -5.25‰). The most isotopically light values (-27.15‰, -27.32‰) occur within the most interior, unresorbed growth zone of sample 11733 (Figure 9c). The second growth zone is isotopically heavier (-5.78‰, -5.25‰, -6.10‰ from core to rim) and resorbed, followed by a similarly isotopically heavy, lightly resorbed growth zone (one analysis of -6.04‰) and unresorbed coating (one analysis of -5.66‰).

Linear correlation coefficients between $\delta^{13}\text{C}$ and [N] ($p = \text{cov}(\delta^{13}\text{C}, [\text{N}]) / \sigma_{\delta^{13}\text{C}} \sigma_{[\text{N}]}$) for each diamond vary widely. Most samples display a strong to moderately strong negative correlation between the two values (15 samples correlation coefficient between -1 and -0.6). Carbon isotopic composition and [N] are also weakly negatively correlated within samples (-0.6 to -0.2, 11 samples), weakly positively (0.2 to 0.6, 6 samples), or moderately strong positive correlation (0.6 to 0.8, 6 samples).

5.7 Cathodoluminescence

Both the sample suite as a whole and individual samples are very heterogeneous in cathodoluminescent brightness. Very broadly, spot analyses taken in regions of dim cathodoluminescence in octahedral zones yield low [N] and those within regions of bright cathodoluminescence yield high [N]. There are many exceptions to this rule, however, particularly when the growth zone has fine oscillations in CL character. Large variations in [N] may be present within single diamonds whose CL characteristics appear relatively uniform. Spot analyses taken in growth zones with a mottled CL appearance (e.g. Figure 9f, spot 6) generally have [N] less than 100 ppm, often much less, though unmottled growth layers from the same diamonds often rival these values. Fibrous diamonds are many times dimmer in CL than their octahedrally grown counterparts despite their high average [N]. Additionally, the fibrous diamonds are significantly more uniform in CL character. No systematic variation of $\delta^{13}\text{C}$ as a function of CL brightness is observed.

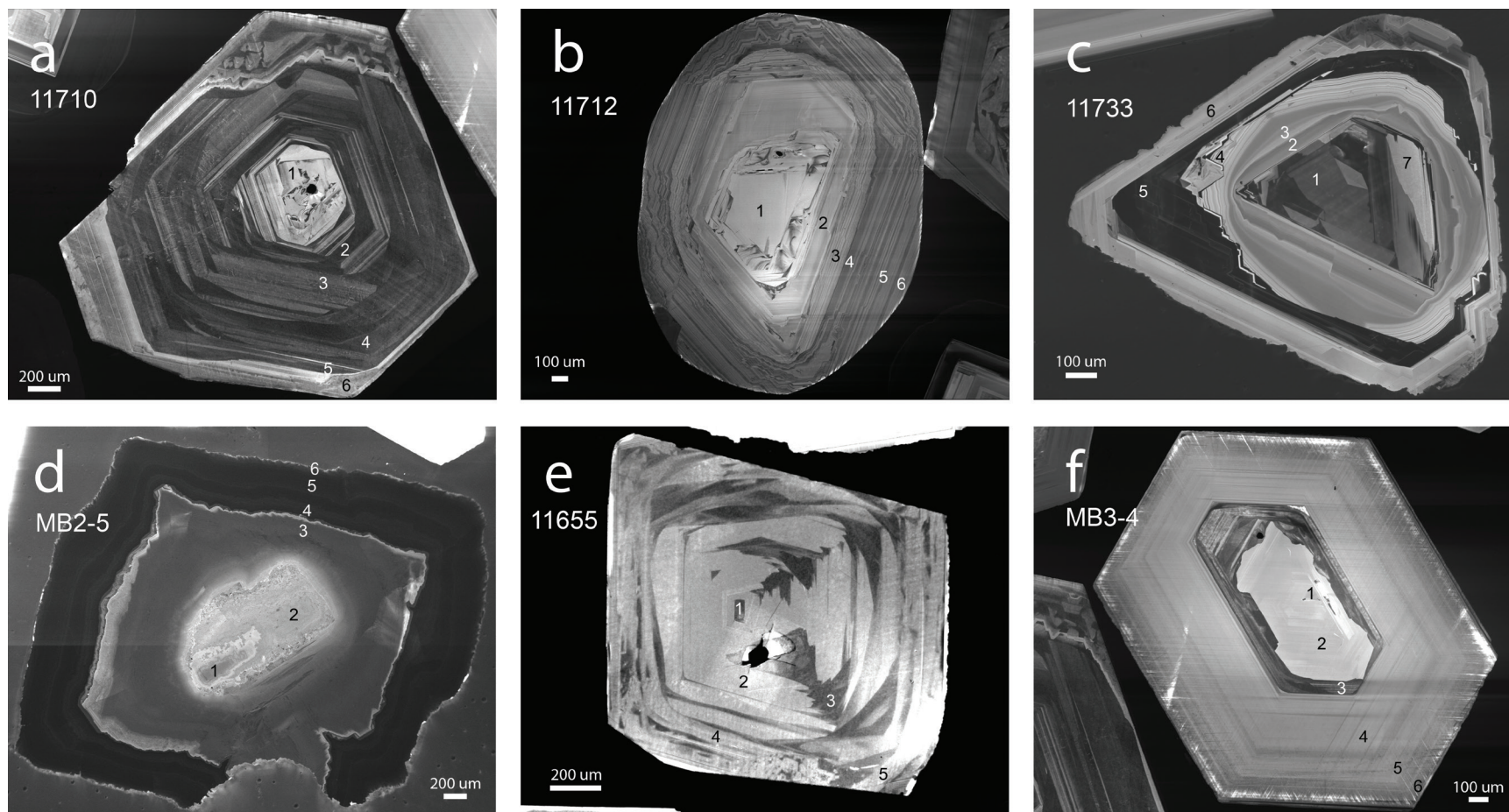


Figure 9. Representative cathodoluminescence (CL) images of six polished alluvial diamonds of the Kasai River, Katanaga Province, DRC. Numbers correspond to points at which $\delta^{13}\text{C}$ and [N] ppm were analyzed via SIMS (see Methodology and Appendix E). Sample MB2-5 (D) is a fibrous cuboid diamond, all other images are of octahedrally-grown diamonds. Sample 11733 (C) exhibits extreme variation in carbon isotopic composition between growth zones from -27.32 ‰ and -27.15‰ at points 7 and 1, respectively, to -5.25 ‰ at point 3.

6. Discussion

6.1 Sources of Diamond Carbon and Their Variation

Observed carbon isotopic compositions of the studied Kasai diamonds follow the known general patterns for diamond sources worldwide. It has been observed globally that diamonds belonging with both peridotitic and eclogitic affinities bear $\delta^{13}\text{C}$ isotopic signatures clustering near -5‰ (Javoy et al., 1986; Cartigny, 2005; Stachel et al., 2009), coinciding with isotopic values observed for mantle derived melts and the mantle itself (Javoy et al., 1986). Finer subdivision of peridotitic and eclogitic parageneses has suggested multiple closely spaced modes in the -5.75‰ to -3.50‰ range, with distinct modes for harzburgitic and lherzolitic parageneses (Stachel et al., 2009). Additionally, individual cratons bear distinct $\delta^{13}\text{C}$ modes (e.g., Cartigny, 2005; Miller et al., 2012). Diamonds belonging to eclogitic and websteritic parageneses are much less restricted in carbon isotopic composition than their peridotitic counterparts and feature more depleted isotopic compositions (Cartigny, 2005; Stachel et al., 2009), down to -41 ‰ for the northern Slave craton (De Stefano et al., 2009). Isotopic compositions depleted in ^{13}C are thought to broadly reflect subducted organic carbon-rich sediment bearing sources (Sobolev and Sobolev, 1980; Milledge et al., 1983) whose isotopic composition averages -25‰ (Schidlowski, 2001) since at least the time of onset of subduction inferred from the first appearance of diamond-bearing eclogitic parageneses (Shirey and Richardson, 2011). Based on these correlations between diamond paragenesis with $\delta^{13}\text{C}$ and identification of a significant component of eclogitic parageneses comprising northern Angolan SCLM, two diamonds of unknown paragenesis (due to an absence of silicate inclusions) with growth zones bearing $\delta^{13}\text{C}$ values -27‰ and -23‰ may reasonably be assigned to eclogitic affinity. A third diamond of unknown paragenesis averaging -10.1‰ and a fourth averaging -3.8‰ may not unambiguously be assigned a paragenesis. At least 10% of the suite can be assigned to an eclogitic paragenesis on the basis of their $\delta^{13}\text{C}$ characteristics.

Carbon isotopic signatures of Kasai fibrous coats and fibrous diamonds form an array distinct from octahedrally grown diamonds (-4.39‰ to -9.34‰, mean -6.07‰, see Figure 8), as do all other known fibrous diamonds (Cartigny, 2005; Klein-BenDavid et al., 2010). Their $\delta^{13}\text{C}$ close to that of mantle carbon but slightly lower, i.e., shifted towards subducted sediment $\delta^{13}\text{C}$, suggests that fibrous diamond fluids form from a mixture of the two sources. These isotopic signatures likely do not reflect original seawater carbon isotopic ratios; Archean seawater (one proposed time of significant subduction) $\delta^{13}\text{C}$ as ascertained from carbonates falls near mantle values (-1.5‰ \pm 1.5‰; Veizer et al., 1989), and carbonates of Mesoproterozoic age (e.g., the Kibaran orogeny) are also near mantle values ($0 \pm 2\%$ at 1.9 Ga to $-1 \pm 1.5\%$ at 1.65 Ga; Veizer et al., 1992). Fibrous diamonds form largely from mantle carbon, not from the crustal carbon that may have been transported with the crust.

Many diamonds within the suite show some degree of carbon isotopic heterogeneity. All but two diamonds are restricted to $<5\%$ $\delta^{13}\text{C}$. A peridotitic diamond spans isotopic values of -12.48‰ to -3.62‰, with the lightest analysis concentrated in the core and the heavier values averaging -3.87‰. Another diamond within the suite is the single most isotopically heterogeneous diamond known to date worldwide,

with a core averaging -27.2‰ (2 analyses) and a rim averaging -5.8‰ (5 analyses). For both diamonds with large $\delta^{13}\text{C}$ ranges, minimum and maximum values belong to different growth zones observed within CL imaging. Prior investigations of single diamond $\delta^{13}\text{C}$ isotopic heterogeneity have yielded isotopic variation between growth zones typically on the order of 4‰ (Swart et al., 1983; Javoy et al., 1984; Otter et al., 1991; Harte and Otter, 1992; Fitzsimmons et al., 1999; Harte et al., 1999; Zedgenizov et al., 2006; Shatsky et al., 2008; Smart et al., 2011; Wiggers de Vries et al., 2013a). Larger heterogeneities have seldom been observed; these include a Mir octahedral diamond with 10‰ difference between core and rim (Wiggers de Vries et al., 2007), an 11.5 ‰ difference in a Venezuelan diamond (Schulze et al., 2004), and heterogeneity of 15‰ in a Botswanan diamond between its octahedrally grown core and fibrous coat (Boyd et al., 1992).

A number of processes have been invoked to explain carbon isotope variation within individual diamonds. Rayleigh fractionation has attracted significant attention as a potential means by which to produce isotopic heterogeneity in diamond (Cartigny et al., 2001). The $\delta^{13}\text{C}$ composition of diamonds precipitated by fluids undergoing Rayleigh fractionation is controlled by the redox state of the fluid from which diamond precipitates, wherein growth of diamonds from reduced carbon species (i.e., methane) produces diamond with progressively ^{13}C depleted compositions and growth of diamonds from oxidized species (i.e., CO_2 or CO_3^{2-}) the opposite (Deines, 1980). In the two cases of unprecedented heterogeneity, the cores of the diamonds are lighter than their more exterior growth zones so only precipitation from oxidized media is of consideration. Additionally, the CO_2 escape model of Cartigny et al. (2001) is ignored because it only produces progressively lighter isotopic compositions and cannot operate in olivine bearing parageneses (Stachel et al., 2009).

Smart et al. (2011) modeled the frequency of $\delta^{13}\text{C}$ of diamonds precipitated at 1100°C in Rayleigh fractionation processes from both reduced fluids/melts (based on Richet et al., 1977) and oxidized fluids/melts (based on Chacko et al., 1991). Progressively less abundant heavier isotopic signatures are produced through Rayleigh fractionation of oxidized media, essentially tapering off to negligible volumes beyond +7‰ of the isotopic composition of the initial media (Smart et al., 2011). If the model of Smart et al. (2011) is shifted to fluids/melts starting at -27‰ and -12.5‰, one would expect essentially no diamond heavier than -20‰ and -5‰, respectively, to precipitate from these initial fluid/melt compositions. Therefore, Rayleigh fractionation cannot account for the high degrees of heterogeneity and for sharp changes between the isotopic compositions of the adjacent zones observed within some of the Kasai alluvial diamonds.

I attribute formation of diamonds with strongly dissimilar $\delta^{13}\text{C}$ growth zones to precipitation in distinct episodes from distinct sources. A similar process was proposed by Wiggers de Vries et al. (2013a) for Yakutian diamonds. The authors argued this on the basis of markedly different nitrogen aggregation states between growth zones and differential Re-Os ages within zonally distributed sulfide inclusions (Wiggers de Vries et al., 2013b).

6.2 Composition of Diamond Forming Fluids

Fluid inclusions trapped within diamonds provide the best constraints on the composition of diamond forming fluids. The 48 micro-inclusions analyzed across the six diamonds range from 31.3% to 79.7% Si + Al cations when renormalized to the end members Si + Al (silicic), Mg + Fe + Ca (carbonatitic), and K + Na (saline) (Figure 6, Table 3).

Few prior studies have investigated compositions of the crystallized fluids trapped within fibrous diamonds from the Congo craton. Navon et al. (1988) and Kopylova et al. (2010) used similar EPMA methods to investigate the compositions of fluid inclusions from DRC fibrous diamonds, most of which, if not all, are from the kimberlites of Mbuji-Mayi. The compositional overlap between Kasai fluid inclusions and those from the DRC, and the absence of carbonatitic and saline fluid compositions jointly from the Kasai and DRC diamonds, suggest homogeneity in the diamond fluid compositions despite their distance in space (~300 km) and time with Catoca eruption at 117.9 ± 0.7 Ma (Roblez-Cruz et al., 2012a), and Mbuji-Mayi at 70 Ma (Schärer et al., 1997). The age of the diamond-forming fluids is constrained by the poorly aggregated N in fibrous diamonds to ~5 Ma prior to the kimberlite formation (Navon, 1999; Smith et al., 2012). Although fibrous Kasai diamonds were not characterized in terms of N aggregation, they are likely to be similar to all other fibrous diamonds globally with all N aggregated as A-centers.

In the absence of systematic EPMA fluid inclusion study of spatially distributed kimberlites, we cannot assess whether this uniformity in the fluid composition is the norm or the exception; the Slave craton provides the only comparable example. Studies of fibrous diamond fluid inclusions from the Diavik kimberlite (Klein-BenDavid et al., 2007), Ekati Panda kimberlite (Tomlinson et al., 2006), and Ekati Fox kimberlite (Weiss et al., 2015) emplaced between 70 Ma and 45 Ma (Creaser et al., 2004; Schmidberger et al., 2007) within 40 km of one another are compositionally inhomogeneous; Panda yields compositions transitional between saline and silicic compositions, Diavik yields carbonatitic compositions, and Fox yields both silicic and transitional saline-carbonatitic compositions. Thus, the central Slave mantle in the Paleogene produced diamonds from widely varying fluids, unlike the Cretaceous Angolan mantle. To understand the factors controlling the homogeneity or heterogeneity of the diamond-forming fluids, we turn to a recent model of Weiss et al. (2015).

The geochemistry of fluid inclusions within diamonds is a function of their source and their subsequent interaction with SCLM lithologies. Based on investigations of initial Sr isotope ratios and trace element patterns of trapped fluid inclusions, saline (Na + K rich) fluids are parental to both carbonatitic and silicic fluid inclusions; saline compositions evolve towards carbonatitic compositions upon interaction with peridotitic lithologies, whereas interaction with eclogitic lithologies produce silicic compositions (Weiss et al 2009, 2015). Weiss et al. (2015) point to dehydration reactions within subducting slabs as the key mechanism for carbon-bearing fluid genesis and subsequent diamond growth upon their ingress into overlying SCLM. However, the model does not explain why fibrous diamonds that include crustal fluids are made from mantle, rather than crustal carbon (based on mean mantle $\delta^{13}\text{C} = -5\text{‰}$).

If we accept the model of Weiss et al. (2015), fibrous diamonds and fibrous coats from northeastern Angola and those previously studied from Mbuji-Mayi (Navon, 1988; Kopylova et al., 2010) record interaction with eclogitic lithologies underlying the Congo Craton. The absence of fluid compositions other than silicic in the DRC and Kasai diamonds thus far suggest that eclogites comprise a volumetrically significant part of rocks parent to diamond in the Congo SCLM and the eclogites fully reacted with an initial saline fluid. Weiss et al. (2015) hypothesize that the source of fluids to Slave craton fibrous diamonds are related to low angle subduction of the Farallon plate starting in the Mesozoic (Currie and Beaumont, 2011). Perhaps it is the relatively recent sequence of events of subduction, fibrous diamond formation, and kimberlite eruption in the Slave that is responsible for its fluid inclusion diversity. Subducted fluids beneath the Kasai block may have had longer time to interact with SCLM lithologies and therefore transform their possibly once saline composition to silicic, whereas primitive fluid inclusions survive within the Slave suite. Eclogitic xenoliths of the Congo (Nikitina et al, 2014) are dated at Paleoproterozoic. The most recent basin closure and associated subduction recorded within the 550 – 520 Ma Damara belt to the South of the Kasai craton (John et al., 2004; Johnson et al, 2007) provides the possible oldest age of subducted-related fluids introduced into the Congo mantle. Thus, the longer time between the introduction of the crustal fluid via subduction and the diamond-generation below Congo (550 Ma – 120 Ma) may have contributed towards the fluid homogeneity compared to the Slave, where the time between the Mesozoic influx of fluids and Paleogene diamond formation was shorter. Longer residence of the fluid in the mantle may have ensured its buffering by the host mantle lithologies. Additionally, we can deduce the evolution of diamond parent rocks over time. Old octahedral diamonds with aggregated [N] from Kasai are 67% peridotitic and 19% eclogitic (remainder unknown parageneses), whereas younger fibrous diamonds are fully eclogitic. This indicates that eclogitic parageneses became more significant diamond host rocks in the Congo SCLM through time.

6.3 Thermal State of the Congo Craton in the Cretaceous

Temperature estimates based on N aggregation of diamond, together with traditional mineral thermobarometry for diamonds and mantle xenoliths, constrain the thermal state and the minimal lithosphere depth of the Congo craton in the Cretaceous.

The studied Kasai River diamond suite produced only one diamond (11712) amenable to thermobarometry, in which garnet coexists with omphacite. Temperatures of equilibration for the garnet (two grains, one an average of two analyses and the other a single analysis) and clinopyroxene (one analysis) at 50 kbar using the geothermometer of Nakamura (2009) are 1303 °C and 1318 °C, i.e., within 25 °C from one another. By the thermometer of Krogh (1988), the temperatures are shifted to 1331 °C and 1346 at 50 kb, respectively, placing them in the upper 20% of the normal distribution of eclogitic DI inclusions worldwide (Stachel and Harris, 2008). A more accurate thermobarometric constraint on diamond 11712 can be made by drawing univariant PT lines that correspond to the coexisting average garnet-clinopyroxene pair using the Nakamura (2009) thermometer (thick solid line on Figure 10) and the Beyer et al. (2015) barometer (dot-dashed line on Figure 10). The intersection of the two univariant lines indicates a pressure-tempera-

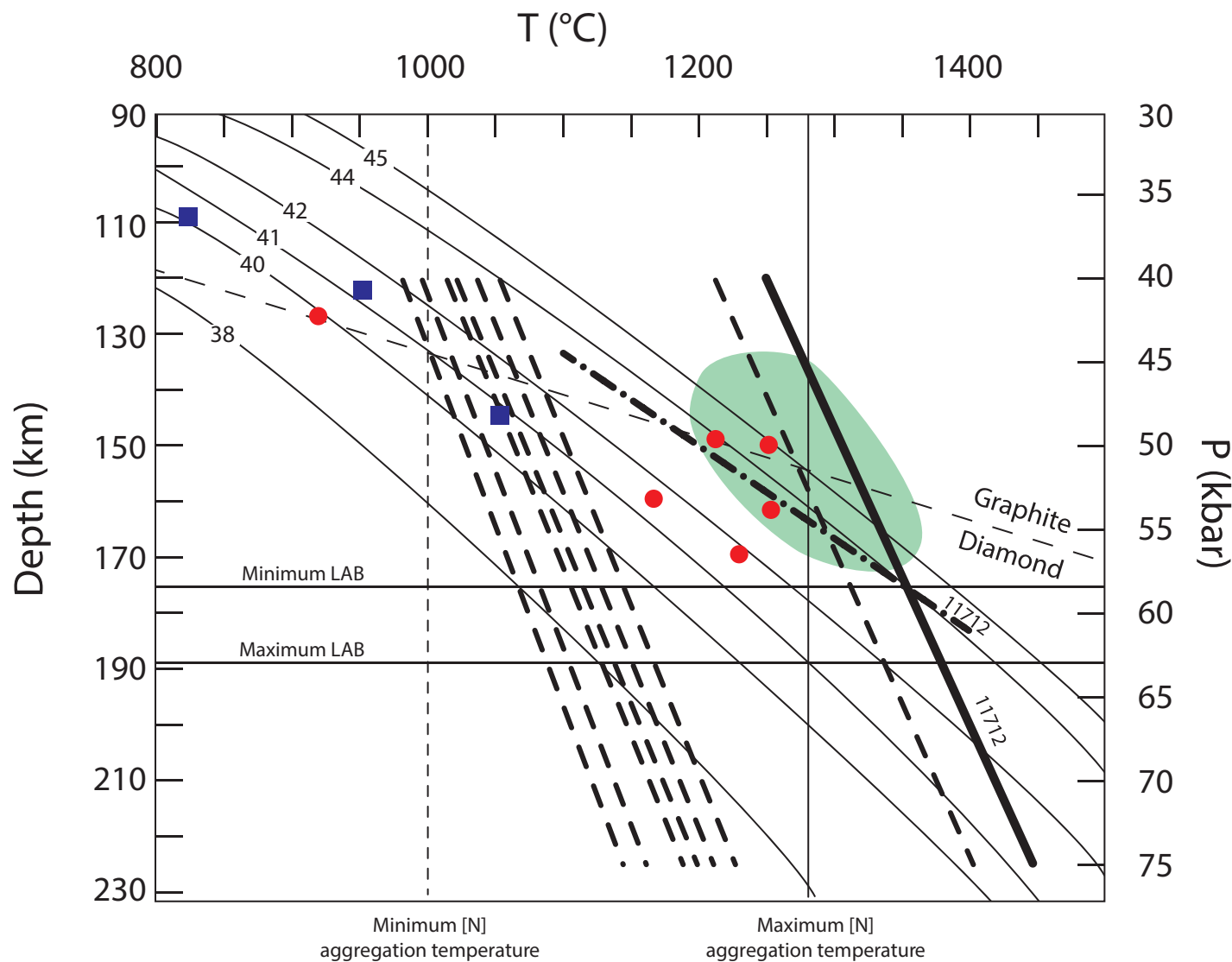


Figure 10. Pressure-temperature diagram of Kasai diamond inclusions with northeast Angola mantle xenolith data. Thin solid lines are geotherms after Pollack and Chapman (1977). Thin horizontal dashed line is the graphite-diamond transition after Kennedy and Kennedy (1976). Solid near-vertical line is a univariant PT line calculated using the thermometer of Nakamura (2009) for the garnet-clinopyroxene pair of Kasai diamond 11712. Dot-dashed line is univariant PT line calculated from the barometer of Beyer et al. (2015). [N] aggregation temperatures represent minimum (1000 °C) and maximum (1278 °C) calculated mantle residence temperatures. Red circle and blue squares are garnet lherzolite and garnet phlogopite wehrlite temperatures, respectively, after Roblez-Cruz et al. (2012b), calculated using the thermometer of Nimis and Taylor (2000). Green field represents a majority (>90%) of single clinopyroxene macrocryst temperatures and pressures from kimberlite Cucumbi 79 after Roblez-Cruz et al. (2012b), using Nimis and Taylor (2000). Thick dashed near-vertical lines represent univariant PT lines of eclogite xenolith mineral data (mineral core analyses only) of Nikitina et al. (2014) calculated using Nakamura (2009). The two lines labeled “Minimum LAB” and “Maximum LAB” correspond to the depth of intersection of the Nakamura (2009) and Beyer et al. (2015) univariant PT lines and the depth of intersection of the 41 mW/m² geotherm with the maximum calculated [N] temperature, respectively.

ture coordinate of 58 kb (170–175 km depth), 1350 °C, along the 44 mW/m² geotherm of Pollack and Chapman (1977). This P-T point fits well the field of single clinopyroxene macrocrysts temperatures and pressures from kimberlite Cucumbi 79 (Roblez-Cruz et al., 2012b), which is also Cretaceous and in the catchment area of the Congo alluvial diamond population. Single P-T point yielded by traditional thermobarometry for diamond 11712 exceeds the temperature estimates based on the nitrogen aggregation thermometer for the sample, 1150–1185 °C (Figure 9 and Figure 10). This temperature mismatch follows the general pattern of the lower mantle residence temperatures compared to traditional thermobarometry temperatures for Kasai (Figure 10) and for included diamonds globally. This can be ascribed to the higher temperatures of freezing-in of the mineral equilibrium or to several other explanations. For example, the growth of diamonds is accompanied by transient heating events whose thermal signature is averaged out in time integrated [N] thermometry, but preserved in mineral chemistry (Aulbach et al., 2011). In addition, the thermobarometry of diamond inclusions overestimates temperatures as inclusion grains do not touch (Stachel and Harris, 2008, and references therein).

The minimum temperatures of the diamond residence as constrained by the N aggregation places the lower bound on the thermal state of the Congo craton. At this temperature of 1000 °C the 41 mW/m² geotherm enters the diamond stability field. This lower bound is predicated on the premise that the [N] data are representative of the general diamond population and there were no depth gaps in the kimberlite sampling. The highest heat flow is constrained by the garnet-clinopyroxene thermobarometry and is 45 mW/m². The heat flow of 41–45 mW/m² is hotter than 37 mW/m² – 42 mW/m² recorded by diamond inclusions for Archean cratonic interiors worldwide (Stachel and Harris, 2008), but compare very well with thermobarometry for mantle xenoliths and macrocrysts in kimberlites of the Congo craton. Univariant PT lines for eclogites from the Catoca and Cat-115 pipes of NE Angola (Nikitina et al., 2014) enter the diamond stability field at 1000 – 1260 °C (dashed lines on Figure 10). Garnet lherzolites and phlogopite garnet wehrlites of the Catoca, Tchiuzo, Cucumbi-79, and Alto Cuila-63 kimberlites plot at 820–1250 °C and 36–58 kb if the thermobarometer of Nimis and Taylor (2000) is employed. These values constrain the geotherm to between 40 and 45 mW/m².

The Kasai diamonds display complex CL characteristics, suggesting multiple growth events possibly under different geotherms (Figure 9). Despite this, the minimum and maximum mantle residence temperatures provide reasonable estimates of mantle residence temperature. The minimum mantle residence temperature is estimated generously low (1000 °C) due to a single sample with 0% [N]_B, since an anomalous absence of B-centers precludes an estimate. A temperature of 1000 °C is within the lower 10 % of worldwide diamond formation temperatures constrained by coexisting mineral geothermobarometry (Stachel and Harris, 2008). The upper [N] aggregation temperature estimate of 1278 °C will, if anything, be a minimum upper bound, since diamond rim growth will almost always have less aggregated N than diamond cores (e.g., Smart et al., 2011). The good agreement between [N] aggregation temperature, coexisting mineral inclusion pair temperature of this study, and that of prior studies (Roblez-Cruz et al., 2012; Nikitina et al., 2014) suggest that [N] aggregation temperatures determined from bulk [N] analysis are

sufficient even considering observed growth zones in CL.

Regional tectonothermal processes may alternately favor or hinder diamond stability within the SCLM based on their aptitude to preserve or destroy cratonic roots, respectively. Helmstaedt and Gurney (1994) and Helmstaedt and Gurney (1995) first categorized mantle events as being either diamond “friendly” or “unfriendly”, wherein the former include lateral dike swarms or “thin-skinned” deformation, and the latter include plumes, rifts, and crustal reworking. Broadly, diamond unfriendly processes act by either mechanically eroding away cratonic roots or by heating roots to higher temperatures that are unfavorable for diamond preservation at relatively low pressures.

Several tectonothermal events of the Kasai block may serve to explain the high calculated geotherms. Firstly, the higher heat flow may relate to reworking of Archean crust in Paleoproterozoic, Mesoproterozoic, and Neoproterozoic events as indicated by zircon ages (Batumike et al., 2009b). In particular, Neoproterozoic ages for zircon correspond well to ages for magmatic activity and formation of the Katangan Basin (880 Ma – 760 Ma), the peak of the Lufilian orogeny (570 Ma), and the closure of the Katangan Basin (540 Ma) that introduced additional oceanic lithosphere beneath the Kasai block (John et al., 2004), all on the south and south-east margins of the Kasai block. These events may relate to the position of the craton above a superplume (Torsvik et al., 2010).

Alternatively, the high geotherms may be directly attributable to rifting of the southern Atlantic. Contemporaneous eruption of kimberlites on the Sao Francisco craton (Chaves et al., 2008), in South Africa (Jelsma et al., 2009), and Catoca (Roblez-Cruz et al., 2012a) each along northeast-southwest trending lineaments, are consistent with the timing of southern Atlantic rifting. It is well known that rifting may increase the heat flow in adjacent cratonic SCLM. Miller et al. (2012) report heating and destruction of the Southern Superior SCLM attributable to the thermal disturbance of the Midcontinent Rift at 1.1 Ga, with a remaining elevated geotherm (from 39 – 41 mW/m² pre-rift to 41 – 42 mW/m² in the Jurassic). Similarly, Smit et al. (2014) report a geotherm of 42 mW/m² constrained from 1.1 Ga diamond inclusions near the Midcontinent Rift, versus a 39 mW/m² from Jurassic kimberlites. South African SCLM xenoliths record a regional protracted heating event (~100 °C, about +2 mW/m²) associated with Gondwana supercontinent breakup starting at ~200 Ma propagating from east to west (Bell et al., 2003).

Present day heat flow value measurements of Southern DRC with which to compare our determined paleogeotherms are available, though scarce. Sebagenzi et al. (1993) report the single existing heat flow measurement from a borehole at Mbuji-Mayi to be 44 mW/m², with much higher geotherms in the Kibara belt (53.0 ± 30 mW/m² to 69.0 ± 26 mW/m² across three boreholes). A more recent heat flow estimate of 40 ± 5 mW/m² based on data from the Gilson 1 and M’bandaka oil wells by Lucazeau et al. (2015) is in good agreement with the measurement of Sebagenzi et al. (1993).

The constrained thermal regime and the restriction of diamonds to the lithosphere (Stachel and Harris,

2008) enable assessment of the lithosphere thickness. The 41 mW/m² model geotherm intersects the maximum N aggregation temperatures at 63 kb (189 km). If the higher geotherm of 44 mW/m² is assumed, the greatest depth where the diamonds occur in the Congo mantle is 58 kb (175 km) (Figure 10). The relatively thin lithosphere of 175 – 189 km is shallower than the typical cratonic lithosphere of ~200 km as defined petrologically (e.g. Boyd, 1987; Kopylova et al., 1999; Eaton et al., 2009 and references therein) and even more so for the geophysical lithosphere (e.g. Begg et al., 2009; Dalton et al., 2009, and references therein; Fischer et al., 2010 and references therein). Specifically, Hansen et al. (2009) report an LAB potentially as deep as 285 km beneath the Bogoin, Central African Republic permanent seismic station (BCGA), though they cast doubt on this estimate. Global seismic tomography models indicate high velocity domains underlying the Congo craton, suggesting lithospheric roots as deep as 300-400 km (Begg et al., 2009; O'Reilly et al., 2009).

The thinner lithosphere beneath the marginal Kasai block may be attributable to its position on the periphery of the Congo craton. The geophysical lithosphere on the marginal part of the Congo craton is thinner than the lithosphere in the center of the craton (Begg et al., 2009). An additional factor in the relatively shallow petrological LAB could be ingress of asthenospheric melts like those below the Lucapa corridor. (O'Neill et al., 2005).

6.4 Dual Paragenesis Origin of Diamonds

None of the 23 peridotitic diamonds bear clinopyroxene or garnet and therefore may not be unambiguously assigned to lherzolitic or harzburgitic parageneses. Nevertheless, high Mg# of olivine inclusions in the suite (Figure 3) and absence of peridotitic garnet and clinopyroxene suggest extremely depleted peridotitic mantle, likely harzburgitic. Analyzed clinopyroxenes are low in Mg# and bear a significant jadeite component, classifying them as eclogitic. Na₂O and K₂O concentration in garnet and clinopyroxene, respectively, are elevated. Na₂O in garnet inclusions ranges from 0.21 to 0.48 wt.%, average 0.30 wt.%, whereas K₂O in clinopyroxene ranges from 0 to 0.58 wt.%, average 0.27 wt.%. Elevations of these trace elements in the respective phases are indicative of high pressure origin; higher concentrations are known in diamondiferous eclogites, and still higher enrichment in eclogitic diamond mineral inclusions (McCandless and Gurney, 1989; Gurney and Zweistra, 1995). On the basis of diamond inclusion parageneses, 70% of the suite is peridotitic (n = 23), 18% eclogitic (n = 6), and 12% contain only sulfides (n = 4). Coincidentally, inclusion-bearing diamonds from this suite occur in nearly the 3:1 ratio of peridotite to eclogite diamonds suggested by Hawthorne et al. (1978) for southern Africa. Carbon isotopic data supports these assignments of paragenesis (see discussion section 6.1), wherein 12.5% of the octahedrally grown samples can be unambiguously assigned to eclogitic parageneses ($\delta^{13}\text{C} < -13\text{‰}$, n = 4).

Prior studies of DRC and Angolan diamond inclusions and xenoliths have also revealed the presence of two parageneses comprising Congo craton SCLM. Boyd and Danchin (1980) report results from lherzolites obtained from the Somacuanza kimberlite of central Angola as well as eclogites from kimberlites of both central and northeastern Angola. Five inclusion-bearing diamonds from the DRC studied by Prinz et

al. (1975) contained exclusively eclogitic parageneses. Mveumba Ntanda et al. (1982) reported olivine, lherzolitic garnet, and eclogitic garnet within diamonds sourced from the Mbuji Mayi area. Kampata et al. (1995) report xenoliths of lherzolites and harzburgites with less abundant eclogites within the diamond-poor Kundelungu kimberlites of southeastern DRC. More recent studies focusing on mantle sampled by diamond producing kimberlites of northeastern Angola has also revealed multiple parageneses, including eclogite, garnet lherzolite, and wehrlite (Robles-Cruz et al., 2012b). Nikitina et al. (2014) report a predominance of eclogitic xenoliths over peridotitic xenoliths in the Catoca kimberlite pipe. However, the extent to which a sample suite of either diamond inclusions or mantle xenoliths reflects the true abundance of SCLM parageneses is not straightforward. The efficiency of production of free CO₂ from the interaction of proto-kimberlitic fluid with diamond host rocks, and consequently the efficacy of fracturing and sampling by kimberlite, may favour eclogite over peridotite (Smith et al., 2015). During the transport to the surface peridotitic xenoliths are more likely to be disaggregated than their eclogitic counterparts (Gurney et al., 2005, and references therein). All this leads to observations that eclogites may comprise 20 – 30% of xenoliths or diamonds in particular suites, with the commonly-cited exceptional 80% eclogitic xenoliths at Roberts Victor, South Africa (MacGregor and Carter, 1970), even though eclogites make up less than 2% of the mantle (Schulze, 1989; Russell et al., 2001; McLean et al., 2007).

The origin of eclogites in the Congo mantle was proven to be subduction-related, based on petrography, major and trace element investigations, and Proterozoic U-Pb ages of the eclogite xenoliths contemporaneous with the subduction around the Congo craton (Nikitina et al., 2014). The origin of eclogitic parageneses within the suite is likely attributable to cratonic amalgamation on the southern margin of the Congo craton in Proterozoic time (Nikitina et al., 2014). Peridotites of the Congo craton have never been studied in detail, but in general peridotitic SCLM is the residuum of extreme degrees of low pressure polybaric partial melting, possibly the Archean equivalent of modern day oceanic spreading centers (Pearson and Wittig, 2008) imbricated in Archean time (Helmstaedt and Schulze, 1989). Kimberlites sampling cratonic margins contain significant proportions of eclogitic parageneses attributable to post-Archean subduction events (Jacob, 2004). Diamond formation in the Kasai eclogites documented by this study is favoured by the setting of the Lucapa kimberlites off the thickest part of the Congo craton root (Begg et al., 2009).

Before the opening of the Southern Atlantic in Mesozoic time (Nürnberg and Müller, 1991), the Congo and the Sao Francisco cratons (modern day Brazil) were a single continent (Gondwana) with a coherent, continuous mantle. Similar to the Congo craton, Brazil hosts Late Cretaceous alkaline magmatism, including kimberlites and carbonatites (Schimmel et al., 2003, and references therein). Therefore, one might expect similar mantle composition, thermal state and diamond-forming processes below the Congo and the Sao Francisco cratons. Mantle processes that culminated in the break-up of Gondwana should be equally pronounced below the Congo and the Sao Francisco cratons. The Tristan mantle plume that was suggested to exist below the Cretaceous Congo craton is estimated to be 1500 km in diameter (O’Con-

nor et al., 1990; Gibson et al., 1999) therefore should have been expressed across significant parts of the Congo and the Sao Francisco cratons. Indeed, both the Sao Francisco craton and the Congo craton host peridotitic and eclogitic diamonds (Hayman et al., 2005), but the inferred mantle processes below these two cratons are dissimilar.

The Sao Francisco craton hosts a sizable population of diamonds from the lower mantle. Kaminsky et al. (2001), Hayman et al. (2005), Bulanova et al. (2010), Walter et al., (2011), and Pearson et al. (2014) documented the presence of lower mantle, transition zone minerals, and/or majoritic garnet as inclusions in diamonds of the Juina province of the Sao Francisco craton, which serve as direct evidence of plume impingement. Despite the association of alkaline magmatism in the Congo craton with the paleolocation of a mantle plume (e.g. Torsvik et al., 2010), no inclusions of lower mantle and transition zone minerals are present within the suite. The absence of Type II (nitrogen free) diamonds similarly confirms that no diamonds of the suite are derived from the lower mantle (Smith and Kopylova, 2014).

The presence of lower mantle parageneses in Brazilian diamonds and their absence in kimberlites of NE Angola may relate to several factors. Firstly, it may be a function of the proximity to the Tristan plume head during the time of Southern Atlantic rifting. O'Connor et al. (1990) and Gibson et al. (1999) infer the Tristan da Cunha plume to have been underneath southeastern Brazil at the time of onset of continental breakup based on the location of Parana-Etendeka continental flood basalts (CFB; O'Connor et al., 1990; Gibson et al., 1999; Hawkesworth et al., 1999; Figure 11). Alternatively, the Trindade plume (presently off the coast of southeastern Brazil), rather than the Tristan plume, could be responsible for the transport of sublithospheric diamonds to the populations of western Brazilian kimberlites (i.e., Juina-5). The Trindade plume is closer to the Brazilian Juina kimberlites that carry lower mantle diamonds and existed underneath Brazil in the Cretaceous, contemporaneous with Brazilian alkaline magmatism than the Tristan da Cunha plume whose arrival caused the breakup of Gondwana (Figure 11). Alkaline magmatism in Brazil spans 95 – 55 Ma (Heaman et al., 1998; Thomson et al., 1998), coeval with the younger Trindade plume. The Brazilian alkaline magmatism eruption ages broadly young from northwest to southeast following the migration of the present-day Trindade plume (Thompson et al., 1998). Angolan kimberlite genesis on the other hand cannot be attributed directly to plume activity. The younging direction of carbonatite/kimberlites of the Lucapa graben is northeast, to the opposite of the younging of basaltic volcanism southwest along the Walvis Ridge towards the Tristan da Cunha hot spot (O'Connor et al., 1990).

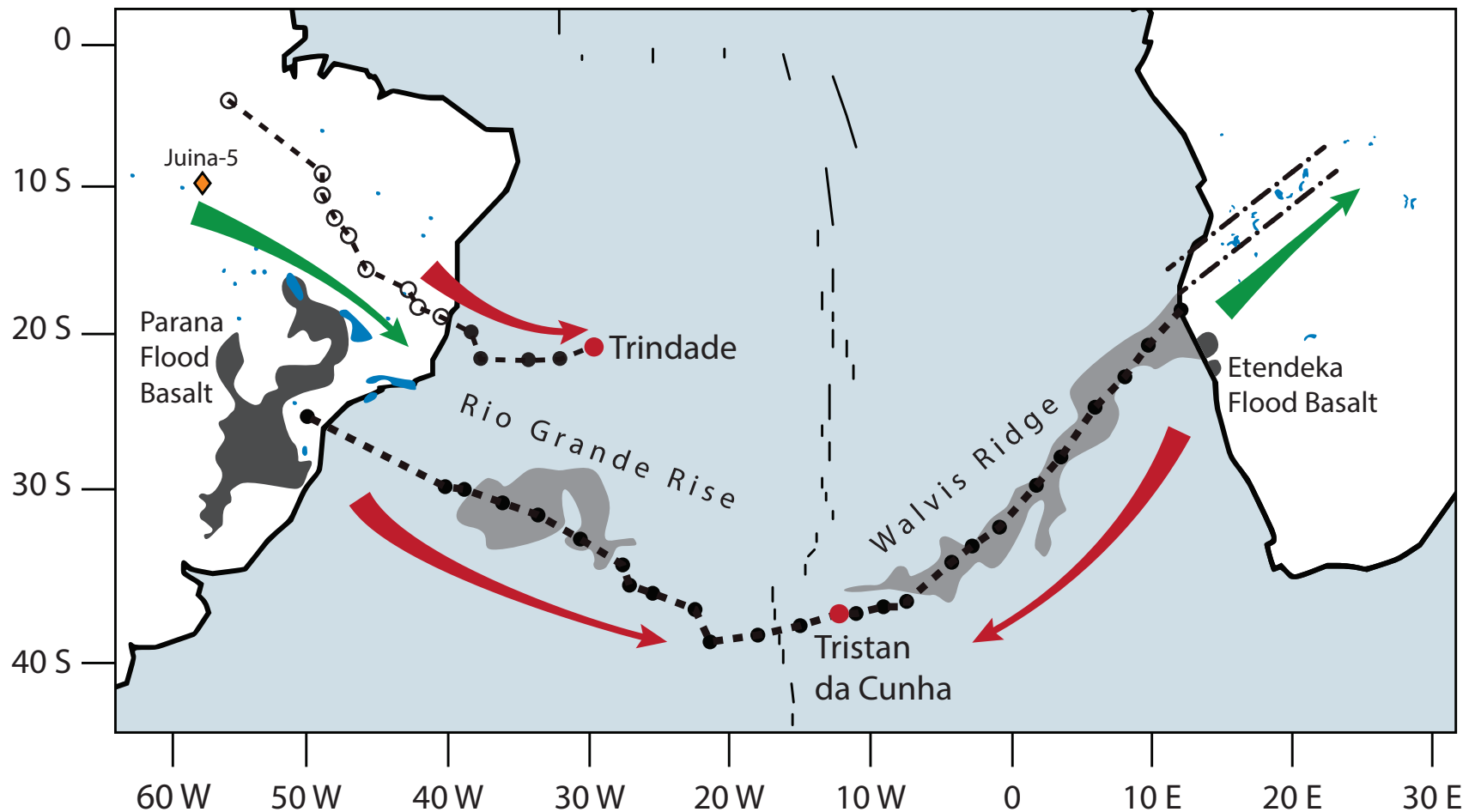


Figure 11. The modern day southern Atlantic Ocean with selected hotspot tracks, alkaline magmatic provinces, and continental flood basalts (CFBs). Large red circles indicate the present day location of the Trindade and Tristan da Cunha plumes. Dotted black lines indicate the hypothesized hotspot paths of the Trindade plume and Tristan plume after O'Connor et al. (1990). Open circles within the hotspot track indicate they are loosely constrained. Light grey areas indicate the Walvis Ridge and Rio Grande Rise. Red arrows indicate direction of younging of hotspot tracks. The Tristan da Cunha plume trace appears on both sides of the mid-ocean ridge, indicating paleo-plume magmatism at the mid-ocean ridge location. Dark grey areas indicate CFBs, emplaced together at 132 Mya (age of peak magmatism, Stewart et al., 1996). Blue areas indicate the locations of central African and Brazilian alkaline magmas (alkaline basalt, carbonatite, and kimberlite, after sources in Figure 1, O'Connor et al. (1990) and Crough et al. (1980); South African alkaline magmatism omitted for simplicity). Green arrows indicate the general younging direction of alkaline magmatism. Whereas South American alkaline magmatism youngs in the same direction as both the Trindade and western expression of the Tristan da Cunha plume, central African alkaline magmatism youngs oppositely.

7. Conclusions

Diamonds emplaced by kimberlites of the northeast Lucapa graben and eroded to form alluvial deserts along the Kasai river contain 25 – 2900 ppm [N], show 0 – 88% [N]_B aggregation and $\delta^{13}\text{C}$ isotopic compositions spanning -27‰ to -2‰ with a mode near mantle-like values. *In situ* carbon isotopic and [N] investigations reveal that many Kasai diamonds have experienced episodic growth from isotopically heterogeneous sources. Select diamonds' isotopic signatures dictate that carbon from both subducted organic material and mantle carbon were required in the diamond forming fluids. Large heterogeneities in diamond [N] similarly suggest episodic growth. [N] aggregation and content varies across the suite, suggesting diamonds experienced markedly different residence histories.

The studied Kasai diamonds contain inclusions of olivine, orthopyroxene, and garnet. Their chemistry indicates that the diamonds originate from garnet-facies harzburgitic (70%) and eclogitic (18%) sources. Clinopyroxene-garnet thermobarometry suggest diamond formation at 1350 – 1375 °C, whereas [N] aggregation thermometry yields diamond residence temperatures between 1000 and 1275 °C, if the assumed residence time is 0.9 – 3.3 Ga. The integrated geothermobarometry indicates heat fluxes of 41 – 45 mW/m², in the Cretaceous, slightly higher than the typical cratonic heat flows. I explain these elevated heat flows by contemporaneous development of adjacent rifting, thermal disturbance by plume and multiple post-Archean reactivations of the craton. Compositions of fluid inclusion in fibrous diamonds are moderately to highly silicic, similar to fluid compositions in DRC diamonds, suggesting spatially extensive homogenization of the diamond-forming fluid within the Congo mantle over tens of millions of years.

References

- Alberti, A., Castorina, F., Censi, P., Comin-Chiaramonti, P., & Gomes, C.B. (1999). Geochemical characteristics of Cretaceous carbonatites from Angola. *Journal of African Earth Sciences*, 29(4), 735–759.
- Aulbach, S., Stachel, T., Heaman, L. M., & Carlson, J. A. (2011). Microxenoliths from the Slave craton: Archives of diamond formation along fluid conduits. *Lithos*, 126(3), 419–434.
- Batumike, J. M., Griffin, W. L., Belousova, E. A., Pearson, N. J., O'Reilly, S. Y., & Shee, S. R. (2008). LAM-ICPMS U–Pb dating of kimberlitic perovskite: Eocene–Oligocene kimberlites from the Kundelungu Plateau, DR Congo. *Earth and Planetary Science Letters*, 267(3), 609–619.
- Batumike, J. M., Griffin, W. L., & O'Reilly, S. Y. (2009a). Lithospheric mantle structure and the diamond potential of kimberlites in southern DR Congo. *Lithos*, 112, 166–176.
- Batumike, J. M., Griffin, W. L., O'Reilly, S. Y., Belousova, E. A., & Pawlitschek, M. (2009b). Crustal evolution in the central Congo-Kasai Craton, Luebo, DR Congo: Insights from zircon U–Pb ages, Hf-isotope and trace-element data. *Precambrian Research*, 170(1), 107–115.
- Begg, G. C., Griffin, W. L., Natapov, L. M., O'Reilly, S. Y., Grand, S. P., O'Neill, C. J., Hronsky, J.M.A., Poudjom Djomani, Y., Swain, C.J., Deen, T., and Bowden, P. (2009). The lithospheric architecture of Africa: seismic tomography, mantle petrology, and tectonic evolution. *Geosphere*, 5(1), 23–50.
- Bell, D. R., Schmitz, M. D., & Janney, P. E. (2003). Mesozoic thermal evolution of the southern African mantle lithosphere. *Lithos*, 71(2), 273–287.
- Beyer, C., Frost, D. J., & Miyajima, N. (2015). Experimental calibration of a garnet–clinopyroxene geobarometer for mantle eclogites. *Contributions to Mineralogy and Petrology*, 169(2), 1–21.
- Boyd, F.R. (1987). High- and low-temperature garnet peridotite xenoliths and their possible relation to the lithosphere-asthenosphere boundary beneath southern Africa. In: Nixon, P.H. (Ed.), *Mantle Xenoliths* (pp. 403–412). New York: Wiley.
- Boyd, F. R., & Gurney, J. J. (1986). Diamonds and the African lithosphere. *Science*, 232(4749), 472–477.
- Boyd, F. R., Pokhilenko, N. P., Pearson, D. G., Mertzman, S. A., Sobolev, N. V., & Finger, L. W. (1997). Composition of the Siberian cratonic mantle: evidence from Udachnaya peridotite xenoliths. *Contributions to Mineralogy and Petrology*, 128(2–3), 228–246.
- Boyd, F. R., & Danchin, R. V. (1980). Lherzolites, eclogites and megacrysts from some kimberlites of Angola. *American Journal of Science*, 280(2), 528–549.
- Boyd, S. R., Kiflawi, I., & Woods, G. S. (1994). The relationship between infrared absorption and the A defect concentration in diamond. *Philosophical Magazine B*, 69(6), 1149–1153.
- Boyd, S. R., Kiflawi, I., & Woods, G. S. (1995). Infrared absorption by the B nitrogen aggregate in diamond. *Philosophical Magazine B*, 72(3), 351–361.
- Boyd, S. R., Pillinger, C. T., Milledge, H. J., Mendelsohn, M. J., & Seal, M. (1992). C and N isotopic composition and the infrared absorption spectra of coated diamonds: evidence for the regional uniformity of CO₂-H₂O rich fluids in lithospheric mantle. *Earth and Planetary Science Letters*, 109(3), 633–644.
- Bulanova, G. P., Walter, M. J., Smith, C. B., Kohn, S. C., Armstrong, L.S., Blundy, J., and Gobbo, L. (2010) Mineral inclusions in sublithospheric diamonds from Collier 4 kimberlite pipe, Juina, Brazil: Subducted protoliths, carbonat-

- ed melts and primary kimberlite magmatism. *Contributions to Mineralogy and Petrology*, 160(4), 489–510.
- Campany, M., Mangas, J., Melgarejo, J. C., Bambi, A., Alfonso, P., Gernon, T., & Manuel, J. (2014). The Catanda extrusive carbonatites (Kwanza Sul, Angola): An example of explosive carbonatitic volcanism. *Bulletin of Volcanology*, 76(4), 1–15.
- Cartigny, P. (2005). Stable isotopes and the origin of diamond. *Elements*, 1(2), 79–84.
- Cartigny, P., Harris, J. W., & Javoy, M. (2001). Diamond genesis, mantle fractionations and mantle nitrogen content: a study of $\delta^{13}\text{C}$ –N concentrations in diamonds. *Earth and Planetary Science Letters*, 185(1), 85–98.
- Cawthorn, R. G., & Collerson, K.D. (1974). the recalculation of pyroxene end-member parameters and the estimation of ferrous and ferric iron content from electron microprobe analyses. *American Mineralogist*, 59, 1203–1208.
- Chacko, T., Mayeda, T. K., Clayton, R. N., & Goldsmith, J. R. (1991). Oxygen and carbon isotope fractionations between CO_2 and calcite. *Geochimica et Cosmochimica Acta*, 55(10), 2867–2882.
- Chambel, L., Caetano, L., & Reis, M. (2013). One century of Angolan diamonds. Retrieved from <https://xmb1.files.wordpress.com/2013/10/one-century-of-angolan-diamonds-hd2.pdf> on December 10th, 2015.
- Chaves, M.L.S.C., Benitez, L., Brandão, P.R.G., Girodo, A.C. (2008). Kimberlito Canastra-1 (São Roque de Minas, MG): geologia, mineralogia e reservas diamantíferas. *Revista Escola de Minas*, 61(3), 57–364.
- Creaser, R. A., Grütter, H., Carlson, J., & Crawford, B. (2004). Macrocystal phlogopite Rb–Sr dates for the Ekati property kimberlites, Slave Province, Canada: evidence for multiple intrusive episodes in the Paleocene and Eocene. *Lithos*, 76(1), 399–414.
- Crough, S. T., Morgan, W. J., & Hargraves, R. B. (1980). Kimberlites: their relation to mantle hotspots. *Earth and Planetary Science Letters*, 50(1), 260–274.
- Currie, C. A. & Beaumont, C. (2011). Are diamond-bearing Cretaceous kimberlites related to low-angle subduction beneath western North America? *Earth and Planetary Science Letters*, 303(1), 59–70.
- Dalton, C. A., Ekström, G., & Dziewonski, A. M. (2009). Global seismological shear velocity and attenuation: A comparison with experimental observations. *Earth and Planetary Science Letters*, 284(1), 65–75.
- Davies, R.M., Griffin, W.L., Pearson, N.J., Andrew, A.S., Doyle, B.J. and O'Reilly, S.Y., (1999). Diamonds from the deep: pipe DO-27, Slave Craton, Canada. In: J.J. Gurney, J.L. Gurney, M.D. Pascoe and S.H. Richardson (Eds.), *The J.B. Dawson Volume, Proceedings of the VIIth International Kimberlite Conference* (pp. 148–155). Cape Town: Red Roof Design.
- de Boorder, H. (1982). Deep-reaching fracture zones in the crystalline basement surrounding the West Congo System and their control of mineralization in Angola and Gabon. *Geoscientific Exploration*, 20(3), 259–273.
- de Stefano, A., Kopylova, M. G., Cartigny, P., & Afanasiev, V. (2009). Diamonds and eclogites of the Jericho kimberlite (Northern Canada). *Contributions to Mineralogy and Petrology*, 158(3), 295–315.
- de Waele, B., Johnson, S. P., & Pisarevsky, S. A. (2008). Palaeoproterozoic to Neoproterozoic growth and evolution of the eastern Congo Craton: its role in the Rodinia puzzle. *Precambrian Research*, 160(1), 127–141.
- de Wit, M. C., & Jelsma, H. A. (2015). A Review of the Kimberlites of the Democratic Republic of Congo. In: M. F. de Wit, Gaulliocheau, and M.C.J. de Wit (Eds.), *Geology and Resource Potential of the Congo Basin* (pp. 361–369). Berlin: Springer-Verlag.

- Deines, P. (1980). The carbon isotopic composition of diamonds: relationship to diamond shape, color, occurrence and vapor composition. *Geochimica et Cosmochimica Acta*, 44(7), 943-961.
- Demaiffe, D., Fieremans, M., & Fieremans, C. (1991). The kimberlites of Central Africa: a review. In: Kampunzu, A.B., Lubala R.T. (Editors), *Magmatism in Extensional Structural Settings*. Springer-Verlag, Berlin, pp. 537-539.
- Dietrich, C. (2000). Inventory of formal diamond mining in Angola. *Angola's War Economy: The Role of Oil and Diamonds*, 151.
- Eaton, D. W., Darbyshire, F., Evans, R. L., Grütter, H., Jones, A. G., & Yuan, X. (2009). The elusive lithosphere-asthenosphere boundary (LAB) beneath cratons. *Lithos*, 109(1), 1-22.
- Egorov, K. N., Roman'ko, E. F., Podvysotsky, V. T., Sablukov, S. M., Garanin, V. K., & D'yakonov, D. B. (2007). New data on kimberlite magmatism in southwestern Angola. *Russian Geology and Geophysics*, 48(4), 323-336.
- El Fadili, S., & Demaiffe, D. (1999). Petrology of eclogite and granulite nodules from the Mbuji Mayi kimberlites (Kasai, Congo): the significance of kyanite-omphacite intergrowths. In: J.J. Gurney, J.L. Gurney, M.D. Pascoe and S.H. Richardson (Eds.), *The J.B. Dawson Volume, Proceedings of the VIIth International Kimberlite Conference* (pp. 205-213). Cape Town: Red Roof Design.
- Faure, S., Godey, S., Fallara, F., & Trépanier, S. (2011). Seismic architecture of the Archean North American mantle and its relationship to diamondiferous kimberlite fields. *Economic Geology*, 106(2), 223-240.
- Fernandez-Alonso, M., Cutten, H., De Waele, B., Tack, L., Tahon, A., Baudet, D., & Barritt, S. D. (2012). The Mesoproterozoic Karagwe-Ankole Belt (formerly the NE Kibara Belt): The result of prolonged extensional intracratonic basin development punctuated by two short-lived far-field compressional events. *Precambrian Research*, 216, 63-86.
- Fitzsimons, I. C. W., Harte, B., Chinn, I. L., Gurney, J. J., & Taylor, W. R. (1999). Extreme chemical variation in complex diamonds from George Creek, Colorado: A SIMS study of carbon isotope composition and nitrogen abundance. *Mineralogical Magazine*, 63(6), 857-857.
- Gibson, S. A., Thompson, R. N., Leonardos, O. H., Dickin, A. P., & Mitchell, J. G. (1999). The sectorized extent of plume-lithosphere interactions during continental flood-basalt genesis: geochemical evidence from Cretaceous magmatism in southern Brazil. *Contributions to Mineralogy and Petrology*, 137(1-2), 147-169.
- Griffin, W. L., Sobolev, N.V., Ryan, C.G., Pokhilenko, N.P., Win, T.T. and Yefimova, E.S. (1993). Trace elements in garnets and chromites: diamond formation in the Siberian lithosphere. *Lithos*, 29(3-4), 235-256.
- Griffin, W. L., O'Reilly, S. Y., Abe, N., Aulbach, S., Davies, R. M., Pearson, N. J., Doyle, B. J., & Kivi, K. (2003). The origin and evolution of the Archean lithospheric mantle. *Precambrian Research* 127, 19-41.
- Grütter, H. S., Gurney, J. J., Menzies, A. H., & Winter, F. (2004). An updated classification scheme for mantle-derived garnet, for use by diamond explorers. *Lithos*, 77(1), 841-857.
- Gurney, J. J., Helmstaedt, H. H., Le Roex, A. P., Nowicki, T. E., Richardson, S. H., & Westerlund, K. J. (2005). Diamonds: crustal distribution and formation processes in time and space and an integrated deposit model. *Economic Geology*, 100, 143-177.
- Gurney, J. J., & Zweistra, P. (1995). The interpretation of the major element compositions of mantle minerals in diamond exploration. *Journal of Geochemical Exploration*, 53(1), 293-309.
- Hansen, S. E., Nyblade, A. A., & Julia, J. (2009). Estimates of crustal and lithospheric thickness in sub-saharan Africa from S-wave receiver functions. *South African Journal of Geology*, 112(3-4), 229-240.

- Harte, B., Fitzsimons, I. C. W., Harris, J. W., & Otter, M. L. (1999). Carbon isotope ratios and nitrogen abundances in relation to cathodoluminescence characteristics for some diamonds from the Kaapvaal Province, S. Africa. *Mineralogical Magazine*, 63(6), 829–829.
- Harte, B., & Otter, M. (1992). Carbon isotope measurements on diamonds. *Chemical Geology: Isotope Geoscience section*, 101(1), 177–183.
- Hawthorne, J. B., Gurney, J. J., & Harris, J. W. (1978). Inclusions in diamonds from South Africa. *International Mineralogical Association, Eleventh General Meeting, September 1978, Novosibirsk, USSR, abstracts*.
- Hawkesworth, C., Kelley, S., Turner, S., Le Roex, A., & Storey, B. (1999). Mantle processes during Gondwana break-up and dispersal. *Journal of African Earth Sciences*, 28(1), 239–261.
- Hayman, P. C., Kopylova, M. G., & Kaminsky, F. V. (2005). Lower mantle diamonds from Rio Soriso (Juina area, Mato Grosso, Brazil). *Contributions to Mineralogy and Petrology*, 149(4), 430–445.
- Heaman, L., Teixeira, N., Gobbo, L., & Gaspar, J. (1998). U-Pb mantle zircon ages for kimberlites from the Juina and Paranatinga provinces, Brazil. In: VIIth International Kimberlite Conference, Extended abstracts (pp 322–324). Cape Town.
- Helmstaedt, H. H., & Gurney, J. J. (1994). Geotectonic controls on the formation of diamonds and their kimberlitic and lamproitic host rocks: Applications to diamond exploration. In: H.O.A. Meyer and O.H. Leonardos (Eds.), *Diamonds: Characterization, Genesis and Exploration*. CPRM Special Publication 1/B, 236–250.
- Helmstaedt, H. H., & Gurney, J. J. (1995). Geotectonic controls of primary diamond deposits: implications for area selection. *Journal of Geochemical Exploration*, 53(1), 125–144.
- Helmstaedt, H. H., & Schulze, D. J. (1989). Southern African kimberlites and their mantle sample: implications for the Archean tectonics and lithosphere evolution In: *Proceedings of the Fourth International Kimberlite Conference, Perth, Special Publication (Vol. 14, pp. 358–368)*. Geological Society of Australia.
- Izraeli, E. S., Harris, J. W., & Navon, O. (2004). Fluid and mineral inclusions in cloudy diamonds from Koffiefontein, South Africa. *Geochimica et Cosmochimica Acta*, 68(11), 2561–2575.
- Jacob, D. E. (2004). Nature and origin of eclogite xenoliths from kimberlites. *Lithos*, 77(1), 295–316.
- Javoy, M., Pineau, F., & Delorme, H. (1986). Carbon and nitrogen isotopes in the mantle. *Chemical geology*, 57(1), 41–62.
- Javoy, M., Pineau, F., & Demaiffe, D. (1984). Nitrogen and carbon isotopic composition in the diamonds of Mbuji Mayi (Zaire). *Earth and Planetary Science Letters*, 68(3), 399–412.
- Jelsma, H., Barnett, W., Richards, S., & Lister, G. (2009). Tectonic setting of kimberlites. *Lithos*, 112, 155–165.
- Jelsma, H. A., de Wit, M. J., Thiart, C., Dirks, P. H., Viola, G., Basson, I. J., & Anckar, E. (2004). Preferential distribution along transcontinental corridors of kimberlites and related rocks of Southern Africa. *South African Journal of Geology*, 107(1–2), 301–324.
- Jelsma, H., Krishnan, U., Perritt, S., Preston, R., Winter, F., Lemotlo, L., van der Linde, G., Armstrong, R., Phillips, D., Joy, S. and Costa, J. (2013). Kimberlites from Central Angola: a case study of exploration findings. In: *Proceedings of 10th International Kimberlite Conference (pp. 173-190)*. Springer India.
- John, T., Schenk, V., Mezger, K., & Fembo, F. (2004). Timing and PT evolution of whiteschist metamorphism in the Lufilian Arc-Zambezi belt Orogen (Zambia): implications for the assembly of Gondwana. *The Journal of Geology*

- Johnson, S.P., De Waele, B., Evans, D., Banda, W., Tembo, F., Milton, J.A., & Tani, K. (2007). Geochronology of the Zambezi supracrustal sequence, southern Zambia: a record of Neoproterozoic divergent process along the southern margin of the Congo Craton. *The Journal of Geology* 115 (3), 355–374.
- Kaminsky, F., Zakharchenko, O., Davies, R., Griffin, W., Khachatryan-Blinova, G., & Shiryaev, A. (2001). Super-deep diamonds from the Juina area, Mato Grosso State, Brazil. *Contributions to Mineralogy and Petrology*, 140(6), 734–753.
- Kampata, M. D., Moreau, J., Hertogen, J., Demaiffe, D., Condliffe, E., & Mvuemba, N. F. (1995). Megacrysts and ultramafic xenoliths from Kundelungu kimberlites (Shaba, Zaire). *Mineralogical Magazine*, 59(397), 661–676.
- Kennedy, C.S. and Kennedy, G.C. (1976). The equilibrium boundary between graphite and diamond. *Journal of Geophysical Research*, 81, 2467–2470.
- Klein-BenDavid, O., Izraeli, E. S., Hauri, E., & Navon, O. (2007). Fluid inclusions in diamonds from the Diavik mine, Canada and the evolution of diamond-forming fluids. *Geochimica et Cosmochimica Acta*, 71(3), 723–744.
- Klein-BenDavid, O., Logvinova, A. M., Schrauder, M., Spetius, Z. V., Weiss, Y., Hauri, E. H., Kaminsky, F.V., Sobolev, N.V., & Navon, O. (2009). High-Mg carbonatitic microinclusions in some Yakutian diamonds—a new type of diamond-forming fluid. *Lithos*, 112, 648–659.
- Klein-BenDavid, O., Pearson, D. G., Nowell, G. M., Ottley, C., McNeill, J. C., & Cartigny, P. (2010). Mixed fluid sources involved in diamond growth constrained by Sr–Nd–Pb–C–N isotopes and trace elements. *Earth and Planetary Science Letters*, 289(1), 123–133.
- Kopylova, M. G., Gurney, J.J., and Daniels, L.R.M. (1997). Mineral inclusions in diamonds from the River Ranch kimberlite, Zimbabwe. *Contributions to Mineralogy and Petrology*, 129(4), 366–384.
- Kopylova, M. G., Navon, O., Dubrovinsky, L., & Khachatryan, G. (2010). Carbonatitic mineralogy of natural diamond-forming fluids. *Earth and Planetary Science Letters*, 291(1), 126–137.
- Kopylova, M. G., Russell, J. K., & Cookenboo, H. (1999). Petrology of peridotite and pyroxenite xenoliths from the Jericho kimberlite: implications for the thermal state of the mantle beneath the Slave craton, northern Canada. *Journal of Petrology*, 40(1), 79–104.
- Krogh, E. J. (1988). The garnet–clinopyroxene Fe–Mg geothermometer—a reinterpretation of existing experimental data. *Contributions to Mineralogy and Petrology*, 99(1), 44–48.
- Leahy, K., & Taylor, W. R. (1997). The influence of the Glennie domain deep structure on the diamonds in Saskatchewan kimberlites. *Geologiya i Geofizika*, 38, 481–491.
- Linol, B., de Wit, M. J., Guillocheau, F., Robin, C., & Dautheil, O. (2015). Multiphase Phanerozoic subsidence and uplift history recorded in the Congo basin: A complex successor basin. In: M. F. de Wit, Guillocheau, and M.C.J. de Wit (Eds.), *Geology and Resource Potential of the Congo Basin* (pp. 213–227). Berlin: Springer-Verlag.
- Lucazeau, F., Armitage, J., & Kabongo, É. K. (2015). Thermal Regime and Evolution of the Congo Basin as an Intracratonic Basin. In: M. de Wit, F. Guillocheau, and M.C.J. de Wit (Eds.), *Geology and Resource Potential of the Congo Basin* (pp. 229–244). Berlin: Springer-Verlag.
- Macgregor, I. D., & Carter, J. L. (1970). The chemistry of clinopyroxenes and garnets of eclogite and peridotite xenoliths from the Roberts Victor Mine, South Africa. *Physics of the Earth and Planetary Interiors*, 3, 391–397.

- McCallum, M. E., Huntley, P. M., Falk, R. W., & Otter, M. L. (1994). Morphological, resorption and etch feature trends of diamonds from kimberlite populations within the Colorado–Wyoming state line district, USA. In: H.O.A. Meyer and O.H. Leonardos (Eds.), *Diamonds: Characterization, Genesis and Exploration*. CPRM Special Publication (1/B, pp. 78–97).
- McCandless, T.E. and Gurney, J.J., (1989). Sodium in garnet and potassium in clinopyroxene: criteria for classifying mantle eclogites. In: J. Ross (Ed.), *Kimberlites and Related Rocks Their Crustal/Mantle Setting, Diamonds and Diamond Exploration*. Geological Society of Australia Special Publication, 14/2 (pp. 827–832).
- McLean, H., Banas, A., Creighton, S., Whiteford, S., Luth, R. W., & Stachel, T. (2007). Garnet xenocrysts from the Diavik mine, NWT, Canada: Composition, color, and paragenesis. *The Canadian Mineralogist*, 45(5), 1131–1145.
- Mendelssohn, M. J., & Milledge, H. J. (1995). Geologically significant information from routine analysis of the mid-infrared spectra of diamonds. *International Geology Review*, 37(2), 95–110.
- Milledge, H. J., Mendelssohn, M. J., Seal, M., Rouse, J. E., Swart, P. K., & Pillinger, C. T. (1983). Carbon isotopic variation in spectral type II diamonds. *Nature*, 303(5920), 791–792.
- Miller, C. E., Kopylova, M. G., & Ryder, J. (2012). Vanished diamondiferous cratonic root beneath the Southern Superior province: evidence from diamond inclusions in the Wawa metaconglomerate. *Contributions to Mineralogy and Petrology*, 164(4), 697–714.
- Mveumba Ntanda, F., Moreau, J., & Meyer, H. O. A. (1982). Particularites des inclusions cristallines primaires des diamants du Kasai, Zaire. *Canadian Mineralogist*, 20, 217–230.
- Nakamura, D. (2009). A new formulation of garnet–clinopyroxene geothermometer based on accumulation and statistical analysis of a large experimental data set. *Journal of Metamorphic Geology*, 27(7), 495–508.
- Navon, O. (1999). Diamond formation in the Earth’s mantle. In: J.J. Gurney, J.L. Gurney, M.D. Pascoe and S.H. Richardson (Eds.), *The J.B. Dawson Volume, Proceedings of the VIIth International Kimberlite Conference* (pp. 584–604). Cape Town: Red Roof Design.
- Navon, O., Hutcheon, I. D., Rossman, G. R., Wasserburg, G. J. (1988) Mantle-derived fluids in diamond micro-inclusions. *Nature*, 335, 784–789.
- Nikitina, L. P., Korolev, N. M., Zinchenko, V. N., & Felix, J. T. (2014). Eclogites from the upper mantle beneath the Kasai Craton (Western Africa): Petrography, whole-rock geochemistry and U Pb zircon age. *Precambrian Research*, 249, 13–32.
- Nimis, P., & Taylor, W. R. (2000). Single clinopyroxene thermobarometry for garnet peridotites. Part I. Calibration and testing of a Cr-in-Cpx barometer and an enstatite-in-Cpx thermometer. *Contributions to Mineralogy and Petrology*, 139(5), 541–554.
- Nürnberg, D., & Müller, R. D. (1991). The tectonic evolution of the South Atlantic from Late Jurassic to present. *Tectonophysics*, 191(1), 27–53.
- O’Connor, J. M., & Duncan, R. A. (1990). Evolution of the Walvis Ridge-Rio Grande rise hot spot system: implications for African and South American plate motions over plumes.
- O’Neill, C.J., Moresi, L., Jaques, A.L., (2005). Geodynamic controls on diamond deposits: implications for Australian occurrences. *Tectonophysics* 404, 217–236.
- O’Reilly, S. Y., Zhang, M., Griffin, W. L., Begg, G., & Hronsky, J. (2009). Ultradeep continental roots and their oceanic remnants: A solution to the geochemical “mantle reservoir” problem?. *Lithos*, 112, 1043–1054.

- Otter, M. L., Gerneke, D. A., Harte, B., Gurney, J. J., Harris, J. W., & Wilding, M. C. (1991). Diamond growth histories revealed by cathodoluminescence and carbon isotope studies. In: *Proceedings of the 5th International Kimberlite Conference*, (Vol. 5, pp. 318–319).
- Palot, M., Pearson, D. G., Stern, R. A., Stachel, T., & Harris, J. W. (2014). Isotopic constraints on the nature and circulation of deep mantle C–H–O–N fluids: Carbon and nitrogen systematics within ultra-deep diamonds from Kankan (Guinea). *Geochimica et Cosmochimica Acta*, 139, 26–46.
- Pearson, D. G., Brenker, F. E., Nestola, F., McNeill, J., Nasdala, L., Hutchison, M. T., Matveev, S., Mather, K., Silversmit, G., Schmitz, S. and Vekemans, B. (2014). Hydrous mantle transition zone indicated by ringwoodite included within diamond. *Nature*, 507(7491), 221–224.
- Pearson, D. G., & Wittig, N. (2008). Formation of Archean continental lithosphere and its diamonds: the root of the problem. *Journal of the Geological Society*, 165(5), 895–914.
- Phillips, D., Harris, J. W., and Viljoen, K. S. (2004). Mineral chemistry and thermobarometry of inclusions from De Beers Pool diamonds, Kimberley, South Africa. *Lithos*, 77(1), 155–179.
- Pollack, H. N. and Chapman, D. S. (1977). On the regional variation of heat flow, geotherms, and lithospheric thickness. *Tectonophysics*, 38, 279–296.
- Prinz, M., Manson, D. V., Hlava, P. F., & Keil, K. (1975). Inclusions in diamonds: garnet lherzolite and eclogite assemblages. *Physics and Chemistry of the Earth*, 9, 797–815.
- Reis, B. (1972). Preliminary note on the distribution and tectonic control of kimberlites in Angola. In: *Proceedings of the 24th International Geological Congress, Montreal, Canada, 21 August–1 September 1972* (Volume 24, pp. 276–281).
- Richet, P., Bottinga, Y., & Janoy, M. (1977). A review of hydrogen, carbon, nitrogen, oxygen, sulphur, and chlorine stable isotope enrichment among gaseous molecules. *Annual Review of Earth and Planetary Sciences*, 5, 65–110.
- Robles-Cruz, S. E., Escayola, M., Jackson, S., Galí, S., Pervov, V., Watangua, M., Gonçalves, A., & Melgarejo, J. C. (2012a). U–Pb SHRIMP geochronology of zircon from the Catoca kimberlite, Angola: implications for diamond exploration. *Chemical Geology*, 310, 137–147.
- Robles-Cruz, S. E., Melgarejo, J. C., Galí, S., & Escayola, M. (2012b). Major-and Trace-Element Compositions of Indicator Minerals that Occur as Macro- and Megacrysts, and of Xenoliths, from Kimberlites in Northeastern Angola. *Minerals*, 2(4), 318–337.
- Russell, J. K., Dipple, G. M., & Kopylova, M. G. (2001). Heat production and heat flow in the mantle lithosphere, Slave craton, Canada. *Physics of the Earth and Planetary Interiors*, 123(1), 27–44.
- Schärer, U., Corfu, F., & Demaiffe, D. (1997). U–Pb and Lu–Hf isotopes in baddeleyite and zircon megacrysts from the Mbuji-Mayi kimberlite: constraints on the subcontinental mantle. *Chemical Geology*, 143(1), 1–16.
- Schidlowski, M. (2001). Carbon isotopes as biogeochemical recorders of life over 3.8 Ga of Earth history: evolution of a concept. *Precambrian Research*, 106(1), 117–134.
- Schimmel, M., Assumpção, M., & VanDecar, J. C. (2003). Seismic velocity anomalies beneath SE Brazil from P and S wave travel time inversions. *Journal of Geophysical Research: Solid Earth* (1978–2012), 108(B4).
- Schmidberger, S. S., Simonetti, A., Heaman, L. M., Creaser, R. A., & Whiteford, S. (2007). Lu–Hf, in-situ Sr and Pb isotope and trace element systematics for mantle eclogites from the Diavik diamond mine: Evidence for Paleoproterozoic subduction beneath the Slave craton, Canada. *Earth and Planetary Science Letters*, 254(1), 55–68.

- Schrauder, M., & Navon, O. (1994). Hydrous and carbonatitic mantle fluids in fibrous diamonds from Jwaneng, Botswana. *Geochimica et Cosmochimica Acta*, 58(2), 761-771.
- Schulze, D. J. (1989). Constraints on the abundance of eclogite in the upper mantle. *Journal of Geophysical Research: Solid Earth* (1978–2012), 94(B4), 4205-4212.
- Schulze, D. J., Harte, B., Valley, J. W., & Channer, D. M. D. (2004). Evidence of subduction and crust–mantle mixing from a single diamond. *Lithos*, 77(1), 349-358.
- Sebagenzi, M. N., Vasseur, G., & Louis, P. (1993). First heat flow density determinations from southeastern Zaire (central Africa). *Journal of African Earth Sciences (and the Middle East)*, 16(4), 413–423.
- Shatsky, V., Ragozin, A., Zedgenizov, D., & Mityukhin, S. (2008). Evidence for multistage evolution in a xenolith of diamond-bearing eclogite from the Udachnaya kimberlite pipe. *Lithos*, 105(3), 289–300.
- Shirey, S. B., & Richardson, S. H. (2011). Start of the Wilson cycle at 3 Ga shown by diamonds from subcontinental mantle. *Science*, 333(6041), 434–436.
- Shiryaev, A.A., Izraeli, E.S., Hauri, E.H., Zakharchenko, O.D. & Navon, O. (2005). Chemical, optical and isotopic investigation of fibrous diamonds from Brazil. *Russian Geology and Geophysics*, 46(12), 1185–1201.
- Smart, K. A., Chacko, T., Stachel, T., Muehlenbachs, K., Stern, R. A., & Heaman, L. M. (2011). Diamond growth from oxidized carbon sources beneath the Northern Slave Craton, Canada: a $\delta^{13}\text{C}$ –N study of eclogite-hosted diamonds from the Jericho kimberlite. *Geochimica et Cosmochimica Acta*, 75(20), 6027–6047.
- Smart, K. A., Chacko, T., Stachel, T., Tappe, S., Stern, R. A., & Ickert, R. B. (2012). Eclogite formation beneath the northern Slave craton constrained by diamond inclusions: Oceanic lithosphere origin without a crustal signature. *Earth and Planetary Science Letters*, 319, 165–177.
- Smit, K. V., Stachel, T., & Stern, R. A. (2014). Diamonds in the Attawapiskat area of the Superior craton (Canada): evidence for a major diamond-forming event younger than 1.1 Ga. *Contributions to Mineralogy and Petrology*, 167(1), 1–16.
- Smith, E. M., & Kopylova, M. G. (2014). Implications of metallic iron for diamonds and nitrogen in the sublithospheric mantle. *Canadian Journal of Earth Sciences*, 51(5), 510–516.
- Smith, E. M., Kopylova, M. G., Frezzotti, M. L., & Afanasiev, V. P. (2015). Fluid inclusions in Ebelyakh diamonds: Evidence of CO₂ liberation in eclogite and the effect of H₂O on diamond habit. *Lithos*, 216, 106-117.
- Smith, E. M., Kopylova, M. G., Nowell, G. M., Pearson, D. G., & Ryder, J. (2012). Archean mantle fluids preserved in fibrous diamonds from Wawa, Superior craton. *Geology*, 40(12), 1071-1074.
- Sobolev, V. S., & Sobolev, N. V. (1980). New proof on very deep subsidence of eclogitized crustal rocks. *Doklady Akademii Nauk SSSR*, 250(3), 683-685.
- Sobolev, N.V., Yefimova, E.S. and Koptil, V.I. (1999). Mineral inclusions in diamonds in the Northeast of the Yakutian diamondiferous province. In: J.J. Gurney, J.L. Gurney, M.D. Pascoe and S.H. Richardson (Eds.), *The P.H. Nixon Volume, Proceedings of the VIIth International Kimberlite Conference* (pp. 816–822). Capetown, South Africa: Red Roof Design.
- Stachel, T., & Harris, J. W. (2008). The origin of cratonic diamonds—constraints from mineral inclusions. *Ore Geology Reviews*, 34(1), 5–32.
- Stachel, T., Banas, A., Muehlenbachs, K., Kurszlaukis, S. and Walker, E.C., (2006). Archean diamonds from Wawa

- (Canada): samples from deep cratonic roots predating cratonization of the Superior Province. *Contributions to Mineralogy and Petrology*, 151(6), 737–750.
- Stachel, T., Harris, J.W., Aulbach, S., Deines, P. (2002). Kankan diamonds (Guinea) III; $\delta^{13}\text{C}$ and nitrogen characteristics of deep diamonds. *Contributions to Mineralogy and Petrology*, 142, 465–475.
- Stachel, T., Harris, J. W., & Muehlenbachs, K. (2009). Sources of carbon in inclusion bearing diamonds. *Lithos*, 112, 625–637.
- Stern, R.A., Palot, M., Howell, D., Stachel, T., Pearson, D.G., Cartigny, P., & Oh, A. (2014). Methods and reference materials for SIMS diamond C- and N-isotope analysis. Canadian Centre for Isotopic Microanalysis, Research Report 14-01. University of Alberta, Education and Research Archive. Retrieved from <https://era.library.ualberta.ca/files/cc08hf71g>, December 10th, 2015.
- Stewart, K., Turner, S., Kelley, S., Hawkesworth, C., Kirstein, L., & Mantovani, M. (1996). 3-D, 40Ar – 39Ar geochronology in the Paraná continental flood basalt province. *Earth and Planetary Science Letters*, 143(1), 95–109.
- Swart, P. K., Pillinger, C. T., Milledge, H. J., & Seal, M. (1983). Carbon isotopic variation within individual diamonds. *Nature*, 303(5920), 793–795.
- Sykes, L. R. (1978). Intraplate seismicity, reactivation of preexisting zones of weakness, alkaline magmatism, and other tectonism postdating continental fragmentation. *Reviews of Geophysics*, 16(4), 621–688.
- Tack, L., Wingate, M. T. D., De Waele, B., Meert, J., Belousova, E., Griffin, B., Tahon, A., & Fernandez-Alonso, M. (2010). The 1375 Ma “Kibaran event” in Central Africa: Prominent emplacement of bimodal magmatism under extensional regime. *Precambrian Research*, 180(1), 63–84.
- Tappert, R., Stachel, T., Harris, J. W., & Shimizu, N. (2005). Mineral inclusions in diamonds from the Panda kimberlite, Slave Province, Canada. *European Journal of Mineralogy*, 17(3), 423–440.
- Taylor, W.R., Jaques, A.L., & Ridd, M. (1990). Nitrogen-defect aggregation characteristics of some Australasian diamonds: time-temperature constraints on the source regions of pipe and alluvial diamonds. *American Mineralogist*, 75, 1290–1310.
- Taylor, W. R., Canil, D., & Milledge, H. J. (1996). Kinetics of Ib to IaA nitrogen aggregation in diamond. *Geochimica et Cosmochimica Acta*, 60(23), 4725–4733.
- Thompson, R.N., Gibson, S.A., Mitchell, J.G., Dickin, A.P., Leonardos, O.H., Brod, J.A., & Greenwood, J.C. (1998). Migrating Cretaceous–Eocene magmatism in the Serra do Mar Alkaline Province, SE Brazil: melts from the deflected Trindade mantle plume? *Journal of Petrology*, 39, 1493–1526.
- Tomlinson, E. L., Jones, A. P., & Harris, J. W. (2006). Co-existing fluid and silicate inclusions in mantle diamond. *Earth and Planetary Science Letters*, 250(3), 581–595.
- Torsvik, T. H., Burke, K., Steinberger, B., Webb, S. J., & Ashwal, L. D. (2010). Diamonds sampled by plumes from the core–mantle boundary. *Nature*, 466(7304), 352–355.
- Veizer, J., Hoefs, J., Lowe, D. R., & Thurston, P. C. (1989). Geochemistry of Precambrian carbonates: II. Archean greenstone belts and Archean sea water. *Geochimica et Cosmochimica Acta*, 53(4), 859–871.
- Veizer, J., Plumb, K. A., Clayton, R. N., Hinton, R. W., & Grotzinger, J. P. (1992). Geochemistry of Precambrian carbonates: V. Late Paleoproterozoic seawater. *Geochimica et Cosmochimica Acta*, 56(6), 2487–2501.
- Walter, M.J., Kohn, S.C., Araujo, D., Bulanova, G.P., Smith, C.B., Gaillou, E., Wang, J., Steele, A. & Shirey, S.B.

- (2011). Deep mantle cycling of oceanic crust: evidence from diamonds and their mineral inclusions. *Science*, 334(6052), 54–57.
- Weiss, Y., Kessel, R., Griffin, W.L., Kiflawi, I., Klein-BenDavid, O., Bell, D.R., Harris, J.W. and Navon, O. (2009). A new model for the evolution of diamond-forming fluids: evidence from microinclusion-bearing diamonds from Kankan, Guinea. *Lithos*, 112, 660–674.
- Weiss, Y., Griffin, W. L., Elhlou, S., & Navon, O. (2008). Comparison between LA-ICP-MS and EPMA analysis of trace elements in diamonds. *Chemical Geology*, 252(3), 158–168.
- Weiss, Y., McNeill, J., Pearson, D. G., Nowell, G. M., & Ottley, C. J. (2015). Highly saline fluids from a subducting slab as the source for fluid-rich diamonds. *Nature*, 524(7565), 339–342.
- Wiggers de Vries, D.F., Bulanova, G. P., De Corte, K., Pearson, D. G., Craven, J. A., & Davies, G. R. (2013). Micro-scale coupled carbon isotope and nitrogen abundance variations in diamonds: Evidence for episodic diamond formation beneath the Siberian Craton. *Geochimica et Cosmochimica Acta*, 100, 176–199.
- Wiggers de Vries, D. F., Davies, G. R., Bulanova, G. P., & Pearson, D. G. (2007). No evidence of diffusive homogenisation of carbon isotopes in Yakutian diamonds. In *Geochimica et Cosmochimica Acta*, 71(15), A1112.
- Wiggers de Vries, D. F., Pearson, D. G., Bulanova, G. P., Smelov, A. P., Pavlushin, A. D., & Davies, G. R. (2013). Re–Os dating of sulphide inclusions zonally distributed in single Yakutian diamonds: evidence for multiple episodes of Proterozoic formation and protracted timescales of diamond growth. *Geochimica et Cosmochimica Acta*, 120, 363–394.
- Wilson, M., 1992. Magmatism and continental rifting during the opening of the South Atlantic ocean: a consequence of Lower Cretaceous super-plume activity? In: Storey, B.C., Alabaster, T., Pankhurst, R.J. (Eds.), *Magmatism and the Causes of Continental Break-up*, Geological Society Special Publication (No. 68, pp. 241–255). London.
- Zedgenizov, D. A., Harte, B., Shatsky, V. S., Politov, A. A., Rylov, G. M., & Sobolev, N. V. (2006). Directional chemical variations in diamonds showing octahedral following cuboid growth. *Contributions to Mineralogy and Petrology*, 151(1), 45–57.

Appendix A: Diamond Physical Characteristics

Sample #	Morphology	Resorption class	Weight (mg)	Colour	Surface features	Fragmentation	Silicate Inclusions
10008	Octahedral	4	15.3	Colorless	Stepped faces, slightly recessed square faces		
10187	Cube	5	13.5	Brown	Pitted square faces		
10191	Cube	3	11.8	Brown			
10199	Cubooctahedron	6	15.8	Colourless	Etch channels on square faces		
10240	Macle	6	5.8	Grey	Stepped faces, thin fibrous coat		
10243	Aggregate	6	3.9	Colorless	Fibrous, Cube triple twin		
10247	Elongate cubooctahedron	6	7.1	Green	Frosted surface		
11597	cuboid	4	3.1	Colourless	Recessed square faces	Fragment	
11599	elongate octahedron	5	6.1	Colourless	Sheaf-like striation		
11600	Unknown	3	10.4	Green	Splintery striation, green and blue-green metamict spots	Fragment	
11601	elongate octahedron	5	10.6	Green	Polycentric faces, trigons		6
11602	macle	6	14.6	Colourless			
11604	dodecahedron	1	14.5	Colourless			
11606	cuboid	4	18.1	Yellow	Recessed square faces, trigons on octahedral faces		
11608	octahedron	6	31.4	Brown	Sheaf-like striation		6
11609	dodecahedron	1	7.5	Colourless	Green to blue-green metamict spots		
11610	flat dodecahedron	1	30.2	Brown	Plastic deformation lamellae, sheaf-like striation		
11611	elongate octahedron	5	7.3	Brown	Sheaf-like striation		
11612	flat dodecahedron	1	15.1	Brown	Rhombic surface pattern, uneven coloration		2
11613	dodecahedron	1	14.5	Yellow			

Sample #	Morphology	Resorption class	Weight (mg)	Colour	Surface features	Fragmentation	Silicate Inclusions
11614	flat dodecahedron	1	9.5	Brown	Plastic deformation lamellae, brown metamict spots, coarse sheaf-like striation		
11615	octahedron	5	18.6	Colourless	Etch channels, trigons		
11617	octahedron	6	7.0	Colourless	Trigons		
11620	octahedron	3	15.5	Yellow	Rhombic surface pattern, few brown and green metamict spots		
11621	cuboid	Unknown	24.2	Grey	Recessed square faces, parallel striation		
11622	octahedron	3	15.9	Pink	Splintery striation, trigons, differential resorption		
11623	flat dodecahedron	1	8.9	Yellow	Splintery striation, few brown and blue-green metamict spots		
11624	cuboid	5	18.1	Grey	Blue-green metamict spots		
11625	octahedron	4	11.3	Brown	Sheaf-like striation, brown metamict spots		1
11626	octahedron	5	6.4	Colourless	Sheaf-like striation		8
11627	aggregate (twinned octahedra)	5	17.7	Colourless	Splintery striation, trigons		
11628	flat dodecahedron	1	26.8	Green	Sheaf-like striation		
11629	octahedron	3	29.0	Pink	Coarse sheaf-like to splintery striation		
11630	macle	4	13.2	Yellow	Trigons		
11631	octahedron	4	7.8	Brown	Brown metamict spots, trigons		
11632	dodecahedron	1	25.9	Pink	Plastic deformation lamellae, splintery striation, etch channels		
11633	macle	5	3.4	Colourless	Parallel striation		6
11634	aggregate (twinned octahedra)	5	6.4	Colourless	Sheaf-like striation		
11635	dodecahedron	1	17.5	Brown	Rhombic surface pattern, blue-green metamict spot		5
11636	octahedron	4	21.8	Light Brown	Sheaf-like striation		

Sample #	Morphology	Resorption class	Weight (mg)	Colour	Surface features	Fragmentation	Silicate Inclusions
11637	elongate octahedron	5	69.5	Colourless	Polycentric faces, splintery striation		1
11638	elongate octahedron	6	88.8	Colourless	Parallel striation, aligned trigons, etch channels, polycentric faces		
11639	aggregate (twinned octahedra)	5	20.4	Colourless	Sheaf-like striation		
11640	dodecahedron	1	22.7	Colourless	Sheaf-like striation		
11641	flat octahedron	5	64.4	Light Brown	Polycentric faces, sheaf-like striation, irregular frosted “bubble” pit		
11642	macle	5	10.1	Colourless	Sheaf-like striation		5
11643	macle	5	6.4	Light Brown	Parallel striation, trigons		
11644	octahedron	6	40.0	Light Brown	Green metamict spots		
11652	Unknown	3	4.5	Green	Recessed square faces, green metamict spots		
11653	octahedron	4	20.5	Colourless	Sheaf-like striation, blue-green metamict spots		
11654	octahedron	4	15.5	Green	Etch channels, sheaf-like striation, blue-green metamict spots		
11655	octahedron	5	6.8	Colourless	Splintery striation		4
11657	macle	5	21.4	Brown	Sheaf-like striation		
11658	cuboid	Unknown	2.5	Colourless			
11659	dodecahedron	1	23.3	Brown-Pink	Rhombic surface pattern, uneven coloration, plastic deformation lamellae		
11660	dodecahedron	1	22.4	Yellow		Chipped	
11661	Unknown	1	19.8	Colourless	Green metamict spots, plastic deformation lamellae	Fragment	
11662	macle	5	16.8	Brown	Parallel striation		1
11663	dodecahedron	1	18.8	Yellow			

Sample #	Morphology	Resorption class	Weight (mg)	Colour	Surface features	Fragmentation	Silicate Inclusions
11664	dodecahedron	1	11.0	Pink	Plastic deformation lamellae, uneven coloration		2
11665	octahedron	3	11.5	Green	Sheaf-like striation, stepped faces	Chipped	
11666	dodecahedron	2	26.0	Yellow	Rhombic surface pattern, mechanical wear pits		
11667	flat octahedron	6	0.8	Colourless			
11668	aggregate (twinned octahedra)	5	14.7	Pink	Sheaf-like striation		
11669	aggregate (twinned octahedra)	5	12.6	Brown	Trigons, splintery striation		
11670	Unknown	Unknown	77.6	Colourless		Fragment	
11672	dodecahedron	1	24.9	Light Yellow			
11687	flat dodecahedron	1	29.1	Colourless			
11690	aggregate (twinned octahedra)	3	27.6	Colourless	Sheaf-like striation, stepped faces, uneven coloration		
11691	flat octahedron	6	32.2	Pink-Brown			8
11695	cuboid	3	106.1	Yellow	Square pits, splintery striation		
11696	aggregate	Unknown	28.0	Pink	Splintery striation, stepped faces	Fragment	
11698	dodecahedron	1	19.0	Brown	Splintery striation, dark plastic deformation lamellae		
11699	octahedron	5	69.7	Colourless	Parallel striation, stepped faces, polycentric faces		3
11700	octahedron	4	84.5	Colourless	Sheaf-like striation, trigons		
11701	octahedron	6	8.3	Brown			5
11702	dodecahedron	1	17.2	Brown	Plastic deformation lamellae, splintery striation		
11703	dodecahedron	1	19.7	Brown			
11705	octahedron	6	7.1	Colourless	Trigonal to square pits		
11706	octahedron	4	10.5	Colourless	Sheaf-like striation		

Sample #	Morphology	Resorption class	Weight (mg)	Colour	Surface features	Fragmentation	Silicate Inclusions
11707	dodecahedron	2	13.6	Brown	Brown metamict spots, uneven coloration, sheaf-like striation		
11708	octahedron	3	18.3	Colourless	Sheaf-like striation, etch channels		
11710	octahedron	5	28.4	Light Brown	Parallel striation		1
11711	flat dodecahedron	1	34.1	Brown	Plastic deformation lamellae		
11712	dodecahedron	1	18.0	Brown	Rhombic surface pattern		8
11714	dodecahedron	1	9.9	Colourless			
11715	octahedron	6	6.4	Colourless	Polycentric faces	Fragment	4
11716	octahedron	5	7.9	Light Brown	Sheaf-like striation		
11717	aggregate (twinned octahedra)	5	13.3	Colourless	Parallel striation		
11720	octahedron	4	5.9	Colourless	Sheaf-like striation		1
11721	aggregate (twinned macles)	4	21.1	Colourless	Sheaf-like striation		
11722	dodecahedron	1	17.6	Light Yellow	Splintery striation		
11723	octahedron	4	14.6	Colourless	Parallel to splintery striation, trigons		
11725	octahedron	4	9.5	Pink-Brown	Sheaf-like striation		
11726	aggregate (twinned octahedra)	5	28.8	Colourless	Sheaf-like striation, trigons		
11727	Unknown	1	15.2	Yellow		Fragment	
11728	cuboid	3	6.6	Yellow-Brown	Square pits, differential resorption		
11729	octahedron	5	7.0	Colourless	Parallel striation		
11730	dodecahedron	2	21.2	Brown	Parallel to splintery striation		5
11731	aggregate (twinned octahedra)	4	24.4	Colourless	Sheaf-like striation, green metamict spots, trigons		1
11732	octahedron	6	5.1	Brown			2

Sample #	Morphology	Resorption class	Weight (mg)	Colour	Surface features	Fragmentation	Silicate Inclusions
11733	octahedron	5	4.7	Colourless	Stepped faces, polycentric faces		
11734	dodecahedron	1	19.0	Light Brown			
11738	macle	5	34.0	Light Brown	Sheaf-like striation		2
11740	aggregate (twinned octahedra)	5	7.8	Colourless	Parallel to splintery striation, polycentric faces		
11741	cuboid	Unknown	1.5	Yellow	Recessed cube faces with square pits		
11742	octahedron	5	8.8	Greenish	Splintery striation, polycentric faces		
11743	octahedron	5	4.3	Colourless	Parallel striation		
11744	flat dodecahedron	1	30.2	Colourless	Splintery striation		
11745	dodecahedron	2	6.5	Pink	Splintery striation		
11746	octahedron	6	7.4	Light Brown			8
11747	octahedron	5	7.9	Colourless	Sheaf-like striation, trigons		3
11750	dodecahedron	1	9.8	Yellow			
11751	octahedron	5	5.4	Green	Splintery striation		
11752	dodecahedron	1	30.4	Brown	Plastic deformation lamellae, splintery striation, light rhombic surface pattern		
11753	macle	5	5.4	Colourless	Splintery striation	Chipped	3
11754	elongate octahedron	1	7.2	Yellow			
11755	octahedron	5	8.1	Colourless	Sheaf-like striation, polycentric faces		
MB3-1	octahedron	6	12.0	Light Brown			3
MB3-2	flat octahedron	5	21.8	Light Brown	Sheaf-like striation, trigonal pits		
MB3-3	octahedron	5	12.8	Light Brown	Sheaf-like striation		1

Sample #	Morphology	Resorption class	Weight (mg)	Colour	Surface features	Fragmentation	Silicate Inclusions
MB3-4	elongate octahedron	6	7.2	Light Yellow	Minor chips at edges		1
MB3-5	dodecahedron	1	3.2	Colourless			
MB3-6	dodecahedron	1	3.2	Light Brown			
10274	Cube	-	4.8	Black	Fibrous		
10284	Cube	-	4.7	Grey	Fibrous coat		
10305	Cube	-	9.1	Colorless	Fibrous		
10312	Cube	-	7.2	Light yellow	Fibrous		
10313	Cube	-	6.4	Yellow	Fibrous		
MB3-7	Aggregate	-	14.5	Light yellow	Fibrous, intergrown cubes		
MB3-8	Cube	-	12.7	Yellow	Fibrous, intergrown cubes		
MB2-1	Cube	-	16.7	Yellow	Fibrous coat		
MB2-2	Cube	-	22.5	Yellow	Etch channels		
MB2-3	Cube	-	16.4	Grey	Fibrous		
MB2-4	Cube	-	11.1	Yellow	Fibrous		
MB2-5	Aggregate	-	99.3	Yellow	Fibrous, intergrown cubes		
MB2-6	Cube	-	15.2	Grey	Fibrous		
11671	Cube	-	200.2	Grey	Fibrous		

Appendix B: EPMA Data of Silicate Inclusions

Sample	11612	11637	11691	11691	11699	11701	11710	11715	11715	11720	11730
Mineral ^a	Ol	Ol	Ol	Ol	Ol	Ol	Ol	Ol	Ol	Ol	Ol
# grains analyzed	2	1	1	6	3	2	1	2	1	1	4
# analyses averaged	3	2	3	15	7	4	2	4	2	3	9
SiO ₂	40.70	41.72	41.87	41.19	41.36	41.44	41.06	41.54	42.01	41.36	41.56
TiO ₂	*	*	*	*	*	*	*	*	*	*	*
Al ₂ O ₃	0.03	*	*	0.04	*	0.05	*	0.06	0.09	*	0.04
Cr ₂ O ₃	0.10	*	*	*	*	*	*	*	*	*	*
FeO	7.25	7.23	8.98	6.85	7.22	6.53	7.11	6.83	7.14	7.13	5.62
MnO	*	0.10	0.11	0.09	0.08	0.08	0.10	*	0.08	0.09	*
NiO	0.34	0.40	0.29	0.40	0.36	0.37	0.42	0.37	0.33	0.38	0.37
MgO	51.11	51.82	48.41	51.68	51.19	51.24	51.81	50.93	49.87	51.33	51.72
CaO	0.04	*	*	0.03	*	0.04	*	0.05	0.04	0.03	*
Na ₂ O	—	—	—	—	—	—	—	—	—	—	—
K ₂ O	—	—	—	—	—	—	—	—	—	—	—
Total	99.64	101.33	99.74	100.34	100.29	99.80	100.55	99.90	99.62	100.41	99.49
Mg/(Mg+Fe)	92.30	92.70	90.60	93.10	92.70	93.30	92.80	93.00	92.60	92.80	94.30
Si	1.007	0.998	1.022	0.994	1.000	1.003	0.991	1.005	1.019	0.998	1.005
Ti	0.000	*	*	*	*	*	*	*	*	*	*
Al	0.001	*	*	0.001	*	0.001	*	0.002	0.003	*	0.001
Cr	0.003	*	*	*	*	*	*	*	*	*	*
Fe	0.134	0.145	0.183	0.138	0.146	0.132	0.144	0.138	0.145	0.144	0.114
Mn	*	0.002	0.002	0.002	0.002	0.002	0.002	*	0.002	0.002	*
Ni	0.008	0.008	0.006	0.008	0.007	0.007	0.008	0.003	0.006	0.007	0.007
Mg	1.840	1.848	1.762	1.859	1.844	1.849	1.863	1.837	1.803	1.847	1.864
Ca	0.001	*	*	0.001	*	0.001	*	0.001	0.001	0.001	*
Na	—	—	—	—	—	—	—	—	—	—	—
K	—	—	—	—	—	—	—	—	—	—	—
Total	3.012	3.002	2.977	3.005	3.000	2.996	3.009	2.129	2.979	3.001	2.994

^a ol = olivine, opx = orthopyroxene, cpx = clinopyroxene, gt = garnet * Below detection limit — Not analyzed

Sample	11732	11747	MB3-1	MB3-3	MB3-4	11608				11626	
Mineral ^a	Ol	Ol	Ol	Ol	Opx	Oli	Ol	Opx	Opx	Ol	Ol
# grains analyzed	1	3	2	1	1	1	2	1	2	4	1
# of analyses averaged	1	5	3	2	3	1	4	2	4	11	1
SiO2	40.64	41.30	42.02	41.85	58.44	40.41	41.10	56.86	57.56	41.23	41.04
TiO2	*	0.05	*	*	*	*	*	*	*	*	*
Al2O3	0.01	0.05	0.05	0.03	0.42	0.08	0.03	0.85	0.54	0.04	0.08
Cr2O3	*	*	*	*	0.29	*	*	0.40	0.38	*	0.12
FeO	6.76	6.93	5.93	5.66	4.37	7.97	7.02	4.80	4.15	7.69	7.88
MnO	*	0.09	*	0.11	0.10	0.08	0.08	0.10	0.11	0.10	0.09
NiO	0.32	0.35	0.33	0.37	0.12	0.46	0.37	0.14	0.14	0.40	0.33
MgO	51.67	51.29	51.20	50.69	35.54	50.05	51.13	34.95	36.23	50.57	50.42
CaO	*	0.04	*	0.06	0.41	0.12	0.03	0.93	0.49	0.04	0.11
Na2O	—	—	—	—	*	—	—	0.28	0.11	—	—
K2O	—	—	—	—	*	—	—	*	0.04	—	—
Total	99.52	100.10	99.65	98.80	99.73	99.18	99.83	99.34	99.75	100.13	100.09
Mg/(Mg+Fe)	93.20	93.00	93.90	94.10	93.20	91.80	92.85	92.80	94.00	92.10	91.90
Si	0.989	0.999	1.014	1.017	2.001	1.008	0.997	1.969	1.975	1.000	0.997
Ti	*	0.001	*	*	0.001	*	*	*	*	*	*
Al	0.000	0.001	0.001	0.002	0.017	0.002	0.001	0.035	0.022	0.001	0.002
Cr	*	*	*	*	0.008	*	*	0.011	0.010	*	0.002
Fe	0.138	0.140	0.120	0.115	0.125	0.123	0.142	0.139	0.119	0.156	0.160
Mn	*	0.002	*	0.002	0.003	0.001	0.002	0.004	0.003	0.002	0.007
Ni	0.006	0.007	0.007	0.007	0.003	0.008	0.007	0.003	0.004	0.008	0.002
Mg	1.875	1.849	1.841	1.837	1.814	1.849	1.850	1.803	1.853	1.829	1.826
Ca	*	0.001	*	0.001	0.015	0.001	0.001	0.035	0.018	0.001	0.003
Na2O	—	—	—	—	0.001	—	—	0.019	0.007	—	—
K2O	—	—	—	—	0.000	—	—	*	0.002	—	—
Total	3.010	3.000	2.985	2.982	3.987	2.991	3.001	4.018	3.989	2.998	3.000

^a ol = olivine, opx = orthopyroxene, cpx = clinopyroxene, gt = garnet

* Below detection limit

— Not analyzed

Sample	11626		11633		11655†			11738	11746		
Mineral ^a	Ol	Opx	Ol	Opx	Opx	Opx	Opx	Opx	Ol	Ol	Opx
# grains analyzed	1	1	3	1	2	1	2	1	3	4	1
# analyses averaged	1	3	4	1	4	3	4	3	7	7	3
SiO2	41.51	57.05	41.53	55.59	57.38	56.86	58.17	58.21	41.34	41.26	57.53
TiO2	*	*	*	*	*	*	*	*	*	*	*
Al2O3	*	0.53	0.04	1.72	0.94	0.85	0.45	0.78	0.05	0.06	0.44
Cr2O3	0.06	0.50	*	0.80	0.42	0.40	0.34	0.54	*	*	0.34
FeO	7.42	4.61	6.60	5.49	4.25	4.80	4.35	4.20	7.78	7.41	4.82
MnO	0.10	0.13	0.10	*	0.11	0.10	0.12	0.12	0.11	0.09	0.11
NiO	0.41	0.17	0.42	0.12	0.12	0.14	0.14	0.10	0.41	0.37	0.16
MgO	51.40	35.93	50.89	33.71	35.69	34.95	36.24	36.13	50.54	50.47	36.30
CaO	*	0.33	0.07	0.71	0.49	0.93	0.39	0.38	0.04	0.04	0.62
Na2O	—	*	—	0.14	0.03	0.28	0.11	0.03	—	—	0.15
K2O	—	*	—	0.12	*	*	*	*	—	—	*
Total	100.96	99.28	99.68	98.51	99.45	99.34	100.34	100.47	100.30	99.74	100.48
Mg/(Mg+Fe)	92.50	93.30	93.20	91.60	93.70	92.80	93.70	93.90	92.10	92.50	93.10
Si	0.998	1.971	1.007	1.948	1.974	1.976	1.986	1.980	1.002	1.003	1.967
Ti	*	*	*	*	*	*	*	*	*	*	*
Al	*	0.022	0.001	0.071	0.038	0.038	0.017	0.031	0.001	0.002	0.018
Cr	0.001	0.014	*	0.022	0.012	0.014	0.009	0.015	*	*	0.009
Fe	0.149	0.133	0.134	0.161	0.122	0.133	0.121	0.119	0.157	0.151	0.138
Mn	0.002	0.004	0.002	*	0.003	0.003	0.003	0.003	0.003	0.003	0.003
Ni	0.008	0.005	0.008	0.003	0.003	0.003	0.004	0.003	0.006	0.006	0.004
Mg	1.842	1.850	1.839	1.761	1.830	1.800	1.845	1.832	1.824	1.829	1.851
Ca	*	0.012	0.002	0.027	0.018	0.024	0.013	0.014	0.001	0.001	0.023
Na2O	—	*	—	0.009	0.002	0.014	0.005	0.002	—	—	0.010
K2O	—	*	—	0.005	*	*	*	*	—	—	*
Total	3.001	4.011	2.992	4.012	4.002	4.006	4.004	3.998	2.996	2.995	4.024

^a ol = olivine, opx = orthopyroxene, cpx = clinopyroxene, gt = garnet

* Below detection limit

— Not analyzed

Sample	11753			11635		11642		11664	11731	11601	11601
Mineral ^a	Ol	Opx	Opx	Cpx	Cpx	Cpx	Cpx	Cpx	Cpx	Gt	Gt
# grains analyzed	1	1	1	3	2	4	1	2	1	4	1
# analyses averaged	2	2	2	6	6	7	4	7	5	8	1
SiO2	41.65	57.49	57.40	54.59	54.51	53.75	53.18	54.96	55.09	39.47	39.51
TiO2	*	*	*	0.62	0.26	0.40	0.41	0.34	0.36	*	*
Al2O3	*	0.16	0.28	11.66	10.73	9.41	9.21	5.07	9.05	22.07	21.52
Cr2O3	*	0.22	0.18	0.16	0.16	*	*	0.18	*	*	*
FeO	6.82	4.18	4.48	5.33	5.85	8.10	8.49	8.87	6.47	17.52	17.33
MnO	0.08	0.12	0.12	*	0.09	0.09	*	0.20	*	0.29	0.32
NiO	0.36	0.15	0.13	*	*	0.04	*	*	*	—	—
MgO	50.52	36.09	35.80	9.17	10.05	8.41	8.43	16.75	9.90	9.95	9.61
CaO	*	0.45	0.63	11.72	11.13	13.26	13.27	9.78	12.30	9.14	8.94
Na2O	—	0.06	0.32	5.59	5.52	4.68	4.65	3.06	5.33	0.33	0.48
K2O	—	*	*	0.18	0.16	0.44	0.44	0.08	0.58	—	—
Total	99.53	98.95	99.37	99.12	98.39	98.59	98.14	99.31	98.92	98.83	97.77
Mg/(Mg+Fe)	93.00	93.90	93.40	75.40	75.40	64.90	63.90	77.10	73.20	50.30	49.70
Si	1.011	1.987	1.981	1.959	1.972	1.976	1.969	1.990	1.996	3.000	3.034
Ti	*	*	*	0.017	0.007	0.011	0.011	0.009	0.010	*	*
Al	*	0.007	0.011	0.493	0.457	0.408	0.402	0.217	0.387	1.977	1.947
Cr	*	0.006	0.005	0.005	0.005	*	*	0.005	*	*	*
Fe	0.139	0.121	0.129	0.160	0.177	0.249	0.263	0.269	0.196	1.114	1.113
Mn	0.002	0.004	0.004	*	0.003	0.002	*	0.006	*	0.019	0.021
Ni	0.007	0.004	0.004	*	*	0.002	*	*	*	—	—
Mg	1.828	1.859	1.842	0.490	0.542	0.461	0.466	0.904	0.535	1.127	1.100
Ca	*	0.017	0.023	0.451	0.431	0.522	0.527	0.380	0.478	0.744	0.735
Na2O	—	0.004	0.021	0.389	0.387	0.334	0.334	0.215	0.375	0.049	0.072
K2O	—	*	*	0.008	0.008	0.020	0.021	0.004	0.027	—	—
Total	2.988	4.009	4.021	3.974	3.985	3.986	3.992	3.998	3.992	8.034	8.026

^a ol = olivine, opx = orthopyroxene, cpx = clinopyroxene, gt = garnet

* Below detection limit

— Not analyzed

Sample	11712	
Mineral ^a	Cpx	Gt
# grains analyzed	1	2
# analyses averaged	1	3
SiO2	54.26	39.49
TiO2	0.61	0.68
Al2O3	15.13	22.33
Cr2O3	*	*
FeO	3.97	15.62
MnO	*	0.27
NiO	*	—
MgO	6.50	9.73
CaO	10.24	10.31
Na2O	6.98	0.24
K2O	0.21	—
Total	97.97	98.72
Mg/(Mg+Fe)	71.30	52.60
Si	1.948	2.988
Ti	0.016	0.039
Al	0.640	1.991
Cr	*	*
Fe	0.119	0.988
Mn	*	0.017
Ni	*	—
Mg	0.348	1.098
Ca	0.394	0.836
Na2O	0.486	0.035
K2O	0.010	—
Total	3.963	7.994

^a ol = olivine, opx = orthopyroxene, cpx = clinopyroxene, gt = garnet

* Below detection limit

— Not analyzed

Appendix C: Precision of EPMA analyses of polished mineral inclusions

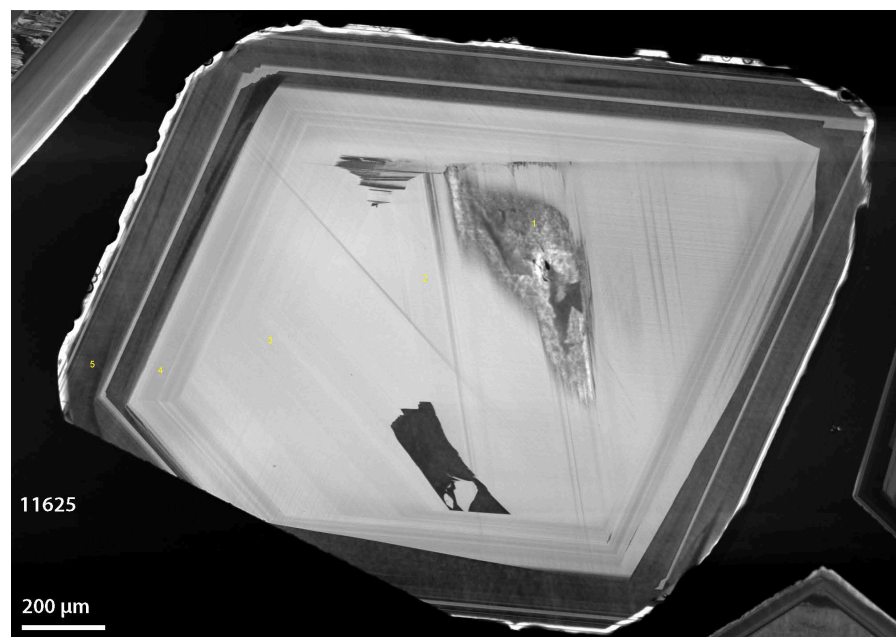
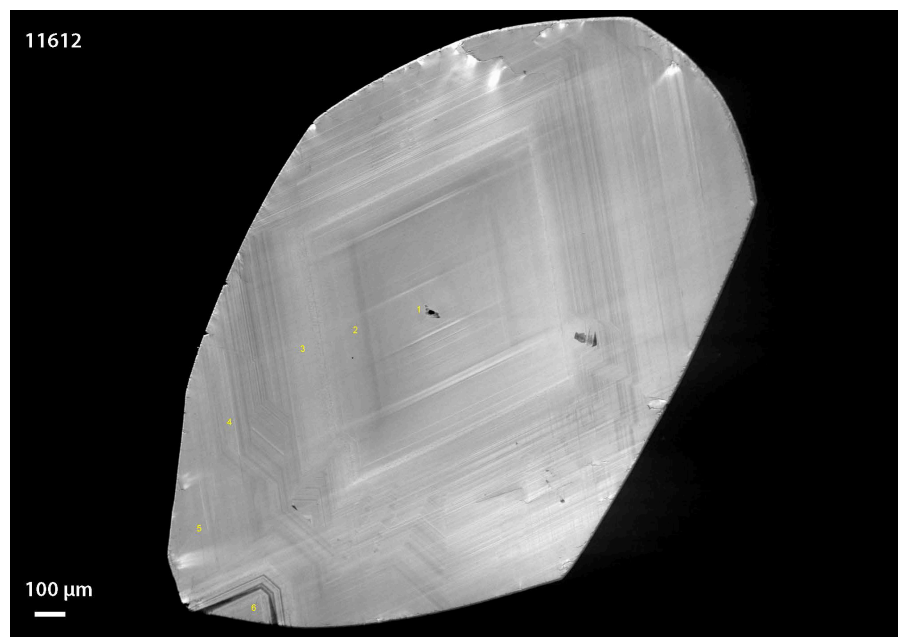
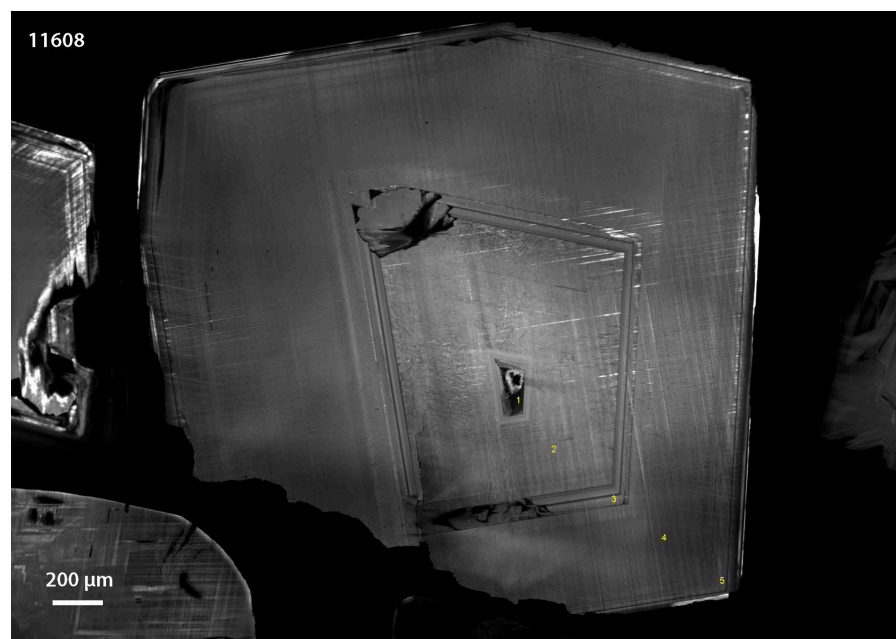
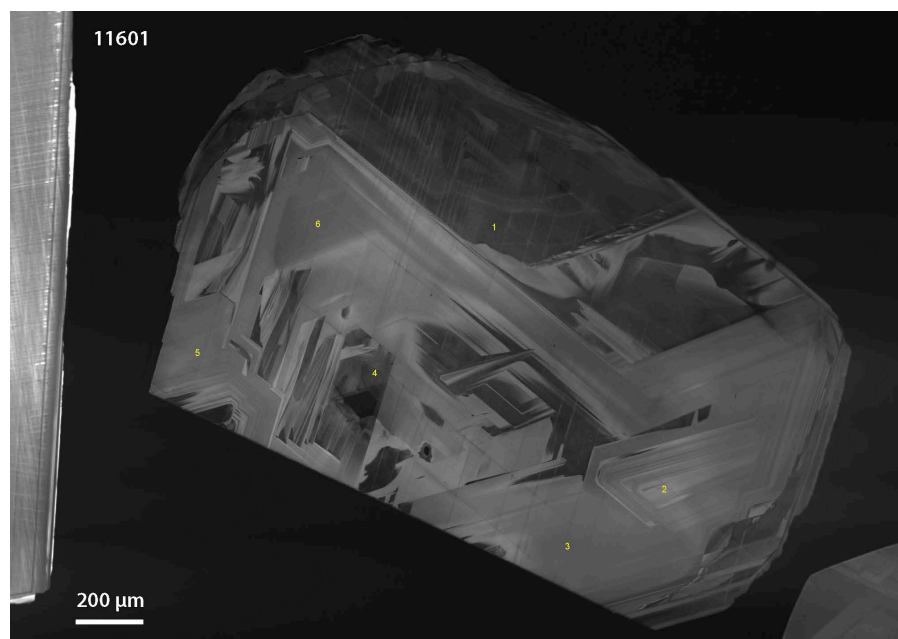
Phase	Olivine		Orthopyroxene		Clinopyroxene		Garnet	
Statistic	MDL ¹	2 σ ²	MDL	2 σ	MDL	2 σ	MDL	2 σ
SiO ₂	0.03	0.13	0.03	0.15	0.03	0.15	0.04	0.14
TiO ₂	0.04	0.01	0.04	0.02	0.04	0.03	0.05	0.03
Al ₂ O ₃	0.03	0.01	0.03	0.02	0.03	0.07	0.05	0.12
Cr ₂ O ₃	0.08	0.03	0.08	0.05	0.08	0.04	0.09	0.04
FeO	0.08	0.17	0.09	0.13	0.08	0.16	0.10	0.31
MnO	0.08	0.04	0.08	0.05	0.08	0.04	0.09	0.05
NiO	0.11	0.07	0.11	0.05	0.11	0.05	–	–
MgO	0.03	0.20	0.03	0.20	0.03	0.09	0.03	0.09
CaO	0.03	0.02	0.04	0.03	0.04	0.13	0.04	0.11
Na ₂ O	–	–	0.03	0.01	0.05	0.08	0.05	0.03
K ₂ O	–	–	0.04	0.01	0.04	0.03	–	–

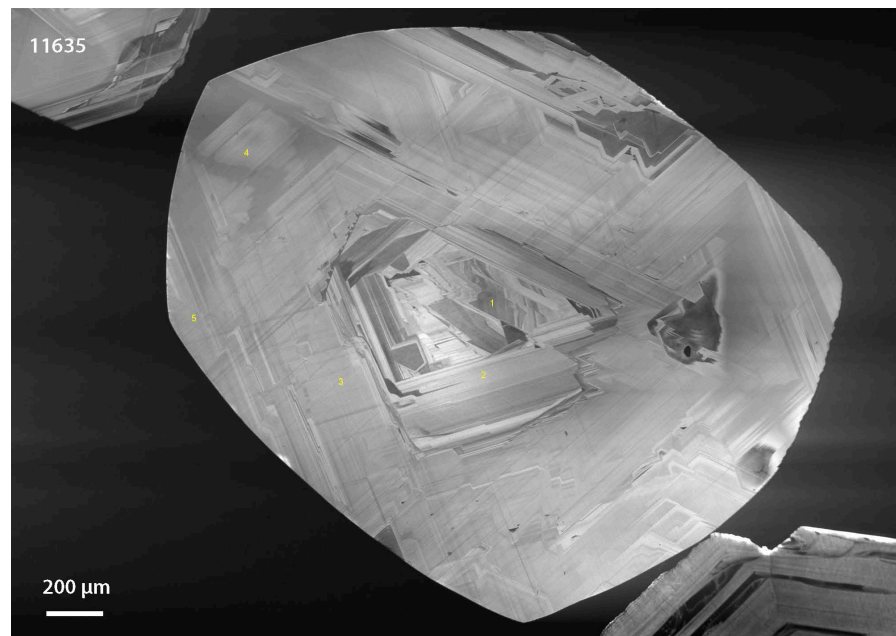
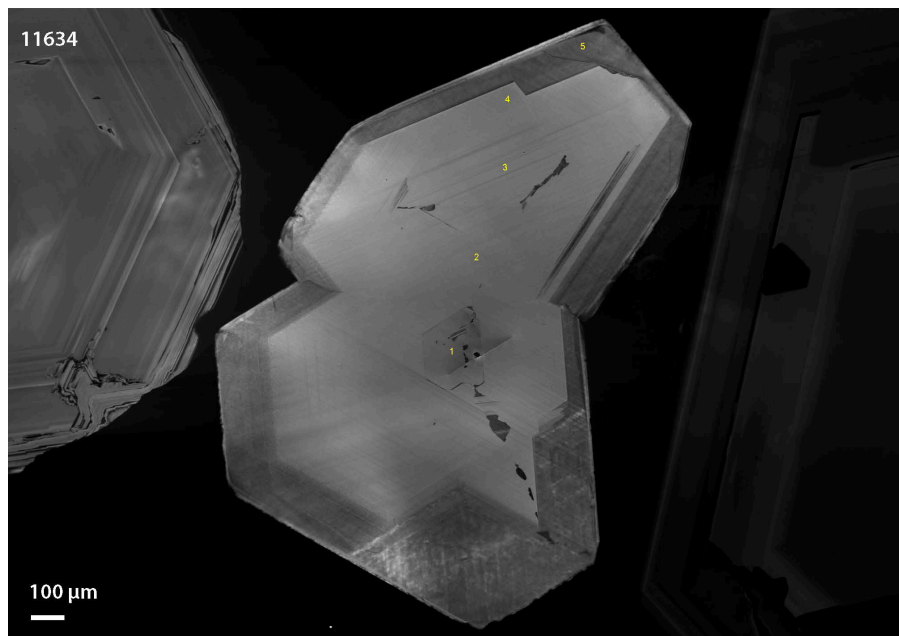
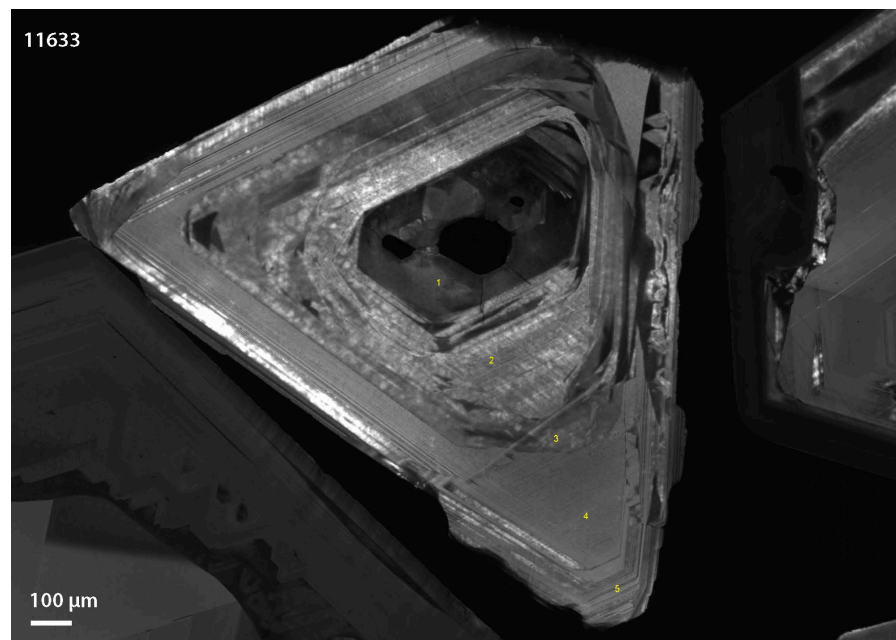
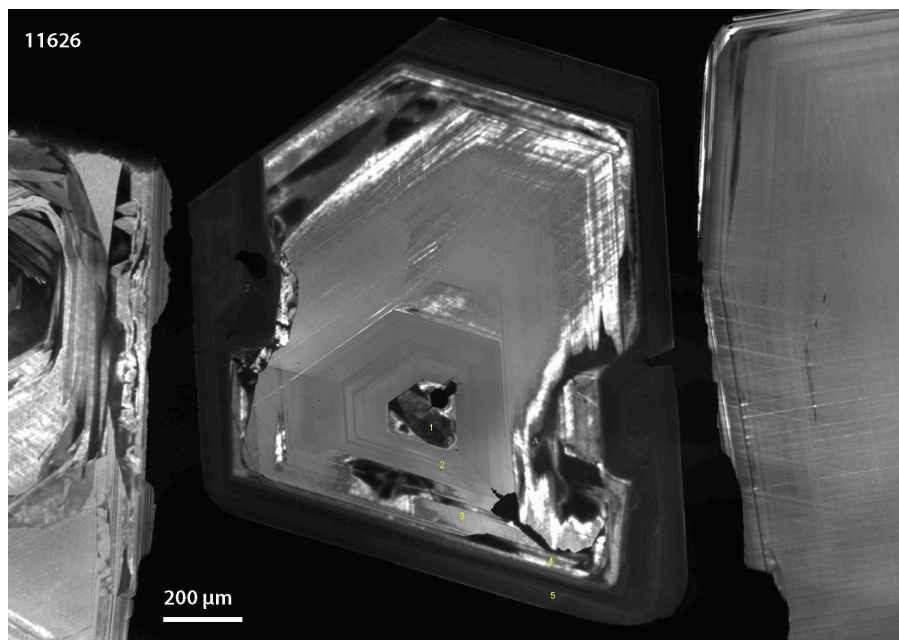
¹ Minimum detection limit

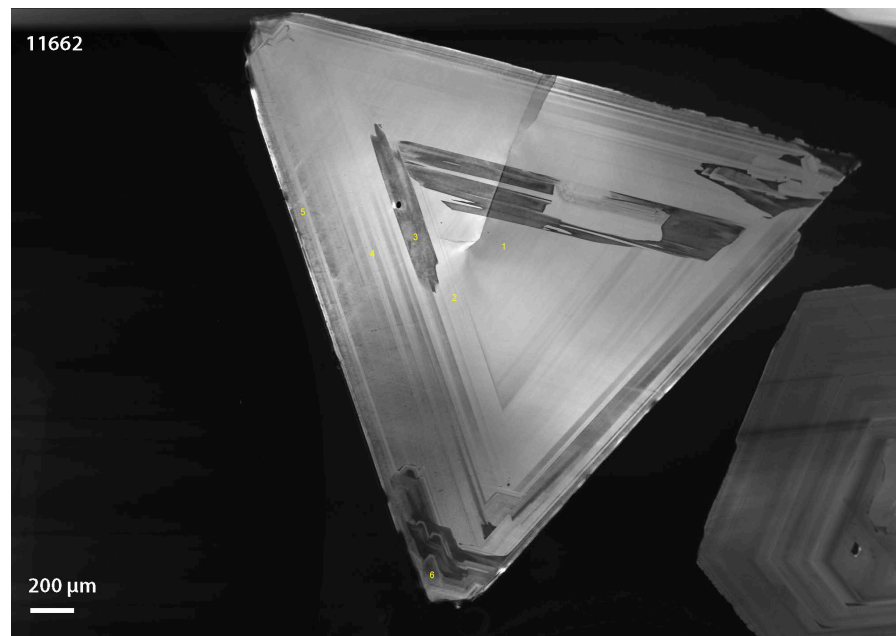
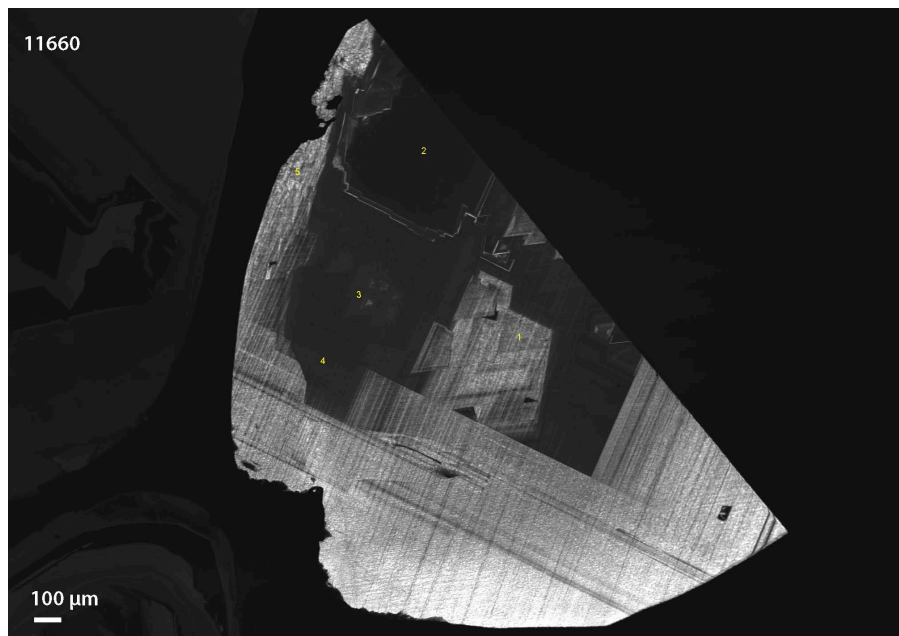
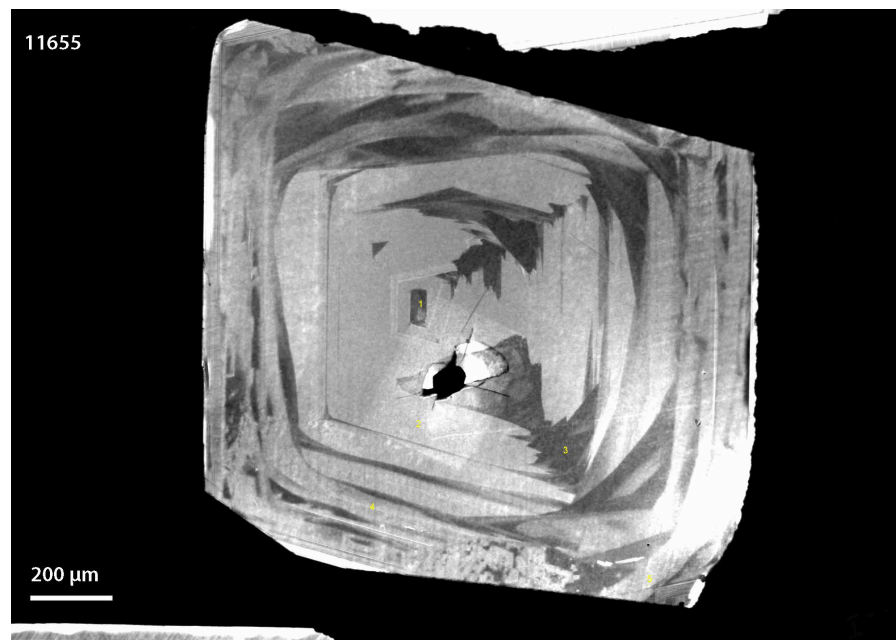
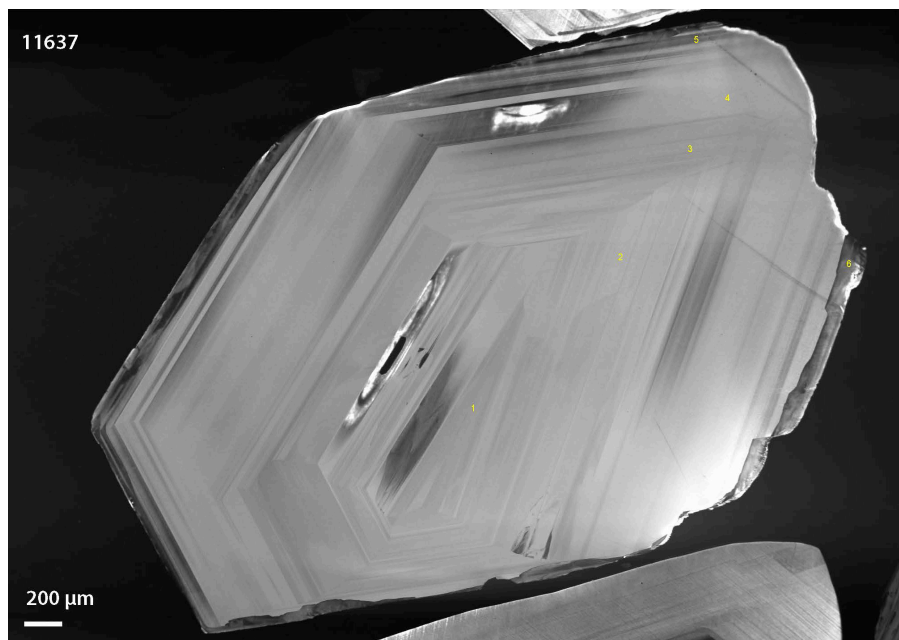
² 95% confidence interval

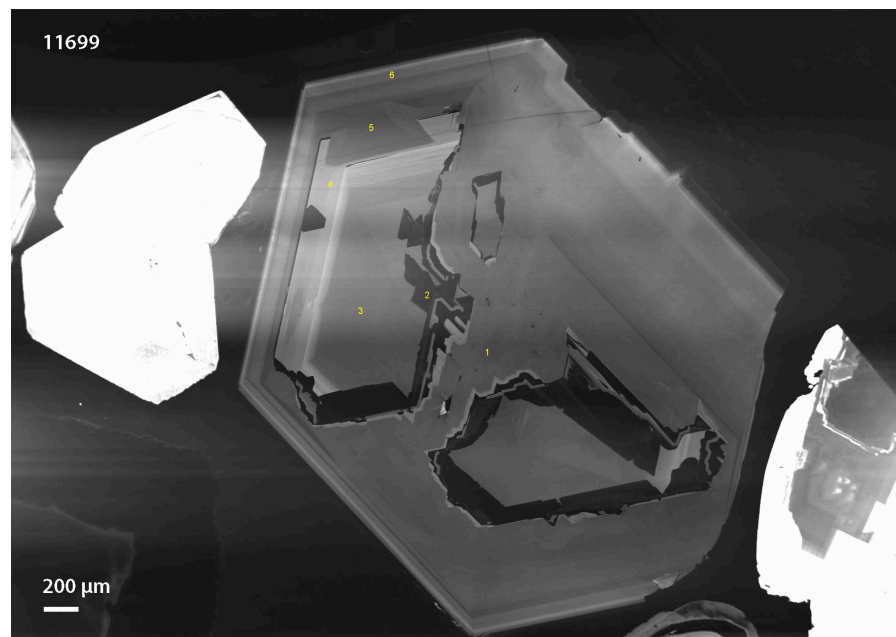
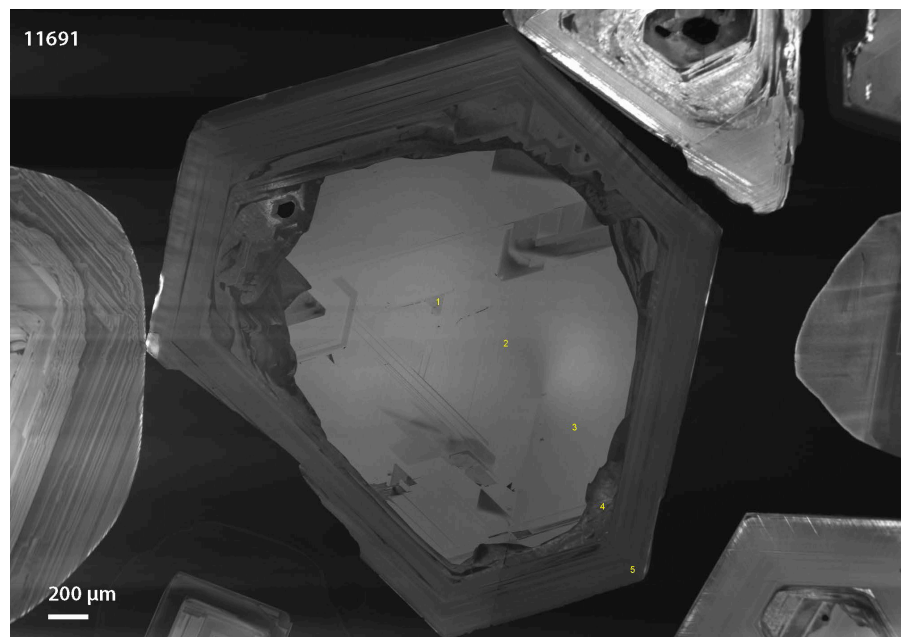
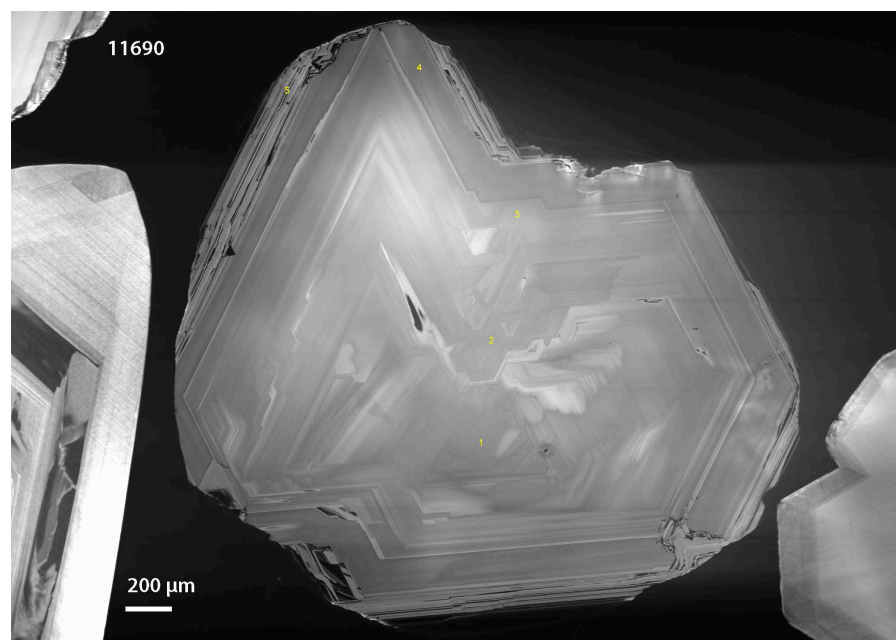
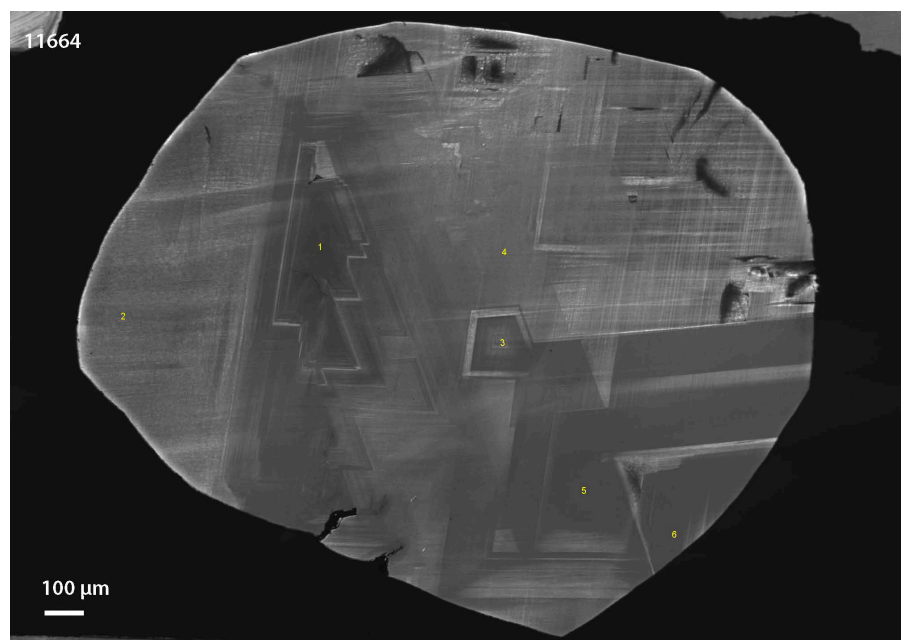
– Not analyzed

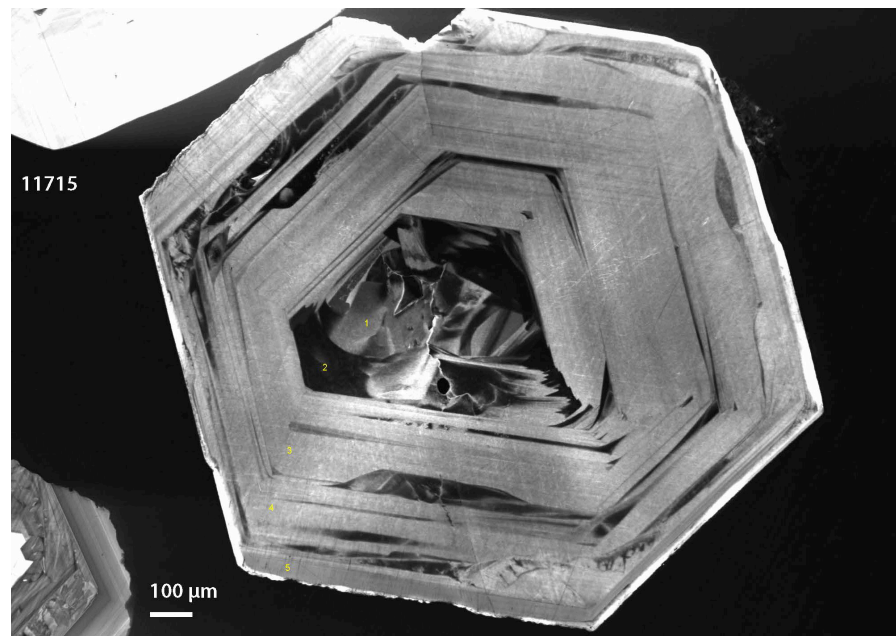
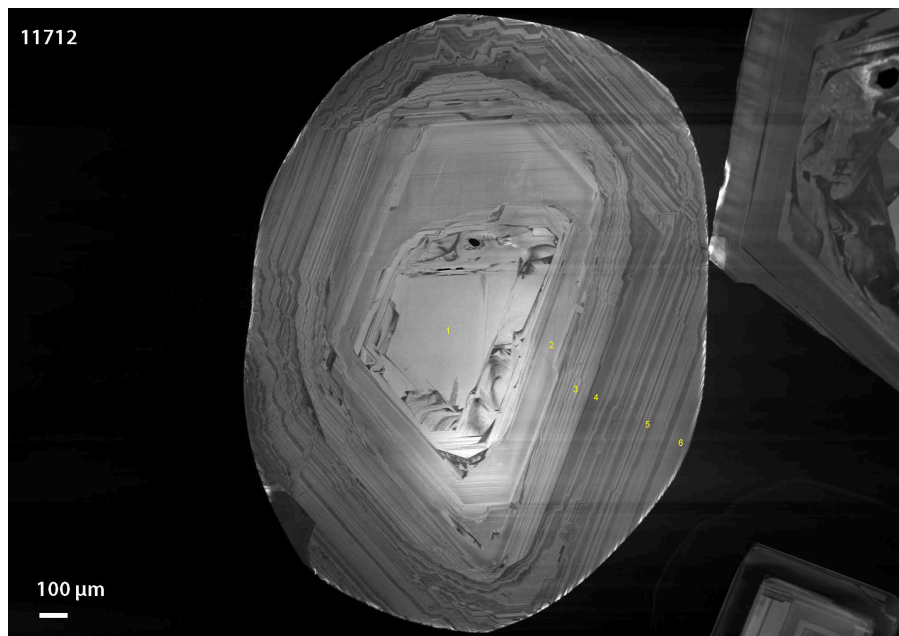
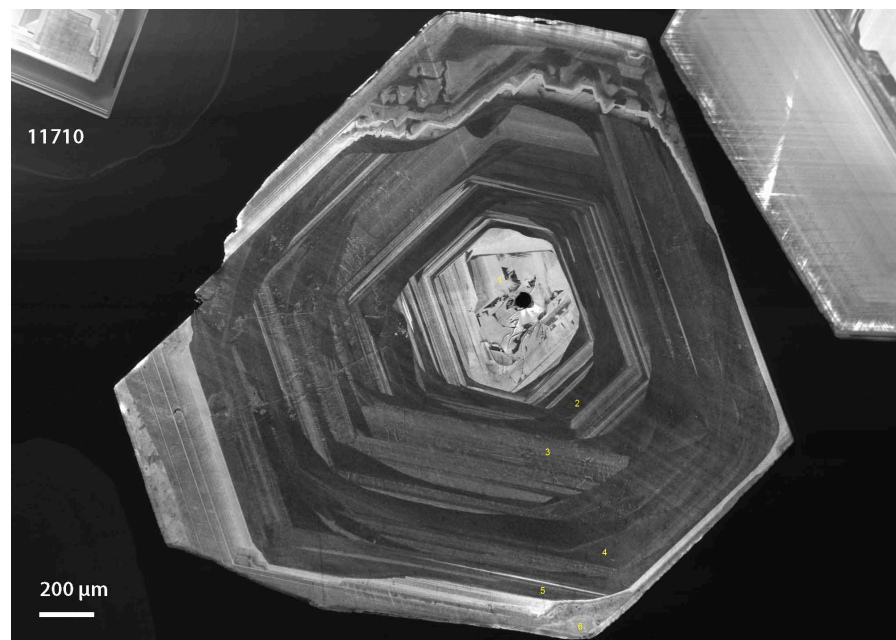
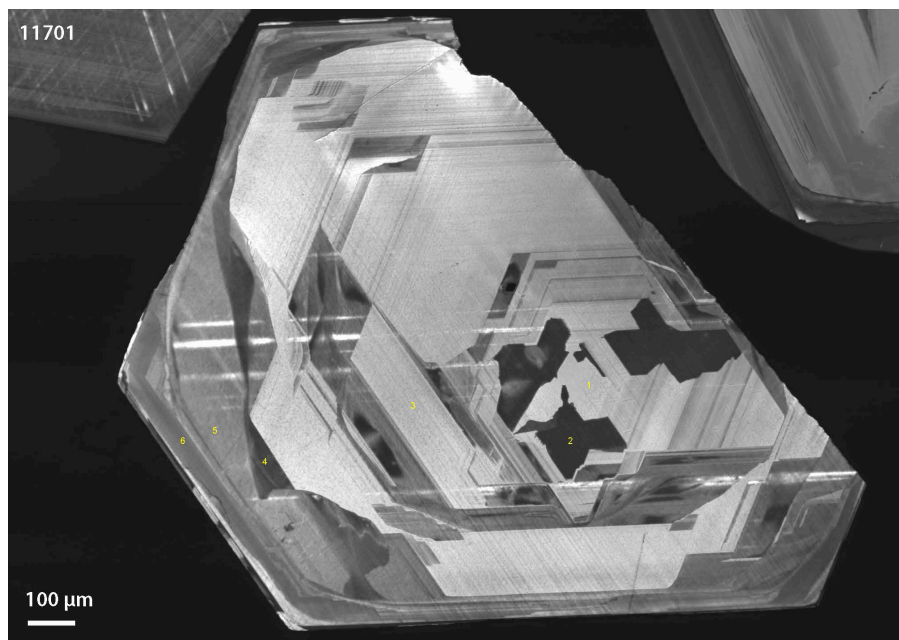
MDLs and precision calculated via EMP XmasPlus software

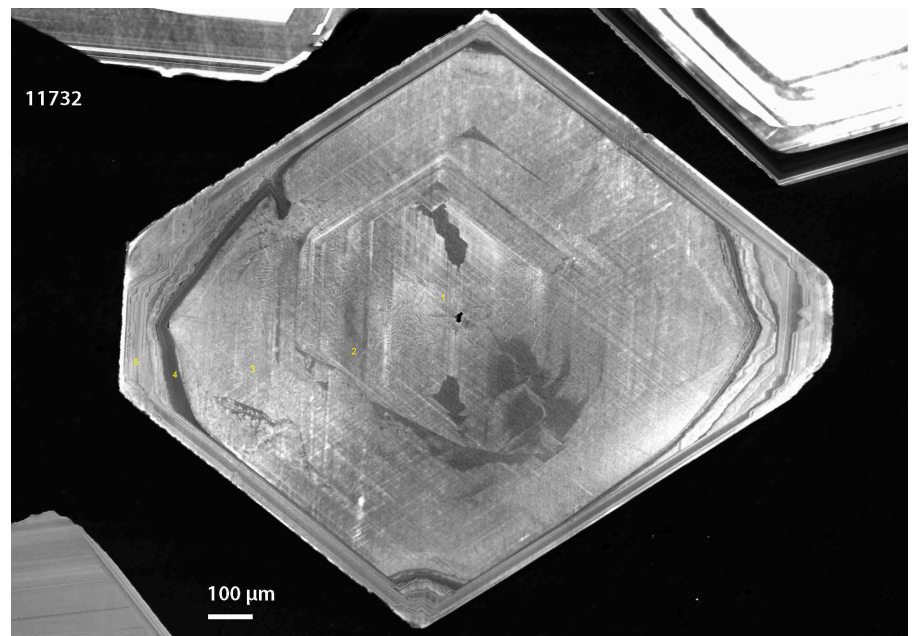
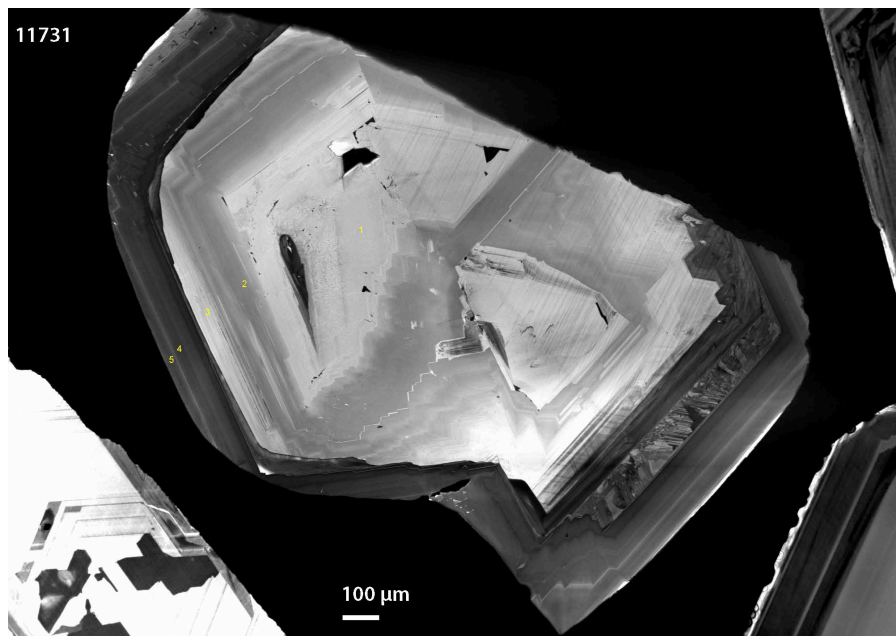
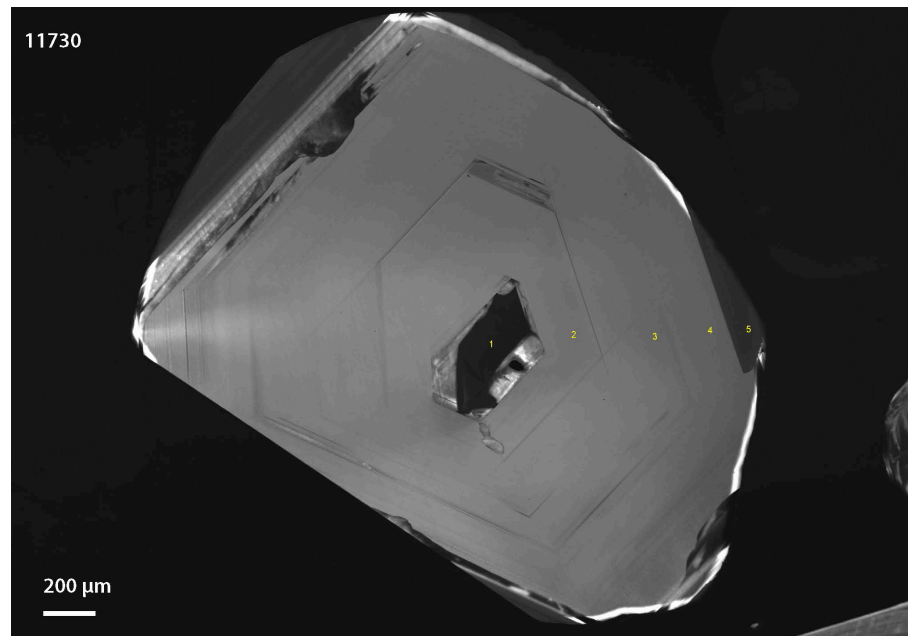


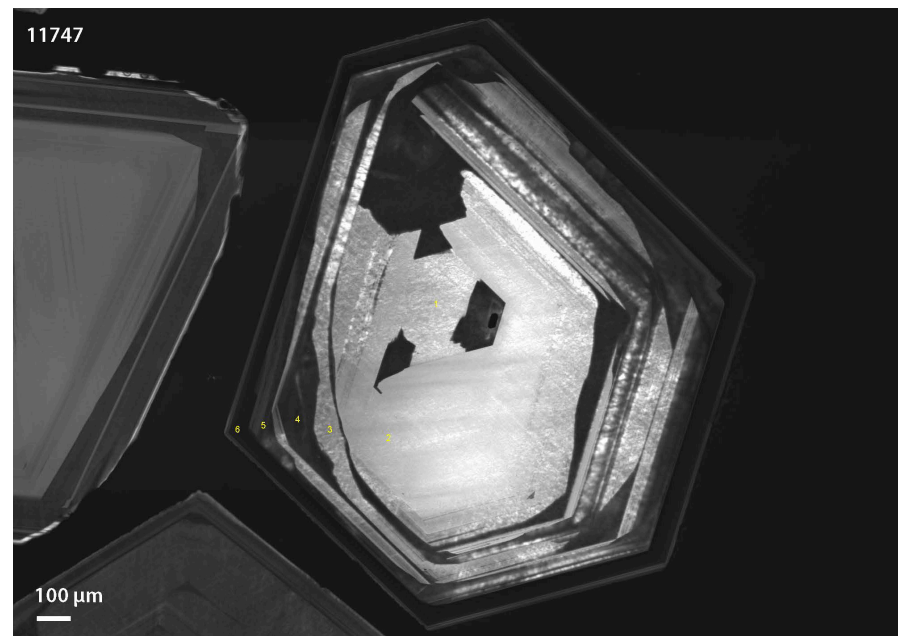
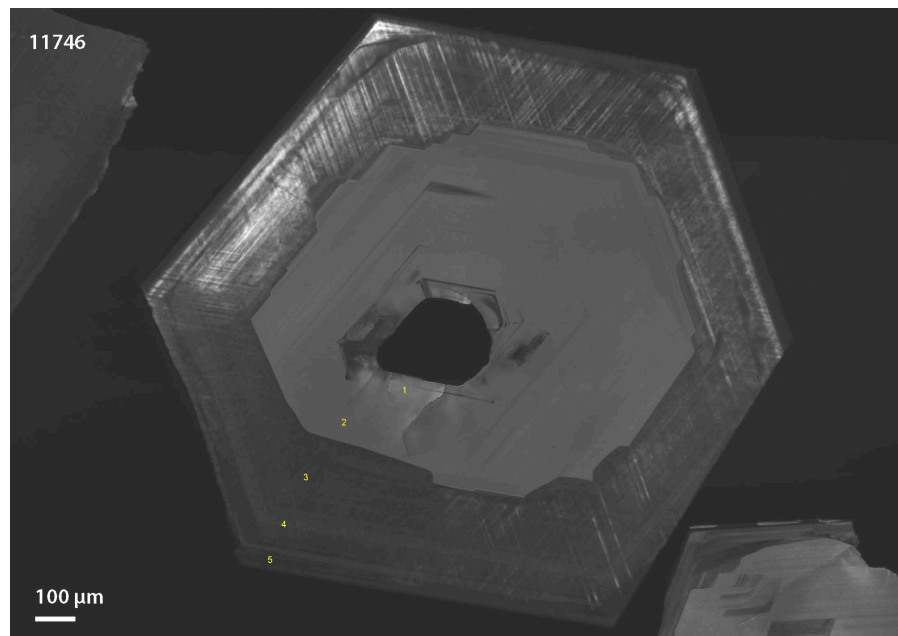
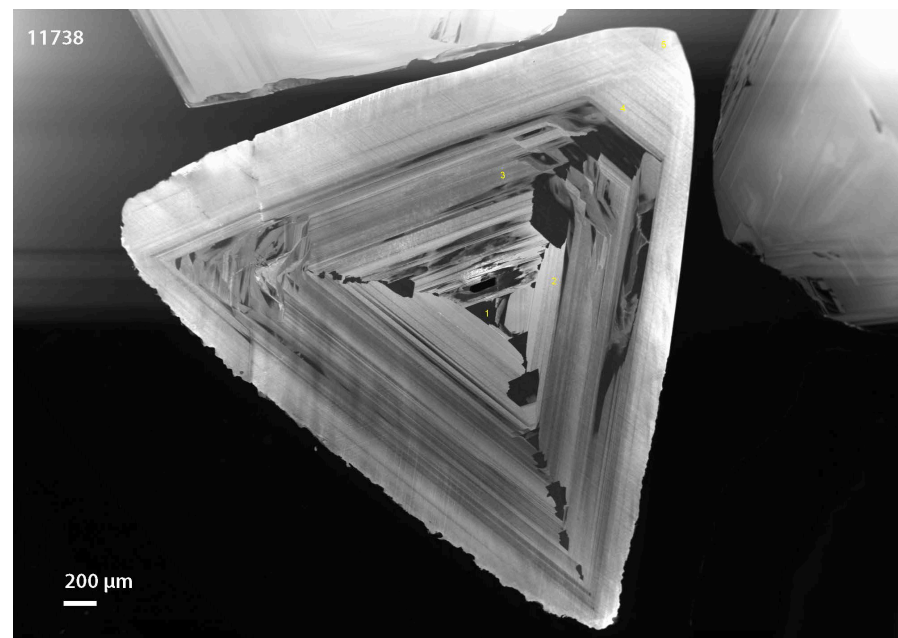
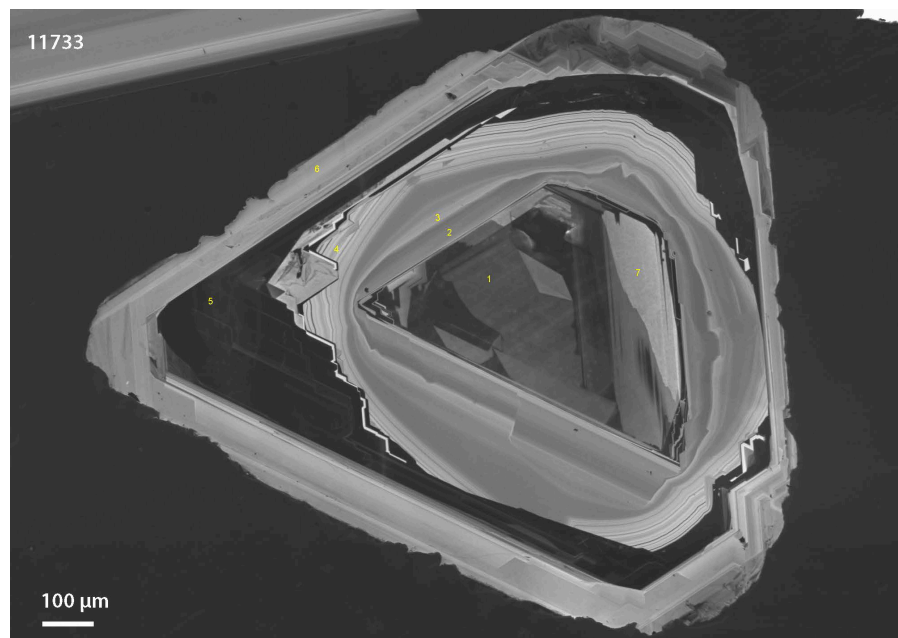


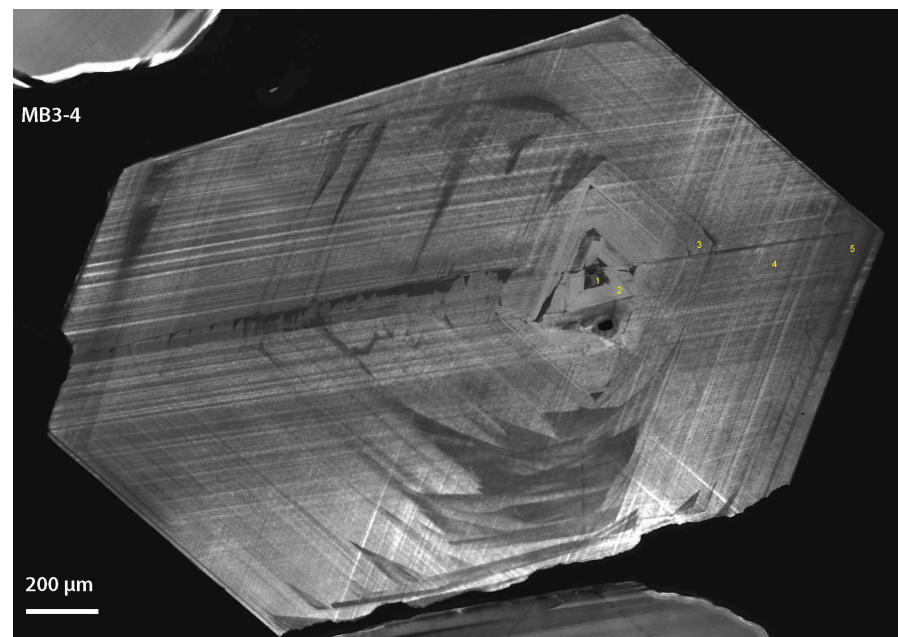
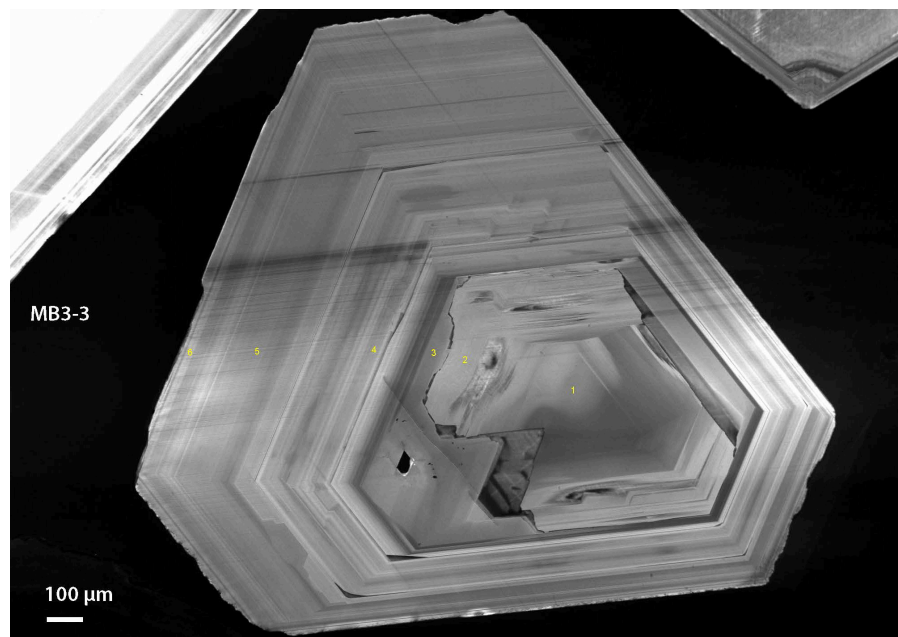
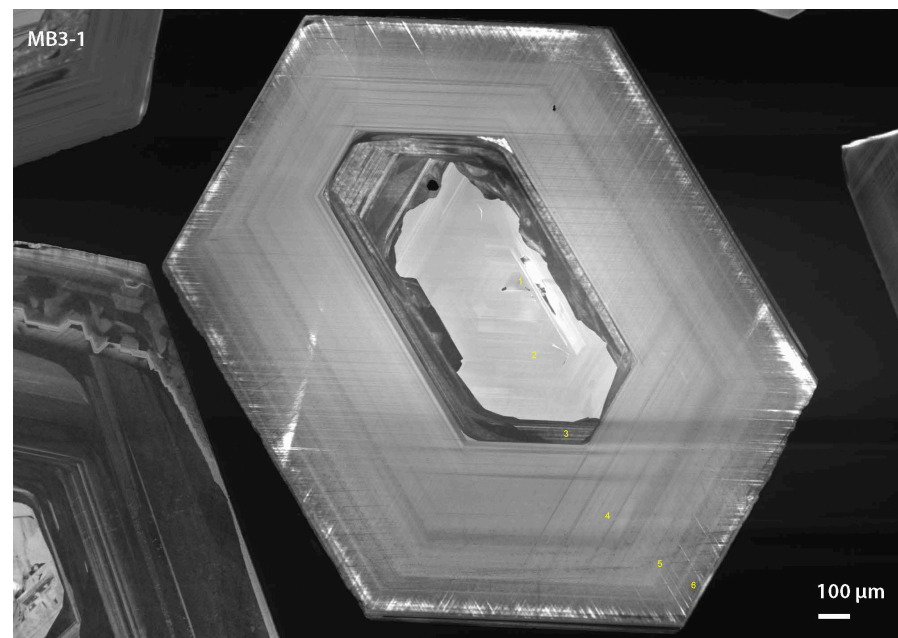
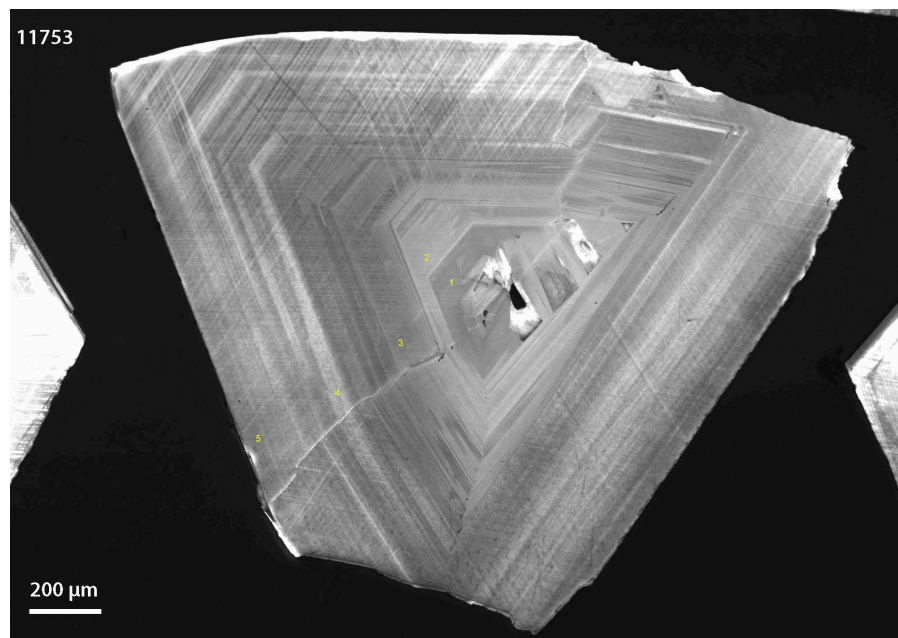


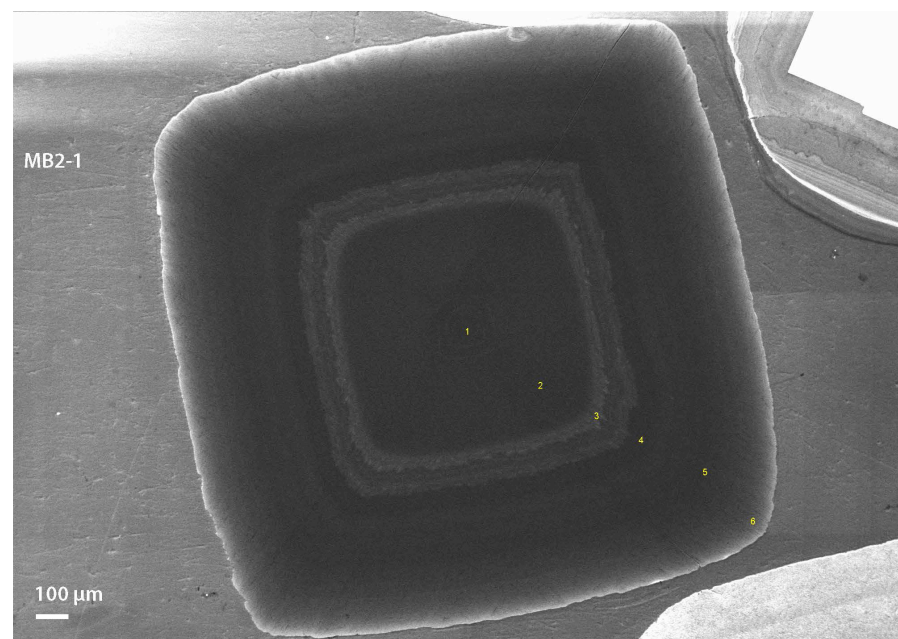
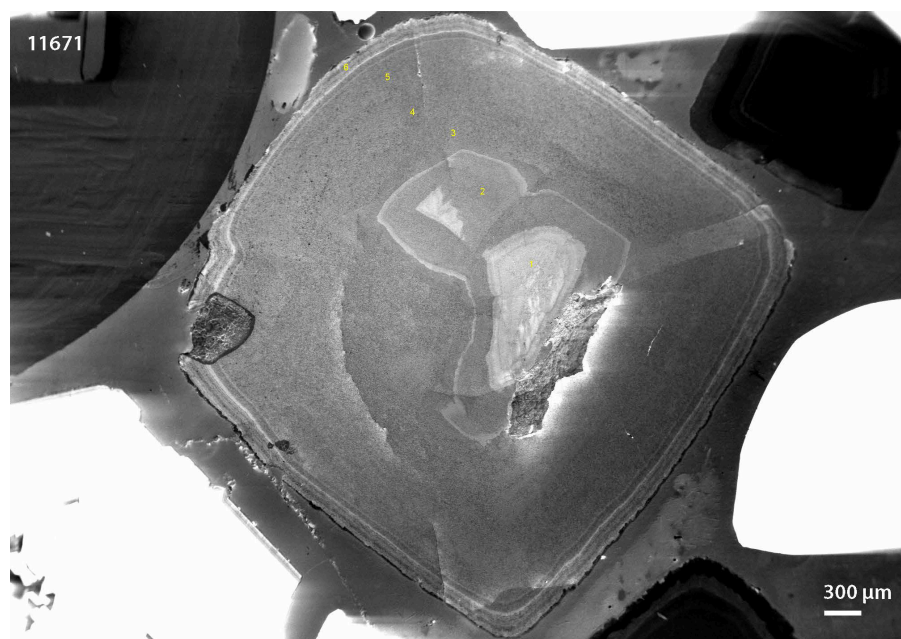
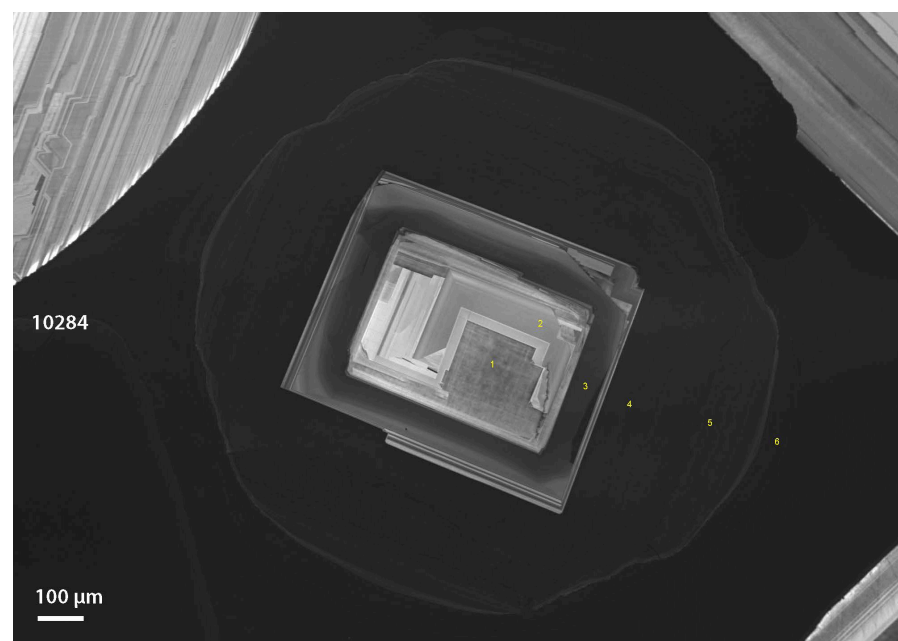
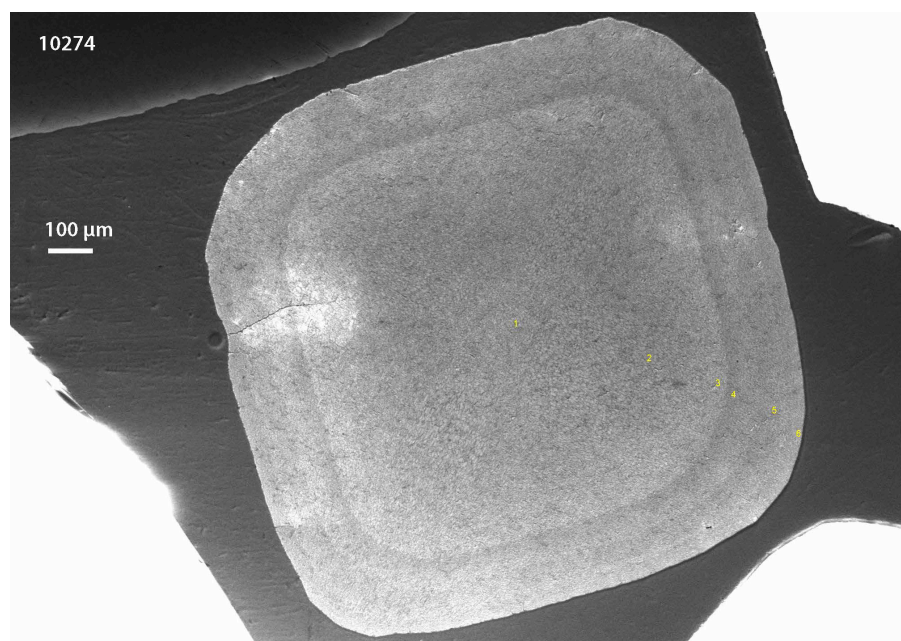


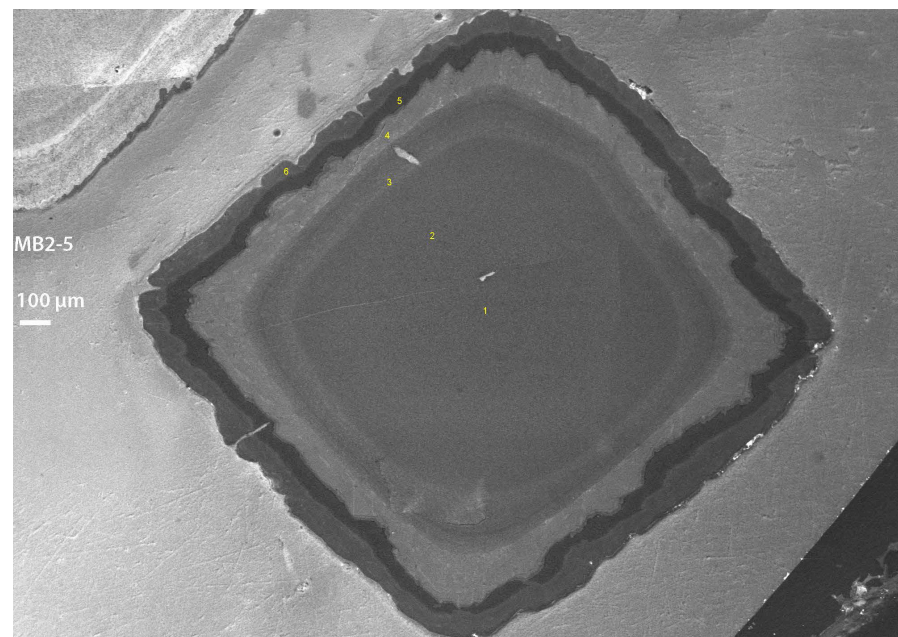
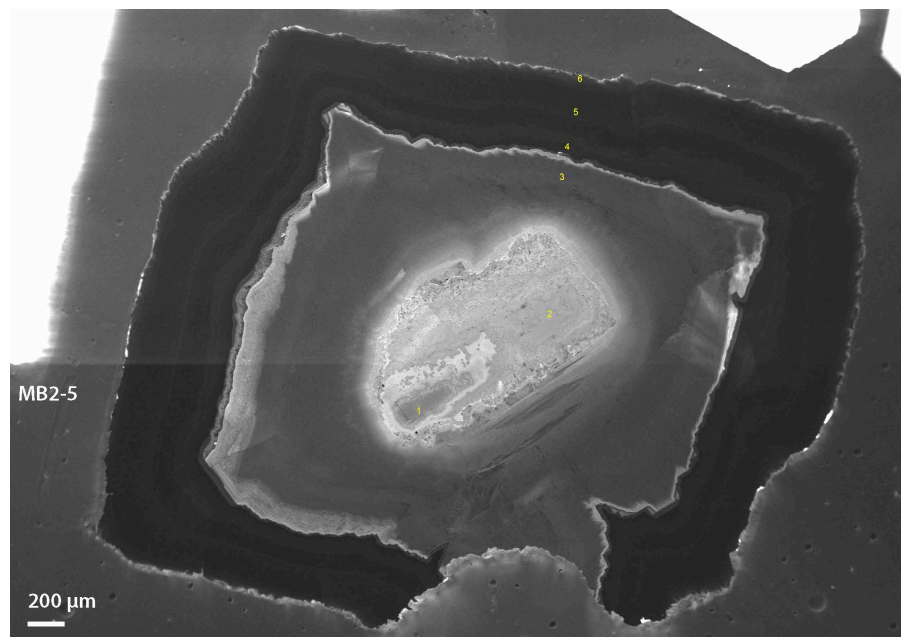
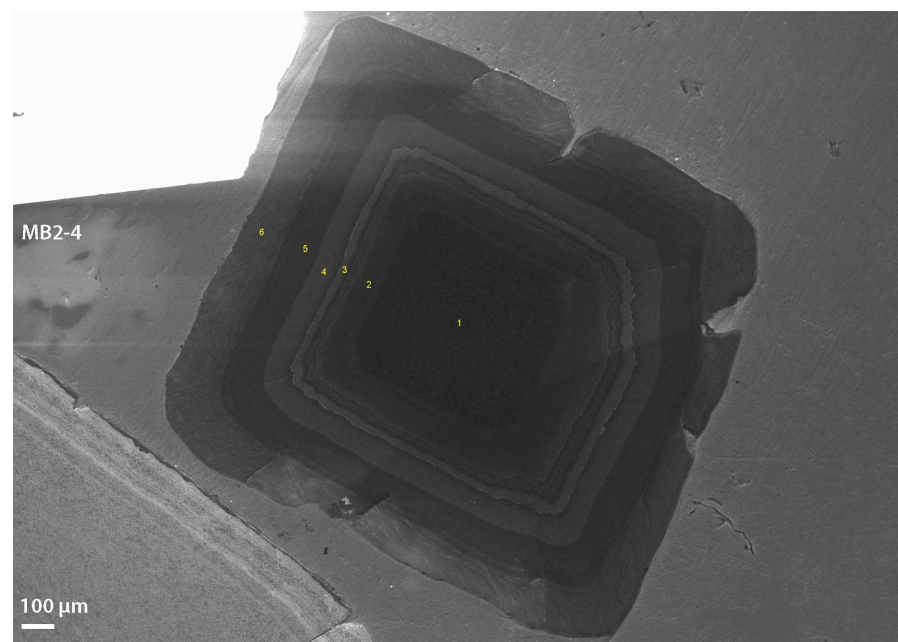
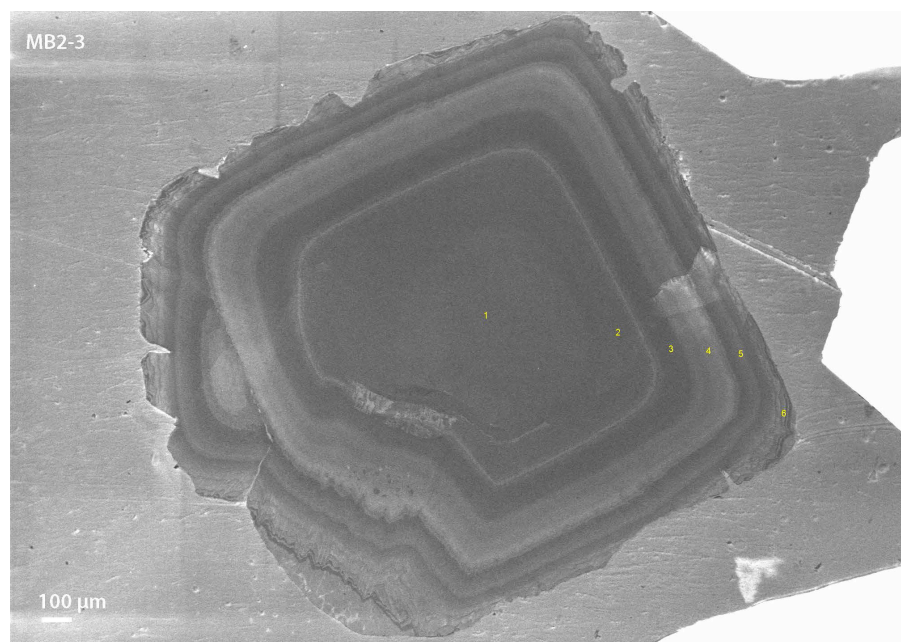












Appendix E: $\delta^{13}\text{C}$, [N] and cathodoluminescence (CL) characteristics of Kasai River diamonds

Sample	Spot	Growth Zone	Growth Zone Resorption	CL Brightness and Structure	Paragenesis	Inclusion Types	$\delta^{13}\text{C}$ (VPDB)	2σ (‰)	[N] atomic ppm	$\pm 95\%$ (ppm)	Rio Tinto (2014) Bulk [N]	%[N] _B
11601	4	1	Unresorbed	Dim CL	Eclogitic	Garnet	-13.56	0.33	24.3	0.7	390	67
	5	2	Unresorbed	Medium CL			-13.73	0.31	945.5	25.9		
	3	2		Medium CL			-13.56	0.31	1432.3	38.3		
	2	3	Unresorbed	Medium-Light CL, second core			-13.64	0.31	151.4	6.3		
	1	4	Unresorbed	Dim CL			-12.98	0.32	14.0	0.4		
11608	1	1	Unresorbed	Very Dim CL	Peridotitic	Olivine, orthopyroxene	-4.10	0.32	1.1	0.1	120	42
	2	2	Unresorbed	Medium CL			-3.76	0.31	36.2	1.0		
	3	3	Unresorbed	Medium CL, fine oscillations			-4.42	0.32	123.2	3.7		
	4	4	Unresorbed	Medium-Dim CL			-3.57	0.31	84.7	2.3		
	5	4		Medium CL, fine oscillations			-3.76	0.31	67.2	1.8		
11612	1	1	Unresorbed	Medium CL	Peridotitic	Olivine	-4.88	0.32	1257.0	33.1	140	43
	2	1		Medium-Dim CL			-4.30	0.31	393.7	10.9		
	3	1		Medium CL			-4.69	0.31	127.0	3.5		
	4	2	Resorbed	Medium CL, fine oscialltion			-4.73	0.32	205.6	5.6		
	5	2		Medium CL			-4.53	0.32	212.0	5.8		
	6	3	Resorbed	Medium-Light CL, second core			-5.69	0.31	75.1	2.1		

Sample	Spot	Growth Zone	Growth Zone Resorption	CL Brightness and Structure	Paragenesis	Inclusion Types	$\delta^{13}\text{C}$ (VPDB)	2σ (‰)	[N] atomic ppm	$\pm 95\%$ (ppm)	Rio Tinto (2014) Bulk [N]	%[N] _B
11625	1	1	Resorbed	Medium CL, mottled appearance	Peridotitic	Olivine	-2.86	0.31	6.4	0.2	-	-
	2	2	Unresorbed	Light CL			-2.88	0.32	622.6	17.3		
	3	2		Medium-Light CL, fine oscillation			-2.91	0.31	663.5	17.7		
	4	2		Medium-Light CL			-2.73	0.32	546.2	14.9		
	5	3	Unresorbed	Dim CL			-4.64	0.32	3.6	0.1		
11626	1	1	Resorbed	Dim CL	Peridotitic	Olivine, orthopyroxene	-2.64	0.32	1.7	0.1	430	51
	2	2	Resorbed	Medium CL			-2.51	0.32	770.2	20.5		
	3	2		Medium-Light CL			-2.35	0.32	225.0	6.2		
	4	3	Resorbed	Medium-Light CL, mottled appearance			-2.45	0.32	2.3	0.1		
	5	4	Unresorbed	Dim CL, fine oscillation			-4.44	0.31	1206.1	32.4		
11633	1	1	Resorbed	Dim CL	Peridotitic	Olivine, orthopyroxene	-4.88	0.31	2.6	0.1	100	45
	2	2	Resorbed	Medium CL, mottled appearance			-4.29	0.32	46.1	2.8		
	3	2		Medium-Dim CL, mottled appearance			-4.09	0.31	3.6	0.2		
	4	3	Unresorbed	Medium CL			-3.85	0.31	74.7	2.0		
	5	4	Unresorbed	Medium CL, fine oscillation			-4.18	0.31	326.7	8.6		

Sample	Spot	Growth Zone	Growth Zone Resorption	CL Brightness and Structure	Paragenesis	Inclusion Types	$\delta^{13}\text{C}$ (VPDB)	2σ (‰)	[N] atomic ppm	$\pm 95\%$ (ppm)	Rio Tinto (2014) Bulk [N]	%[N] _B
11634	1	1	Unresorbed	Medium-Dim CL	Not determined	Sulfide	-4.08	0.32	527.6	14.7	175	63
	2	2	Unresorbed	Medium CL			-3.93	0.31	371.5	10.7		
	3	2		Medium CL			-3.91	0.32	339.6	9.1		
	4	2		Medium CL			-3.89	0.32	222.2	6.6		
	5	3	Unresorbed	Medium-Dim CL, slightly mottled			-3.13	0.31	4.5	0.2		
11635	1	1	Unresorbed	Medium-Dim CL, complex	Eclogitic	Clinopyroxene	-3.45	0.32	20.0	0.6	315	68
	2	2	Resorbed	Medium-Light CL			-3.24	0.31	59.8	1.6		
	3	3	Resorbed	Medium CL			-5.05	0.32	691.9	18.5		
	4	3		Medium CL			-4.47	0.31	504.9	13.8		
	5	3		Medium CL			-4.53	0.32	599.1	16.0		
11637	1	1	Unresorbed	Medium-Dim CL	Peridotitic	Olivine	-3.19	0.31	557.6	15.1	420	62
	2	1		Medium CL			-3.07	0.31	465.1	12.8		
	3	1		Medium-Dim CL			-2.94	0.32	331.0	9.6		
	4	2	Resorbed	Medium CL			-3.06	0.32	287.9	8.1		
	5	2		Dim CL			-2.99	0.31	36.5	1.0		
	6	3	Resorbed	Dim CL			-2.81	0.31	1.3	0.1		
11655	1	1	Unresorbed	Dim CL	Peridotitic	Olivine, orthopyroxene	-4.37	0.32	1.3	0.1	40	50
	2	2	Resorbed	Medium CL			-4.38	0.31	4.1	0.1		
	3	2		Dim CL			-4.37	0.31	1.0	0.1		
	4	3	Resorbed	Medium CL, mottled			-4.10	0.31	10.4	0.3		
	5	3		Medium CL, mottled			-3.94	0.33	5.2	0.2		

Sample	Spot	Growth Zone	Growth Zone Resorption	CL Brightness and Structure	Paragenesis	Inclusion Types	$\delta^{13}\text{C}$ (VPDB)	2σ (‰)	[N] atomic ppm	$\pm 95\%$ (ppm)	Rio Tinto (2014) Bulk [N]	%[N] _B
11660	1	1	Unresorbed	Medium CL	Not determined	Sulfide	-22.48	0.31	84.9	2.5	90	39
	2	2	Unresorbed	Dim CL, second core			-23.03	0.31	1711.9	46.2		
	3	3	Unresorbed	Medium Dim CL, third core (?)			-22.15	0.31	530.7	14.4		
	4	3		Dim CL			-22.19	0.31	540.7	14.4		
	5	4	Resorbed	Medium-Light CL, mottled			-22.29	0.32	66.3	1.9		
11662	1	1	Unresorbed	Medium CL	Peridotitic	Olivine	-4.32	0.31	398.4	10.6	360	47
	2	1		Medium CL			-4.21	0.31	412.5	11.5		
	3	2	Unresorbed	Medium-Dim CL			-4.27	0.32	0.8	0.0		
	4	3	Unresorbed	Medium CL			-4.15	0.31	226.7	6.5		
	5	3		Medium CL, fine oscillation			-4.05	0.32	61.9	1.8		
	6	4	Unresorbed	Medium-Dim CL, fine oscillation			-4.09	0.32	11.1	0.3		
11664	3	1	Resorbed	Medium-Dim CL	Eclogitic	Clinopyroxene	-4.10	0.32	339.9	9.0	310	29
	4	2	Resorbed	Medium-Dim CL, rhombic striations			-4.16	0.31	247.0	6.7		
	1	3	Unresorbed	Medium CL, second core			-3.54	0.33	534.2	14.3		
	5	1		Medium-Dim CL			-4.04	0.31	544.1	14.7		
	6	1		Medium-Dim CL			-4.09	0.32	495.7	13.2		
	2	2		Medium CL, mottled			-4.34	0.31	97.4	2.6		

Sample	Spot	Growth Zone	Growth Zone Resorption	CL Brightness and Structure	Paragenesis	Inclusion Types	$\delta^{13}\text{C}$ (VPDB)	2σ (‰)	[N] atomic ppm	$\pm 95\%$ (ppm)	Rio Tinto (2014) Bulk [N]	%[N] _B
11690	1	1	Unresorbed	Medium CL	Not determined	Sulfide	-10.42	0.31	1190.5	32.1	600	60
	2	2	Unresorbed	Medium CL			-10.86	0.32	820.0	22.3		
	3	2		Medium CL			-10.88	0.31	844.4	22.9		
	4	3	Unresorbed	Medium-Dim CL			-9.42	0.32	988.7	26.7		
	5	4	Resorbed	Medium CL, fine oscillation			-9.03	0.33	492.1	13.1		
11691	1	1	Resorbed	Medium	Peridotitic	Olivine	-2.86	0.31	146.1	4.2	190	42
	2	1		Medium			-2.76	0.31	209.9	5.8		
	3	1		Medium			-2.72	0.32	199.6	5.7		
	4	2	Resorbed	Medium-dim, mottled			-4.01	0.32	7.0	0.3		
	5	3	Unresorbed	Medium-dim, fine oscillation			-3.53	0.32	248.6	6.6		
11699	1	1	Unresorbed	Medium-Dim CL	Peridotitic	Olivine	-2.00	0.32	1139.4	30.6	Offscale	-
	2	2	Unresorbed	Dim CL			-2.25	0.33	10.8	0.4		
	3	3	Unresorbed	Medium CL			-2.34	0.32	1314.9	35.4		
	4	4	Unresorbed	Medium-light CL			-2.24	0.32	818.2	22.0		
	5	1		Medium-dim CL			-1.94	0.32	1144.0	30.8		
	6	1		Medium CL, fine oscillation			-3.09	0.33	764.2	20.5		
11701	1	1	Unresorbed	Light CL	Peridotitic	Olivine	-4.75	0.31	110.0	3.0	95	68
	2	1		Dim CL			-4.85	0.32	0.9	0.1		
	3	1		Light CL			-4.82	0.33	73.4	2.2		
	4	2	Resorbed	Dim CL			-4.75	0.31	51.7	2.0		
	5	2		Medium CL, mottled			-4.19	0.32	2.2	0.1		
	6	3	Unresorbed	Medium-Dim CL			-4.74	0.32	222.5	5.9		

Sample	Spot	Growth Zone	Growth Zone Resorption	CL Brightness and Structure	Paragenesis	Inclusion Types	$\delta^{13}\text{C}$ (VPDB)	2σ (‰)	[N] atomic ppm	$\pm 95\%$ (ppm)	Rio Tinto (2014) Bulk [N]	%[N] _B
11710	1	1	Resorbed	Light CL	Peridotitic	Olivine	-2.42	0.31	128.3	4.4	25	80
	2	2	Resorbed	Dim CL			-2.55	0.31	0.9	0.1		
	3	2		Medium-Dim CL, mottled			-2.64	0.32	6.4	0.2		
	4	3	Resorbed	Medium-Dim CL			-2.47	0.31	1.0	0.1		
	5	3		Medium-Dim CL			-2.96	0.32	2.1	0.1		
	6	4	Unresorbed	Medium CL, mottled			-3.83	0.31	11.6	0.3		
11712	1	1	Resorbed	Medium-Light CL	Eclogitic	Garnet, CLinopyroxene	-3.81	0.32	315.4	10.7	330	64
	2	2	Unresorbed	Medium CL, fine oscillation			-4.64	0.32	901.7	25.3		
	3	2		Medium CL, fine oscillation			-4.40	0.32	110.0	3.0		
	4	3	Resorbed	Medium-Dim CL, fine oscillation			-5.37	0.31	670.9	18.3		
	5	3		Medium-Dim CL, fine oscillation			-5.13	0.32	324.4	9.4		
	6	3		Medium-Dim CL, fine oscillation			-5.09	0.31	249.6	6.7		
11715	1	1	Resorbed	Medium CL, complex	Peridotitic	Olivine	-3.99	0.31	3.0	0.1	55	55
	2	1		Dim CL			-3.73	0.32	1.0	0.0		
	3	2	Resorbed	Medium CL, mottled			-4.27	0.31	8.0	0.2		
	4	2		Medium CL, mottled			-3.98	0.32	8.8	0.2		
	5	3	Unresorbed	Medium CL			-4.36	0.31	325.7	8.9		

Sample	Spot	Growth Zone	Growth Zone Resorption	CL Brightness and Structure	Paragenesis	Inclusion Types	$\delta^{13}\text{C}$ (VPDB)	2σ (‰)	[N] atomic ppm	$\pm 95\%$ (ppm)	Rio Tinto (2014) Bulk [N]	%[N] _B
11720	1	1	Resorbed	Light CL	Peridotitic	Olivine	-3.27	0.31	153.8	5.1	80	88
	2	1		Medium CL			-3.23	0.32	1.1	0.1		
	3	2	Resorbed	Medium-dim CL			-3.06	0.31	0.9	0.1		
	4	2		Medium CL			-2.98	0.32	1.5	0.1		
	5	3	Resorbed	Medium-Light CL, mottled			-3.20	0.32	15.4	0.4		
11730	1	1	Unresorbed	Dim CL	Peridotitic	Olivine	-4.06	0.31	5.8	0.2	220	41
	2	2	Resorbed	Medium CL			-4.04	0.32	431.3	11.9		
	3	2		Medium CL			-4.02	0.32	280.6	7.4		
	4	2		Medium CL			-3.86	0.32	163.4	4.3		
	5	3	Resorbed	Medium-Dim CL			-4.38	0.32	792.1	21.4		
11731	1	1	Resorbed	Light CL	Eclogitic	Clinopyroxene	-17.76	0.32	257.4	7.0	350	63
	2	1		Medium CL			-17.53	0.31	1003.5	27.3		
	3	1		Light CL			-17.96	0.32	634.6	17.7		
	4	2	Unresorbed	Medium-Dim CL			-14.32	0.31	1119.4	30.1		
	5	2		Medium-Dim CL			-15.32	0.31	900.3	24.2		
11732	1	1	Resorbed	Medium CL, mottled, rhombic pattern	Peridotitic	Olivine	-3.23	0.32	6.2	0.2	140	32
	2	1		Medium CL, mottled			-3.21	0.31	1.9	0.1		
	3	2	Resorbed	Medium CL, mottled, rhombic pattern			-4.42	0.31	8.6	0.3		
	4	3	Unresorbed	Medium-Dim CL			-4.37	0.31	1198.4	32.5		
	5	3		Medium CL, fine oscillation			-3.46	0.32	376.1	11.7		

Sample	Spot	Growth Zone	Growth Zone Resorption	CL Brightness and Structure	Paragenesis	Inclusion Types	$\delta^{13}\text{C}$ (VPDB)	2σ (‰)	[N] atomic ppm	$\pm 95\%$ (ppm)	Rio Tinto (2014) Bulk [N]	%[N] _B
11733	1	1	Unresorbed	Medium-Dim CL	Not determined	Sulfide	-27.15	0.32	27.2	0.8	380	39
	7	1		Medium CL			-27.32	0.31	83.9	2.4		
	2	2	Resorbed	Medium CL			-5.78	0.31	1180.5	31.9		
	3	2		Medium Light CL			-5.25	0.32	870.5	23.9		
	4	2		Medium-Light CL, fine oscillation			-6.10	0.32	709.8	19.3		
	5	3	Resorbed	Dim CL			-6.04	0.32	12.5	0.3		
	6	4	Unresorbed	Medium CL			-5.66	0.32	454.2	12.2		
11738	1	1	Unresorbed	Dim	Peridotitic	Olivine, orthopyroxene	-8.53	0.32	0.8	0.0	55	55
	2	1		Medium-Light CL			-8.03	0.32	46.4	1.4		
	3	1		Medium CL, fine oscillation			-5.04	0.32	4.3	0.1		
	4	2	Resorbed	Medium-Light CL, mottled			-3.87	0.32	12.3	0.3		
	5	2		Light CL, mottled			-4.80	0.33	8.6	0.2		
11746	1	1	Resorbed	Medium CL	Peridotitic	Olivine, orthopyroxene	-3.69	0.32	171.2	4.9	90	56
	2	1		Medium CL			-3.95	0.31	175.2	4.7		
	3	2	Unresorbed	Medium-Dim CL			-3.28	0.31	9.8	0.3		
	4	2		Medium CL, fine oscillations			-3.15	0.31	27.1	0.8		
	5	2		Medium-Dim CL			-3.58	0.32	8.4	0.2		

Sample	Spot	Growth Zone	Growth Zone Resorption	CL Brightness and Structure	Paragenesis	Inclusion Types	$\delta^{13}\text{C}$ (VPDB)	2σ (‰)	[N] atomic ppm	$\pm 95\%$ (ppm)	Rio Tinto (2014) Bulk [N]	%[N] _B
11747	1	1	Resorbed	Light CL, mottled	Peridotitic	Olivine	-5.28	0.31	81.3	2.2	175	49
	2	1		Medium-Light CL, mottled			-5.13	0.32	100.6	2.8		
	3	2	Resorbed	Medium CL, mottled			-4.32	0.32	55.7	2.3		
	4	2		Dim CL			-4.28	0.32	1.0	0.1		
	5	3	Unresorbed	Medium-Dim CL, fine oscillation			-4.25	0.31	368.6	9.8		
	6	3		Dim CL			-3.98	0.31	2962.2	81.0		
11753	1	1	Unresorbed	Medium CL	Peridotitic	Olivine, orthopyroxene	-4.00	0.32	844.4	23.1	140	0
	2	1		Medium-Light CL			-4.01	0.31	484.0	12.8		
	3	1		Medium Light			-3.94	0.31	256.6	6.8		
	4	2	Unresorbed	Medium CL, mottled			-3.79	0.32	60.7	1.7		
	5	2		Medium CL mottled			-3.52	0.32	68.3	1.8		
MB3-1	1	1	Resorbed	Medium-Light CL	Peridotitic	Olivine	-4.50	0.32	1170.8	31.5	240	67
	2	1		Light CL			-4.13	0.33	985.3	26.7		
	3	2	Resorbed	Medium-Dim CL, mottled			-3.88	0.32	4.1	0.2		
	4	3		Medium CL			-4.29	0.32	337.1	9.3		
	5	3	Unresorbed	Medium CL			-3.76	0.32	152.4	4.2		
	6	3		Medium CL, rhombic pattern			-3.43	0.31	54.5	1.5		

Sample	Spot	Growth Zone	Growth Zone Resorption	CL Brightness and Structure	Paragenesis	Inclusion Types	$\delta^{13}\text{C}$ (VPDB)	2σ (‰)	[N] atomic ppm	$\pm 95\%$ (ppm)	Rio Tinto (2014) Bulk [N]	%[N] _B
MB3-3	1	1	Resorbed	Medium CL	Peridotitic	Olivine	-3.27	0.32	510.9	13.5	500	47
	2	1		Medium-Light CL			-3.33	0.31	414.9	11.2		
	3	2	Unresorbed	Medium CL			-4.11	0.31	898.6	24.4		
	4	3	Unresorbed	Medium CL, fine oscillation			-3.85	0.32	632.2	17.4		
	5	3		Medium CL			-3.92	0.32	625.4	17.0		
	6	3		Medium-Light CL, fine oscillation			-3.86	0.32	628.5	17.1		
MB3-4	1	1	Resorbed	Dim CL	Peridotitic	Orthopyroxene	-12.48	0.31	9.5	0.3	45	60
	2	1		Medium CL			-3.62	0.32	257.9	7.9		
	3	1		Medium-Dim CL, mottled, rhombic pattern			-4.03	0.32	9.4	0.3		
	4	2	Unresorbed	Medium-Dim CL, mottled, rhombic pattern			-3.88	0.31	29.2	0.8		
	5	2		Medium-Dim CL, mottled, rhombic pattern			-3.94	0.31	64.1	1.7		
10274	1	1	Unresorbed	Medium CL	Not determined	-	-5.32	0.31	1297.7	34.8	-	-
	2	1		Medium CL			-4.93	0.32	1271.3	34.0		
	3	1		Medium-Light CL			-4.39	0.31	1139.6	30.4		
	4	2	Unresorbed	Medium-Dim CL			-5.01	0.33	1227.8	32.4		
	5	2		Medium CL			-4.62	0.31	1160.7	30.9		
	6	2		Medium CL			-4.45	0.32	1084.4	29.7		

Sample	Spot	Growth Zone	Growth Zone Resorption	CL Brightness and Structure	Paragenesis	Inclusion Types	$\delta^{13}\text{C}$ (VPDB)	2σ (‰)	[N] atomic ppm	$\pm 95\%$ (ppm)	Rio Tinto (2014) Bulk [N]	%[N] _B
10284	1	1	Unresorbed	Very light CL, rhombic pattern	Not determined	-	-6.24	0.32	9.4	0.3	-	-
	2	1		Very light CL			-7.21	0.31	1004.9	26.9		
	3	1		Medium CL			-9.34	0.31	2157.5	58.1		
	4	2	Unresorbed	Medium-Dim CL, fine oscillation			-7.03	0.32	1212.6	33.1		
	5	2		Medium CL, fine oscillation			-6.74	0.33	947.7	25.4		
	6	3	Unresorbed	Dim CL, fine oscillation			-7.06	0.32	1081.0	29.5		
11671	1	1	Resorbed?	Light CL	Not determined	-	-5.15	0.32	517.7	13.9	-	-
	2	2	Unresorbed	Medium CL			-6.01	0.31	973.9	25.9		
	3	3	Unresorbed	Medium CL			-5.53	0.31	957.5	26.1		
	4	3		Medium CL			-5.73	0.31	976.5	26.3		
	5	3		Medium CL			-5.52	0.32	973.3	26.5		
	6	4	Unresorbed	Medium-Light CL, fine oscillation			-6.34	0.33	882.6	23.8		
MB2-1	1	1	Unresorbed	Medium-Dim CL	Not determined	-	-7.16	0.32	1671.8	44.7	-	-
	2	1		Medium-Dim CL			-6.54	0.31	1571.5	42.5		
	3	2	Unresorbed	Medium CL, fine oscillation			-5.52	0.31	1251.5	33.9		
	4	3	Unresorbed	Medium-Dim CL			-6.80	0.32	1476.8	39.7		
	5	3		Medium-Dim CL			-7.02	0.32	1447.5	39.6		
	6	3		Medium CL			-6.50	0.31	1336.2	35.5		

Sample	Spot	Growth Zone	Growth Zone Resorption	CL Brightness and Structure	Paragenesis	Inclusion Types	$\delta^{13}\text{C}$ (VPDB)	2σ (‰)	[N] atomic ppm	$\pm 95\%$ (ppm)	Rio Tinto (2014) Bulk [N]	%[N] _B
MB2-3	1	1	Unresorbed	Medium CL	Not determined	-	-4.97	0.31	1632.5	43.8	-	-
	2	1		Medium CL			-5.21	0.32	1664.0	44.8		
	3	2	Unresorbed	Medium-Dim CL			-6.40	0.31	1842.3	49.0		
	4	3	Unresorbed	Medium CL, fine oscillation			-4.29	0.33	1450.4	39.2		
	5	4	Unresorbed	Medium CL, fine oscillation			-5.84	0.32	1536.3	41.8		
	6	5	Unresorbed	Medium CL, fine oscillation			-6.41	0.31	1201.8	32.1		
MB2-4	1	1	Unresorbed	Dim CL	Not determined	-	-4.14	0.32	2975.6	80.4	-	-
	2	1		Medium-Dim CL			-5.98	0.31	2401.8	65.4		
	3	2	Unresorbed	Medium CL			-4.80	0.32	1822.7	49.2		
	4	3	Unresorbed	Medium CL			-5.17	0.32	1675.2	44.9		
	5	4	Unresorbed	Medium-Dim CL			-5.90	0.32	1963.8	53.5		
	6	5	Unresorbed	Medium CL, mottled			-5.73	0.32	1560.0	42.6		
MB2-5	1	1	Unresorbed	Medium CL	Not determined	-	-6.18	0.32	997.4	26.4	-	-
	2	1		Light CL, mottled			-4.99	0.31	963.1	27.1		
	3	1		Medium CL			-5.90	0.31	1678.1	45.9		
	4	2	Unresorbed	Medium-Dim CL			-7.54	0.31	1480.6	40.6		
	5	2		Medium-Dim CL			-7.51	0.32	1400.7	38.2		
	6	2		Medium-Dim CL			-7.07	0.32	1067.4	29.3		

Sample	Spot	Growth Zone	Growth Zone Resorption	CL Brightness and Structure	Paragenesis	Inclusion Types	$\delta^{13}\text{C}$ (VPDB)	2σ (‰)	[N] atomic ppm	$\pm 95\%$ (ppm)	Rio Tinto (2014) Bulk [N]	%[N] _B
MB2-6	1	1	Unresorbed	Medium CL	Not determined	-	-7.18	0.31	1386.7	37.8	-	-
	2	1		Medium CL			-7.15	0.32	1378.1	37.5		
	3	2	Unresorbed	Medium CL			-6.66	0.31	1253.5	34.3		
	4	3	Unresorbed	Medium-Light CL, mottled			-6.15	0.32	974.9	26.9		
	5	4	Unresorbed	Medium-Dim CL			-7.27	0.31	1371.5	37.5		
	6	5	Unresorbed	Medium CL			-6.86	0.33	1145.5	31.2		